MODELING FATIGUE BEHAVIOR OF ADDITIVELY MANUFACTURED NI-BASED SUPERALLOYS VIA CRYSTAL PLASTICITY

by

Veerappan Prithivirajan

A Dissertation

Submitted to the Faculty of Purdue University

In Partial Fulfillment of the Requirements for the degree of

Doctor of Philosophy

School of Aeronautics and Astronautics

West Lafayette, Indiana

May 2020

THE PURDUE UNIVERSITY GRADUATE SCHOOL
STATEMENT OF COMMITTEE APPROVAL

Dr. Michael Sangid, Chair

School of Aeronautics and Astronautics

Dr. Ganesh Subbarayan

School of Mechanical Engineering

Dr. Thomas Siegmund

School of Mechanical Engineering

Dr. Weinong Chen

School of Aeronautics and Astronautics

Approved by:

Dr. Gregory Blaisdell

Head of the Graduate Program

To my dear father, Mr. Veerappan Arunachalam.

ACKNOWLEDGMENTS

First and foremost, I would like to sincerely thank my mentor and advisor, Dr. Michael Sangid, for providing me an opportunity to pursue my PhD in his lab. His enthusiasm, drive for results, emphasis on high quality, and insightful questions has always motivated me to be a better researcher. He also took serious attention to my long-term career goals: provided an opportunity to be a teaching assistant in his fatigue course, recommended me for an instructor position in the AAE department and for a postdoc position at the Los Alamos National Laboratory. None of this would have been possible without his constant support and encouragement throughout my doctoral studies. Also, thanks to my committee members: Dr. Chen, Dr. Siegmund, and Dr. Subbarayan for their guidance over these years. I would also like to acknowledge the financial support by DARPA (N66001-14-1-4041) under program managers M. Maher and J. Vanderbrande.

This research work heavily relied on multi-modal experimental data provided by our collaborators. I would like to thank LTC Todd Book (Purdue) for the EBSD characterization and mechanical testing, Alex Finch (Purdue) for the tomography porosity analysis, Alexandra Mallory (Purdue) for fracture surface analysis, Drs. Xianghui Xiao, Jun-Sang Park, and Peter Kenesei of Argonne National Laboratory for their assistance in the set-up of the high-energy X-ray experiments, Peter Coutts (Penn State) for conducting tomography of the parts, and Priya Ravi (Purdue) for her help with the reconstruction of data from high-energy X-ray experiments. The use of the Advanced Photon Source was supported by the US Department of Energy, Office of Science, Office of Basic Energy Sciences, under contract no. DE-AC02-06CH11357

I would also like to thank all my co-workers who have helped me with my research work. Thanks to Dr. Saikumar Yeratapally for sharing his initial scripts on microstructure generation and meshing and teaching me various tools, Dr. Ritwik Bandyopadhyay for parallelizing my scripts to make them computationally efficient and also proof reading two of my manuscripts, Ajey Venkatraman and Dr. Andrea Nicolas for sharing their GB smoothing code, and Dr. Kartik Kapoor for his help with creation of tessellated grains in the microstructure model.

I would like to thank all the former and current lab members of the ACME^2 lab for creating a very collaborative environment and providing an avenue for many insightful conversations: Saikumar, Andrea Rovinelli, Todd, Andy, Ajey, Kartik, Diwakar, Ronald, Imad, Saikiran, Priya, Sven, John, and Ritwik. To Andrea Rovinelli and Ritwik, I really enjoyed all the deep discussions on the topics of mechanics with both of you. To Andy, Ajey, and Kartik, thanks for driving me home on multiple occasions whenever I stayed late in the lab. I would also like to thank all my friends away from work for they are my support system: Pradeep, Meenu, Srikanth, Sugi, Venky, MVK Chaitanya, Siva Chaitanya, Vignesh, and Lakshman. I would like to thank my friends back in India, for patiently listening to all my complaints and banter: Bharanidharan, Vishnuram, Manikandan, and Sankar Ganesh.

I would like to thank the most important people in my life, my family members. Thanks to my brother and sister-in-law, Abimanyu and Sinduja, for tolerating me in first place, patiently listening to all my problems, for their warmth and affection, for motivating and helping through all my very tough times, and for being my therapists. If it were not for them, I would not have made this far. Of course, nothing would have been possible without the unconditional love and care of my parents. I thank my mother, Malarvili for all the sacrifices she made to raise me. Lastly, special thanks to my father, Veerappan, for he is my hero and my favorite person in the world. My PhD is dedicated to my father.

TABLE OF CONTENTS

LIST OF TABLES

LIST OF FIGURES

ABBREVIATIONS

AM	Additive manufacturing
CPFE	Crystal plasticity finite element
CT	Computed tomography
3D	Three-dimensional
2D	Two-dimensional
HEDM	High-energy diffraction microscopy
FF	Far-field
NF	Near-field
IN718	Inconel 718
TB	Twin boundary
EBSD	Electron backscatter diffraction microscopy
ROI	Region of interest
HCF	High cycle fatigue
APS	Advanced Photon Source
MIDAS	Microstructural Imaging and Diffraction Analysis Software
SEM	Statistical equivalent microstructure
CP	Crystal plasticity
FCC	Face centered cubic
GA	Genetic algorithm
DIP	Damage indicator parameter
BC	Boundary condition
FW	Full width
FWHM	Full width at half maximum
IPF	Inverse pole figure
RAMS	Rotational and axial motion system

ABSTRACT

Additive manufacturing (AM) introduces high variability in the microstructure and defect distributions, compared with conventional processing techniques, which introduces greater uncertainty in the resulting fatigue performance of manufactured parts. As a result, qualification of AM parts poses as a problem in continued adoption of these materials in safety-critical components for the aerospace industry. Hence, there is a need to develop precise and accurate, physics-based predictive models to quantify the fatigue performance, as a means to accelerate the qualification of AM parts. The fatigue performance is a critical requirement in the safe-life design philosophy used in the aerospace industry. Fatigue failure is governed by the loading conditions and the attributes of the material microstructure, namely, grain size distribution, texture, and defects. In this work, the crystal plasticity finite element (CPFE) method is employed to model the microstructure-based material response of an additively manufactured Ni-based superalloy, Inconel 718 (IN718). Using CPFE and associated experiments, methodologies were developed to assess multiple aspects of the fatigue behavior of IN718 using four studies. In the first study, a CPFE framework is developed to estimate the critical characteristics of porosity, namely the pore size and proximity that would cause a significant debit in the fatigue life. The second study is performed to evaluate multiple metrics based on plastic strain and local stress in their ability to predict both the modes of failure as seen in fractography experiments and estimate the scatter in fatigue life due to microstructural variability as obtained from fatigue testing. In the third study, a systematic analysis was performed to investigate the role of the simulation volume and the microstructural constraints on the fatigue life predictions to provide informed guidelines for simulation volume selection that is both computationally tractable and results in consistent scatter predictions. In the fourth study, validation of the CPFE results with the experiments were performed to build confidence in the model predictions. To this end, 3D realistic microstructures representative of the test specimen were created based on the multi-modal experimental data obtained from high-energy diffraction experiments and electron backscatter diffraction microscopy. Following this, the location of failure is predicted using the model, which resulted in an unambiguous one to one correlation with the experiment. In summary, the development of microstructure-sensitive predictive methods for fatigue assessment presents a tangible step

towards the adoption of model-based approaches that can be used to compliment and reduce the overall number of physical tests necessary to qualify a material for use in application.

1. INTRODUCTION

1.1 Motivation

Additive manufacturing (AM) is a revolutionary manufacturing technique, which builds a 3-D net-shaped component via layer-by-layer material deposition, with the use of CAD models. Selective laser melting (SLM) is one of the AM techniques that is used for fabrication of polycrystalline metallic parts. SLM offers numerous advantages over the conventional techniques (machining, milling, etc.) such as the ability to produce complex geometries, reduced tooling cost, and lead time reduction. However, SLM introduces high variability in microstructure and defect distribution such as porosity, surface roughness, and residual stress gradients that cause uncertainty in the resulting fatigue performance of the parts, which in one of the dominant modes of failure in the aerospace components [1]. As a result, qualification of AM parts continues to be a challenge to wide spread adoption of these materials into service, especially in safety-critical components for the aerospace industry [2].

The conventional qualification procedures for the aerospace parts require extensive experimental testing involving ~5,000 -100,000 specimens, which is both time consuming (~ 5-15 years) and costly (more than $130 million) [3]. For SLM materials, this approach could be even more intensive because of the drastic variability in the fatigue performance and hence, is not practical. Alternatively, a model-based approach could be utilized, which would accelerate the process by reducing the overall number of specimen level tests necessary. Therefore, the development of predictive models for quantifying fatigue performance is crucial.

Fatigue failure is plasticity-mediated and is governed by the underlying material microstructure, namely the grain sizes, morphologies, and orientations, grain boundary character distribution, and pore sizes and locations [4,5]. The role of porosity is of particular interest since it can cause a significant debit in fatigue life in synergy with the other microstructural attributes. Furthermore, the variability in the microstructure results in the scatter of the fatigue lives as shown in Figure 1.1. Predicting this scatter behavior and the associated modes of failure is an important problem in view of the qualification process. The crystal plasticity finite element (CPFE) method is a

microstructure-sensitive physics-based numerical tool ideally suited for the assessment of fatigue behavior in the polycrystalline materials [6] and is used extensively in this research work.

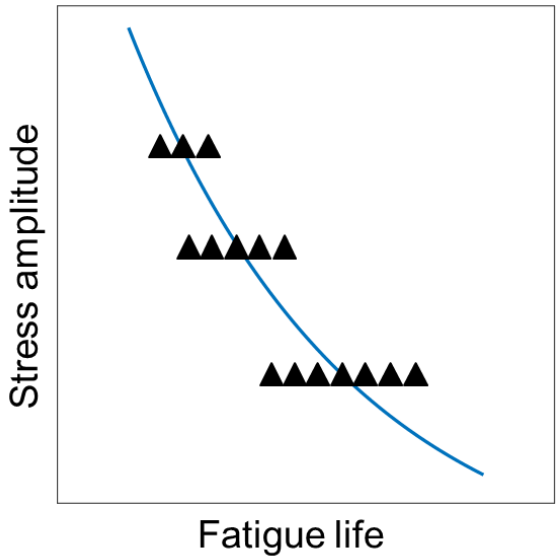

Figure 1.1 Scatter in the fatigue life due to the inherent microstructural variability

The aim of this research is to develop predictive methodologies based on CPFE simulations to address critical problems in the fatigue of additively manufactured IN718, which would provide a pathway forward in realizing rapid qualification of the AM materials. To this end, the four problems of interest are as follows:

- What are the limiting characteristics of a pore in terms of size and clustering that would cause a significant debit in fatigue life?
- What is an appropriate fatigue metric that could identify the location of failure and predict the scatter in fatigue life?
- What is the minimum number of grains in the simulation volume to obtain reliable estimates of the fatigue life?
- How well do the extreme values of the fatigue metrics obtained from CPFE simulations correlate with the experimental location of failure?

1.2 Research Contributions

The major contributions of this dissertation is outlined below:

1. Estimation of critical porosity characteristics
    - Porosity is a potential source of crack initiation and is dependent on the location, size and proximity to an adjacent pore or a surface. Quantifying the limiting characteristics of pore that would cause pore-mediated failures is important for process optimization and making an informed choice of the inspection methods. In this study, we determined the critical pore size and clustering relative to the microstructural length scale that would cause a significant debit in the fatigue life using a CPFE based framework.

2. Examining fatigue metrics for prediction of failure location and fatigue life
    - The safe-life design of the aerospace components requires information on the distribution of the fatigue lives and associated failure modes. In order to derive this information, an appropriate microstructure-sensitive fatigue metric is needed. In this study, we assessed multiple metrics based on plastic strain and local stress in their ability to predict the location and scatter in fatigue life and arrived at optimal choices using CPFE simulations of 3D virtual microstructures and experiments.

3. Role of simulation volume and microstructural constraints on the fatigue life prediction
    - Due to computational time limitations in performing CPFE simulations of large volumes (specimen or component scale), the fatigue prognosis is often performed using reduced volumes and simplified boundary conditions (BCs). The choice of the simulation volume is crucial to obtain accurate predictions and depends on the BCs utilized. In this study, we estimated the minimum simulation volume (or the number of grains in a microstructure) necessary to obtain reliable estimates of the fatigue life by performing a systematic analysis using CPFE simulations with the use of traction free BCs.

4. Validating the microstructure-sensitive fatigue crack initiation using crystal plasticity simulations and high-energy X-ray experiments
    - Validation is an important aspect of developing models to build trust in the predictions. In this study, we achieved an unambiguous 1-to-1 correlation between the extreme values of the fatigue metrics, plastic strain accumulation and plastic strain energy density, and the location of crack initiation with realistic 3D microstructures and boundary conditions.

1.3 Outline of the Dissertation

This dissertation is organized into eight chapters and a brief review of each chapter is as follows.

Chapter 1 presents a broad overview of the current gaps pertaining to the rapid qualification of the additively manufactured materials and a list of specific research questions to be addressed. Furthermore, the research contributions of this dissertation is specified.

Chapter 2 provides a review of the literature in context to the research questions, which are (a) estimation of critical porosity, (b) Examining metrics for fatigue life and location prediction, (c) role of simulations volume and microstructural constraints on the fatigue life prediction, and (d) validation of microstructure-sensitive fatigue crack initiation using crystal plasticity simulations and high-energy X-ray experiments

Chapter 3 describes the material and all the characterization techniques such as the electron backscatter diffraction microscopy, micro-tomography, and high-energy X-ray diffraction microscopy and fatigue testing with associated results.

Chapter 4 details out the primary ingredients of the crystal plasticity modeling framework, which includes the creation of synthetic microstructures using the statistical information obtained from experiments, the description of the material constitutive law, determination of the material parameters using a genetic algorithm, and the regularizing schemes used for post-processing of the results.

Chapter 5 presents a crystal plasticity based framework to quantify the critical porosity characteristics in terms of the pore size and clustering, including a description on the problem formulation based on micromechanics.

Chapter 6 reports a detailed methodology to predict both the location of fatigue crack initiation and life using multiple fatigue metrics followed by a comparative assessment among the metrics. Furthermore, the role of simulation volume and the microstructural constraints on the prediction of scatter in fatigue life is discussed.

Chapter 7 describes the work involving validation of the predicted location of microstructure-sensitive fatigue crack initiation using a high-fidelity crystal plasticity model informed via high-energy X-ray experiments. Moreover, the integrated setup is used to understand the role of twins on the crack initiation.

Chapter 8 presents the conclusions of this dissertation reflecting on the significance of this research work and a discussion on the potential future work.

2. LITERATURE REVIEW

2.1 Estimation of critical porosity characteristics

Porosity is a potential source of fatigue crack initiation in both AM [7–10] and in conventionally manufactured materials [11–16]. Experimental observations based on fractography analysis have shown that the characteristics of a crack-initiating pore in fatigue are related to the pore size and the proximity to the surface or an adjacent pore. Couper et al. have shown that the pore size is more critical than pore volume fraction in connection with the fatigue behavior of a cast aluminum alloy [11]. Wang et al. have experimentally estimated a critical pore size by comparing the fatigue lives of fully dense and porous microstructures of a cast aluminum alloy [12]. Additionally, researchers have shown that fatigue cracks initiate from near-surface and surface pores [9,15,17]. Furthermore, Danninger et al. [13] and Pang et al. [15] have shown that a pore cluster is a prominent location of crack initiation due to interaction effects. As of now, a robust understanding of the limiting cases of porosity in terms of pore size and clustering of pores for SLM materials is still elusive.

Computed tomography (CT) is a non-destructive method used in the detection and characterization of micro-pores in a material, and in the analysis of fatigue crack initiation. 3D reconstruction of the pores in the material microstructure using CT is shown in [7,18–23]. The detection of a pore is dependent on the resolution of the tomography set-up, which varies from sub-micron to sub-millimeter. In this work, two different resolutions per voxel are used, namely, 0.65 μm and 30 μm (Section 3.3). However, to make an informed optimal choice of a tomography set-up, prior knowledge of the minimum pore size that affects the fatigue properties is essential.

Extensive specimen testing under fatigue loading combined with fractography analysis or CT is one of the ways to identify limiting porosity. However, due to the time and cost involved, a more feasible alternative is to make use of numerical modeling and simulation. There has also been a growing need for predictive models in rapid qualification and certification of SLM materials [24], which is the focus of the present work.

Some of the early work on the role of porosity towards the mechanical behavior involved the development of analytical models to understand ductile failure using continuum plasticity theory

[25–30]. These pioneering works have played a significant role in understanding the deformation behavior of materials with pores. Recent studies explicitly account for pores within a finite element (FE) model as it allows for more complex geometry and material description. Gall et al. [31] and Fan et al. [32] studied the plastic strain localization around a pore using a continuum plasticity framework in an idealized 2D-FE analysis. Gall et al. found that pore size and loading ratios have a significant influence on the strain localization [31]. In addition, Fan et al. [32] and Xu et al. [33] obtained the trends on strain localization by varying the distance of the pore from the surface and spacing of the pore cluster. Gall et al. [31] and Baicchi et al. [34] showed that the pore shape has minimal effect on the plastic strain. All of the above studies model the deformation by placing the pore in a homogenized matrix [31–34] and thereby ignoring the effects of spatial inhomogeneity of a polycrystalline microstructure having various grain morphologies and orientations, which can significantly impact the results.

A few studies have been conducted by placing a pore within a heterogeneous matrix explicitly accounting for microstructural attributes. Gao et al. have studied the variation in plastic strain localization around a pore in a bi-crystal by varying the crystallographic orientation of the grains [35]. Carroll et al. have modeled the pore in a polycrystalline microstructure with a large number of grains having random orientations using 2D CP-FE simulations. They conducted the study using different pore sizes and concluded that the local microstructure profoundly influences the strain localization only when the pore has a size comparable to or less than the average grain size, and it has nearly no influence if the pore is significantly larger than the average grain size [36]. Battaile et al. extended the previous study [36] by performing a variability study on the peak plastic strain for different pore sizes using multiple instantiations. Within each microstructure instantiation, the crystallographic orientation of the grains is varied and grain morphology is held constant. Additionally, they showed that a sub-grain pore in a polycrystalline matrix localizes more plastic strain than when placed in an isotropic matrix [37]. The aforementioned studies [35–37] deal with monotonic (tensile) loading and hence do not provide adequate insights on the deformation behavior of pores subjected to cyclic loading. The cyclic deformation captures the effect of reverse plasticity, and stress redistribution that is of prime importance to the study of fatigue crack nucleation.

2.2 Examining metrics for fatigue life prediction

The fatigue performance, especially the crack initiation life, is a significant factor in the safe-life design philosophy used for critical aerospace components. Crack initiation is governed by the loading conditions and the material microstructure, namely, grain size distribution, texture, and defects [38,39]. It has been well established that the variability in microstructure leads to scatter in fatigue life [4,5]. The accurate prediction of scatter in fatigue life is of paramount importance to obtain the statistical minimum life for safe-life analysis [40–42] and further optimize AM process parameters to obtain tailored microstructures.

Some of the early fatigue lifing approaches were based on the regression analysis between the applied mechanical fields and fatigue life. Basquin proposed the first kind of this model, which related the applied alternating stress to fatigue life [43]. Coffin and Manson developed a fatigue life model based on the applied plastic strain, applicable to the low cycle fatigue regimes [44,45], and Morrow related plastic strain energy per cycle to fatigue life [46]. Each of these phenomenological models represent a two-parameter power-law regression to experimental data. Smith, Watson, and Topper proposed a combined stress-strain formulation to predict the fatigue life, which also includes the mean stress effect [47]. Fatemi and Socie developed a unified parameter based on shear strain and normal stress, and correlated with fatigue life, to obtain the critical plane during multi-axial loading [48]. While these classical approaches are easy to implement, they have mainly two major limitations: (a) require a significant amount of experimental data to characterize the model parameters and requires repetition of experiments upon any slight pedigree changes to the material and (b) lack physical insight into the crack initiation mechanisms, which limits their use in designing microstructures based on fatigue resistance. A physics-based model, as the one presented in this work, is necessary to overcome these limitations.

Several researchers formulated analytical models for understanding the crack initiation and life estimation based on the dislocation motion and interaction occurring at the defect scale. Tanaka and Mura modeled the plastic deformation within a slip band using two adjacent layers of dislocations and obtained an expression for cycles to crack initiation by relating the stored energy of dislocations and surface energy of the crack [49] and later, extended their model to account for crack initiation from inclusions [50]. Mura and colleagues made further developments of the

baseline model [49] to account for multiple slip bands [51,52]. Chan et al. made modifications to the dislocation dipole model [49] to explicitly incorporate crack size and microstructural size based on the minimization of the Gibbs free energy [53]. These models provide physical insights into the crack initiation; however, they do not account for the statistical variations of the microstructure, namely, grain size distribution, orientation distribution, and pores, hence, making it less applicable to quantify microstructure induced fatigue scatter. Sangid et al. formulated an atomistically informed prediction model for fatigue scatter with a special focus on crack initiation from persistent slip bands (PSBs) in nickel-based superalloys accounting for the microstructural variability [4,54,55]. However, their approach does not account for the complex evolution of stresses and strains within the microstructure, which requires the use of CPFE simulations.

In the past two decades, researchers have been extensively using microstructure-sensitive CPFE simulations to link the heterogeneities at the mesoscale to fatigue crack initiation. A fatigue metric (commonly known as the fatigue indicator parameter) is a combination of one or more mesoscale field quantities, which is used as a surrogate measure to identify the most likely location of crack initiation. The existing literature has a wide variety of fatigue metrics defined to assess fatigue. Multiple researchers have worked on correlating the fatigue metrics to the location of crack initiation; however, the assessment was based solely on a single mode of failure. For instance, Hochhalter et al. studied the crack initiation from a matrix-particle interface of an aluminum alloy and concluded that all the slip- and energy-based metrics, including the mesoscale Fatemi-Socie parameter [56–61], qualitatively predicted the same location of crack initiation [62]. Rovinelli et al. [63] and Nicolas et al. [64] also observed similar results in their respective works. On the other hand, Dunne and colleagues have studied the crack nucleation arising from a matrix–inclusion interface at the free surface of a nickel-based superalloy and concluded that the metric, stored energy density was able to accurately predict multiple crack initiation locations as compared to other metrics [65]. The findings from the researchers mentioned above cannot be generalized for multiple modes of failure as the mechanics of deformation varies with the failure mode under consideration. In the current work, multiple modes of failure, at the free surface and either a crystallographic feature or pore in the bulk of the microstructure are considered, which motivates the reassessment of the fatigue metrics for this work. Few researchers have looked at the competing failure modes using CPFE simulations, in particular, Prithivirajan and Sangid looked at the fatigue failure between crystallographic features and pores [66], and Bandyopadhyay and Sangid analyzed

failures from crystallographic features and an inclusion [67], however these works have not been used to obtain the scatter in fatigue life, which is one of the objectives of this work.

The fatigue metrics could also be used for the fatigue life estimation, for instance, the elastic stored energy [68] introduced by Dunne and colleagues has shown good correlations with experimental fatigue life data; however, it requires the use of a dislocation density-based model which is computationally expensive for 3D CPFE simulations and the identification of material parameters is challenging. Cruzado et al. proposed a two-parameter model based on the local plastic dissipation energy to predict the fatigue life [69]. Ghosh and colleagues proposed a fatigue life model based on effective traction and dislocation pile up; however, its suitability is limited to dwell fatigue of titanium alloys [70,71]. Yeratapally et al. proposed a fatigue model combining molecular dynamics and CPFE simulations with emphasis on the role of twin boundaries. This work involves the use of model parameters involving multiple length scales, which is very difficult to obtain and validate [72] and hence, difficult in practice to solve problems for industrial applications. In this study, a phenomenological CPFE model is employed to obtain multiple fatigue metrics, which are further utilized to obtain the failure location as well as the scatter in fatigue life. The model for obtaining fatigue life only involves a single parameter that could be easily obtained from experimental test data. This work also involves carrying out a comparative assessment among the multiple fatigue metrics.

2.3 Role of simulation volume and microstructural constraints on fatigue life predictions

While CPFE simulations have been proven to be useful in obtaining mechanistic insights at the microstructural length scale of polycrystalline materials, simulations involving large microstructures are computationally intensive. Hence, researchers often solve problems with multiple instantiations of reduced simulation volumes that are statistically representative, to mitigate the time limitation [4,5,58,73,74]. Tu et al. deduced that the minimum number of grains in the microstructure for the prediction of an effective property or response function varies from 100-300 grains based on the quantity of interest [74], but has not addressed the dependence of simulation volume (or the number of grains) on the fatigue life. A fatigue crack occurs at the weakest link in the material, which is a rogue combination of the microstructural features and defects in the microstructure. The probability of capturing the weakest link increases with either

increasing the number of grains in a single microstructure or with the number of instantiations with a reasonable number of grains in them [75]. Sangid et al. deduced that fatigue life decreases with an increase in the number of grains using their PSB energy model [4]. Yeratapally et al. have performed a sensitivity study on the fatigue scatter with respect to the number of grains within the microstructure, and found that 150 grains is a reasonable simulation size to capture the scatter [5], but has not investigated how the fatigue life prediction will change when the simulation volume is close to the test specimen's gauge volume, which has been addressed in this work. Moreover, previous studies have not explored the combined role of the simulation volume and the microstructure constraints towards the prediction of fatigue scatter, which is also addressed in this work.

2.4 Validation of microstructure-sensitive fatigue crack initiation using crystal plasticity simulations and high-energy X-ray experiments

Fatigue is the most common form of failure in the critical components of the aerospace industry and the material microstructure dictates the plasticity-mediated micro-crack initiation [39]. The development of a validated microstructure-sensitive predictive model for fatigue crack initiation would accelerate the qualification process by reducing the overall number of specimen level tests necessary. The crystal plasticity finite element (CPFE) method is a microstructure-sensitive physics-based numerical tool commonly used to simulate plasticity and fatigue damage in polycrystalline materials [6]. While CPFE has been in use for more than three decades and aspects of CPFE modeling are constantly improving since its inception, lack of rigorous validation efforts has restricted its usage in engineering design workflows [76,77]. To build trust in these models, they must be validated at a relevant length scale, which is the key aspect of this work.

The key inputs to any CPFE simulation are the microstructure (i.e. the description of the grain structure including morphologies, orientations, and grain boundaries and defect distribution) and the boundary conditions. As this work involves one to one comparison with experiments, it is important to replicate the physical test specimen at a mesoscale (i.e. the microstructure) and capture the exact loading scenario and boundary conditions of the test specimen. Recent developments in high-energy synchrotron X-ray techniques have made it possible to non-destructively probe the 3D microstructure of a specimen and acquire the evolution of the micromechanical fields with loading. Synchrotron X-ray micro-tomography (μCT) enables 3D

imaging of the specimen's internal structure based on the local density variations within the sample. μCT is useful to obtain the porosity map and location of fatigue crack initiation during loading in the specimen [78,79]. High-energy X-ray diffraction microscopy (HEDM) uses diffracted spots pertaining to individual crystallites from a rotating sample, illuminated with X-rays to obtain grain level information [80–85]. The near-field (NF) configuration of HEDM provides information on grain morphology and orientations [80–82]. The far-field (FF) configuration of HEDM provides the centroidal position, orientations, and elastic strain tensors for each grain illuminated by X-ray rays within the sample [83–85]. In this work, μCT, NF-HEDM, and FF-HEDM are sequentially used within the same experiment to obtain relevant information during fatigue loading. The subsequent data is used to instantiate the CPFE models and validate the predicted location of crack initiation. Annealing twins are present in the additively manufactured IN718 [86] and are known to significantly influence the local mechanical behavior. While it is quite challenging to identify and reconstruct twins using HEDM, due to restrictions in the dynamic range of the detectors; this limitation can be addressed by carefully setting up multiple CPFE models, as shown in this work.

Twin boundaries (TBs) are known to be preferential sites for fatigue crack initiation in Ni-based superalloys as observed from a few experimental studies [55,87]. Multiple models exist in literature to rationalize why a twin boundary is detrimental to fatigue crack initiation. Some of the earlier works developed analytical models, which showed that the TB developed high stress concentrations because of elastic and plastic incompatibilities [88–91]. Using atomistic calculations, Sangid et al. have derived that the TBs possess the lowest static energy and the highest energy barrier for dislocation motion [55]. Thus, TBs are shown to be both beneficial as well as detrimental to fatigue. Using CPFE simulations, Castelluccio and McDowell have shown that the insertion of twins have increased the extreme values of the Fatemi-Socie parameter [92]. Yeratapally et al. have demonstrated through CPFE simulations that regions adjacent to TBs have high values of elastic stress anisotropy and plastic strain accumulation thereby providing favorable sites for crack initiation [5]. Cerrone et al. from the simulations concluded that high elastic anisotropy and coplanarity of the boundary plane with an active slip plane are the main reasons for TBs to be crack initiators [93]. In this work, we investigate the synergetic aspect of twins via comparing the local micromechanical fields obtained from the microstructural models with and without twins, along with the aforementioned validation efforts.

Recently, several researchers have attempted to validate CPFE model using grain-scale micromechanical fields from experiments. Turner et al. have instantiated a CPFE model informed from the HEDM experiments and showed a reasonable agreement in grain-averaged stresses between the simulations and experiments [94]. Kapoor et al. [95] and Tari et al. [96] have used the same dataset as Ref. [94] and have shown improved predictions in stresses between the CPFE and HEDM after initializing their models with residual stresses. However, validating grain-scale stresses does not guarantee the accurate capture of fatigue crack location, which is a localized event. Few authors have validated a CPFE model with respect to the location of fatigue crack initiation. For instance, Chen et al. have predicted multiple crack locations at the matrix-inclusion interface of a Ni-based superalloy using the extreme values of local stored energy obtained from the CPFE simulations [65]. Bandyopadhyay et al. validated the crack initiation location of Ti-6Al-4V alloys using the soft-hard-soft grain rationale and local micromechanical fields obtained from CPFE simulations [97]. Nicolas et al. probed the environmentally-assisted fatigue crack initiation using multiple fatigue metrics [64]. The aforementioned works [64,65,97] have achieved excellent results, however, the sub-surface information was not included in their models, which has been shown to significantly influence the local micromechanical fields [98]. Cerrone et al. have investigated the fatigue crack initiation at a TB using a 3D realistic microstructural model informed from HEDM experiments [93]. They performed correlation studies between the fatigue metrics and the failure locations in a qualitative sense and reported that the values of slip-based metrics and a transmission-based metric were high at the location of crack initiation. Given that, the predictive models for use in safety-critical applications demand a high degree of confidence, a detailed quantitative assessment of the correlations (between the metrics and the crack location) via the probability measures is crucial, which is performed in this work.

3. MATERIAL AND EXPERIMENTS

In this chapter, the material of interest and the details of different experimental characterization techniques and testing used in this work are described. These experimental data are further used in the modeling efforts and solve the problems associated with the fatigue of additively manufactured IN718 as described in the introduction section.

3.1 Material and fabrication

The material of interest in this study is IN718, produced by SLM. The material was produced at Penn State University's Center for Innovative Materials Processing through Direct Digital Deposition (CIMP-3D) via an EOSINT M280 system [99]. Samples were produced in bulk blocks (from which coupons would be extracted) and net-shape dogbone specimens, both of which were built in the vertical orientation. The samples underwent a stress relief heat treatment prior to being removed from the build plate (1065 °C for 1.5 hours followed by a two-bar argon cooling). Afterwards, the parts underwent vacuum homogenization (1177 °C for 1 hour followed by two bar argon cooling at 38 °C/hr to below 538 °C), vacuum solution heat treatment (982 °C for 1 hour followed by gas fan cooling with argon to below 149 °C), and a two-part vacuum aging process (718 °C for 8 hours, furnace cooled to 621 °C and held for 18 hours, and then gas fan cooled with argon to below 149 °C). It should be noted that the samples did not undergo hot isostatic pressing. The heat treatment was adequate to form γ' and γ'' precipitates, as the major strengthening mechanism in this alloy, as well as a large fraction of annealing twins.

3.2 Electron backscatter diffraction analysis

To identify the grain attributes, several coupons of the material were characterized via electron backscatter diffraction (EBSD) analysis using a Phillips XL-40 SEM with an EDAX EBSD camera and associated TSL data collection and analysis software. More details on the scan parameters and EBSD analysis are available in [86]. The grain map is shown in Figure 3.1. The pertinent microstructural attributes used in this study are a grain size of 52.7 μm with a standard deviation of 52.2 μm, random texture, and twin area fraction of 0.52.

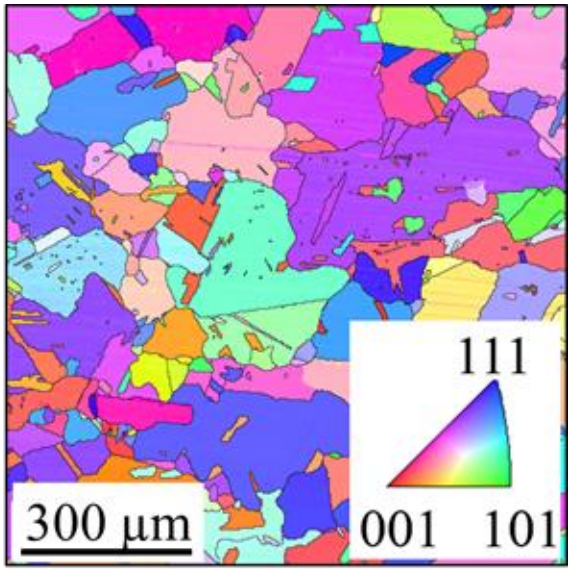

Figure 3.1 2D grain map of SLM IN718 obtained via EBSD analysis indicating the presence of annealing twins in this material.

3.3 Tomography characterization

To characterize the defects inherent in the material as a result of the SLM processing, a detailed tomography evaluation and analysis were conducted at two different length-scales in terms of scanned volume and resolution of the tomograms. First, a lower resolution CT characterization was conducted on a GE Phoenix V Tome X M 300 CT System at CIMP-3D. Two types of samples were scanned and reconstructed, including bulk blocks from the build process (50.8 mm by 21.59 mm by 19.05 mm, as shown in Figure 3.2a) and net-shape dog-bone specimens (3 mm thick and 50.8 mm in overall length by 8.9 mm in width, while the gauge section is 17.5 mm long by 3.5 mm in width, as shown in Figure 3.2b). The CT characterization had a resolution of 30 µm per voxel (as 1680 voxels represented the longest dimension of 50.8 mm). Next, a higher resolution synchrotron based X-ray micro-computed tomography (µXSCT) was conducted on 10 mm x 1 mm x 1 mm coupons extracted from the bulk of the blocks at 2-BM of the Advanced Photon Source at Argonne National Laboratory. The µXSCT characterization consisted of 1500 projections taken over 180° continuously rotated at 1°/s with a 100 ms exposure time in white beam mode. The µXSCT characterization had a resolution of 0.65 µm per voxel (as 1532 voxels represented the longest dimension of 1 mm). Tomographic reconstructions were performed on the acquired

radiographs using a gridrec algorithm [100,101] implemented in tomographic data processing software, TomoPy 1.0.0 [102].

Image processing consisted of both thresholding, using the Ostu method [103] and segmentation, which were performed using a combination of ImageJ [104,105] and Avizo 9.2.0 software [106]. The segmented rendered volumes are shown in Figure 3.2 to display the porosity. A pore was considered based on the threshold and segmented phase contrast. A reliable volume was determined based on a 2x2x2 surface connected voxel filter (8 voxel minimum – minimum 1.3 μm minimum diameter), whereas a reliable morphology description required a 5x5x5 surface connected voxel filter (125 voxels minimum – minimum 3.25 μm minimum diameter) [19]. Figure 3.2c displays the porosity from the μXSCT characterization with the 125 voxel filter. For visualization, only pores with equivalent diameter of 10 μm or larger in the μXSCT sample are shown in Figure 3.2d. As seen in Table 3.1, the disparity in resolution and scanned volume results in drastically different percentages of porosity. The lower resolution CT scans can capture much larger scanned volumes, but cannot measure small pores that are prevalent in the AM process. Thus, the degree of porosity measured in the μXSCT characterization is significantly higher than the CT characterization. However, due to the small scanned volume inherent to the μXSCT technique, it results in low probability of scanning large pores, since an insufficient volume is probed. Moreover, due to the high surface area to volume ratio of the dogbone specimen, compared to the bulk block, the dogbone specimens contain a significantly larger degree of porosity. The cumulative distribution function (CDF) of the porosity for the different techniques and parts are shown in Figure 3.3a, with the 8 voxel filter applied to each dataset. The μXSCT characterization shows a median pore size of 4 μm. Moreover, the data was analyzed to determine the minimum distance to an adjacent pore (for each pore analyzed). The minimum pore spacing is shown in Figure 3.3b, with the median distance to the closest pore being ~10.5 μm.

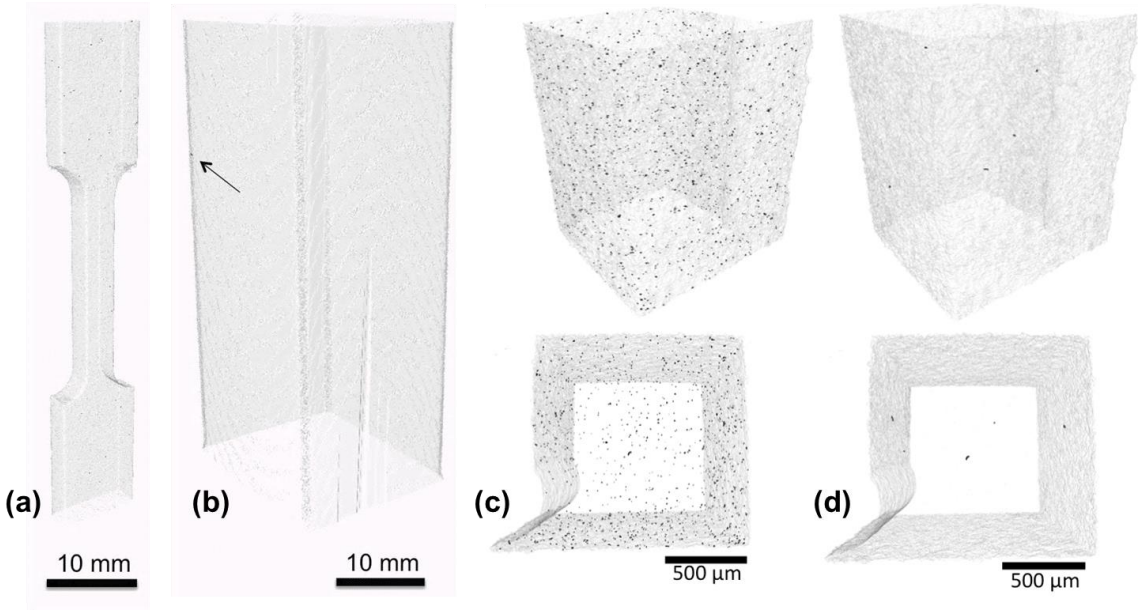

Figure 3.2 Tomography reconstruction showing porosity of IN718 for various samples and settings: (a) CT sample of dogbone (b) CT sample of bulk block, (c) µXSCT sample from bulk – with 5x5x5 voxel filter, and (d) µXSCT sample from bulk – with 10 µm equivalent diameter filter.

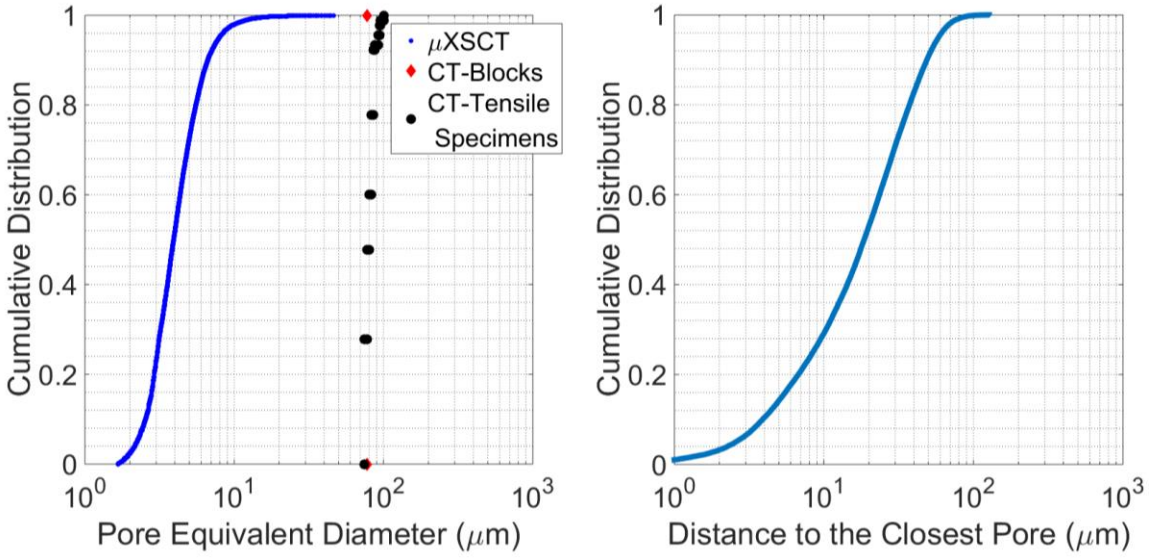

Figure 3.3 Porosity data from tomography reconstruction of IN718 (a) Cumulative distribution of pore equivalent diameter and (b) Cumulative distribution of distance to the closest pore.

Table 3.1 Porosity data using μXSCT and CT.

Sample	Resolution (μm)	Qty	Total volume (mm^3)	Porosity (%)
μXSCT	0.65	8	10.4	4.5×10^{-2}
CT-Blocks	30	2	41878	4.5×10^{-8}
CT-Tensile Specimens	30	3	3960	8.6×10^{-4}

3.4 Mechanical testing

Eight micro-tensile specimens (Figure 3.4(a)) were tested at Element Materials Technology under stress-controlled fatigue loading with a stress ratio (R_σ) of 0.01 and a maximum stress (σ_{max}) of 800 MPa. The samples had a gauge volume of 1 mm x 0.3 mm x 1 mm. The life to failure data obtained from the experiments is shown in Figure 3.4(b), which follows a lognormal distribution[1]. Two modes of failure were observed from post mortem fractography analysis, namely, the facet failure at the bulk of the specimen and failure at a free surface [107], which are also indicated in Figure 3.4(b). Since the macroscopic loading is in high cycle fatigue regime with σ_{max} at ~70% of the material's yield strength [86], the crack initiation life dominates the total life, and for this reason, the failure life will be considered the crack initiation life.

[1] The test for log-normality of the data set $\boldsymbol{X}$ *(*X here represents the failure lives*)* is alternatively posed as a test for normality of log (**X**). The data points are first scaled and centered using the following equation:

$$z = \frac{\log(\mathbf{X}) - \mu}{\sigma}$$

Where, μ and σ are the mean and standard deviation corresponding to log(**X**). Following this, the one sample Kolmogorov-Smirnov test for normality of z was performed using the MATLAB function *kstest*. This returned the h value to be zero indicating that the *kstest* fails to reject the null hypothesis (that the data comes from a normal distribution) at 5% significance level. Thus, the original data set **X** belongs to a log-normal distribution.

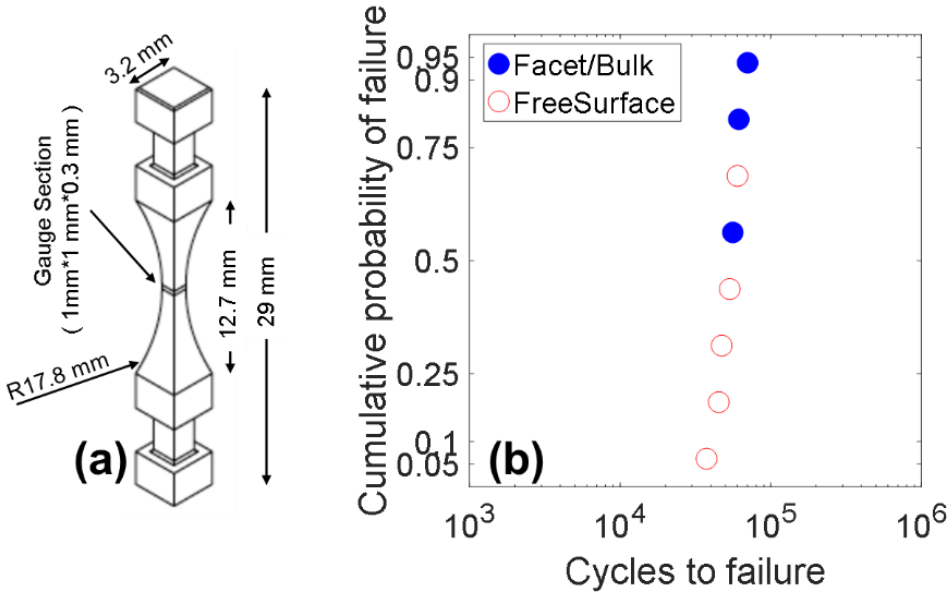

Figure 3.4 (a) IN718 specimen geometry used for fatigue testing, (b) Fatigue life data obtained from testing of eight samples ranging from 37461 to 70161 cycles in life and following a log-normal distribution, and indicating modes of failure, namely facet failure and free surface failure, as observed in the eight specimens from the post mortem fractography analysis.

3.5 Fatigue testing with in situ X-ray experimentss

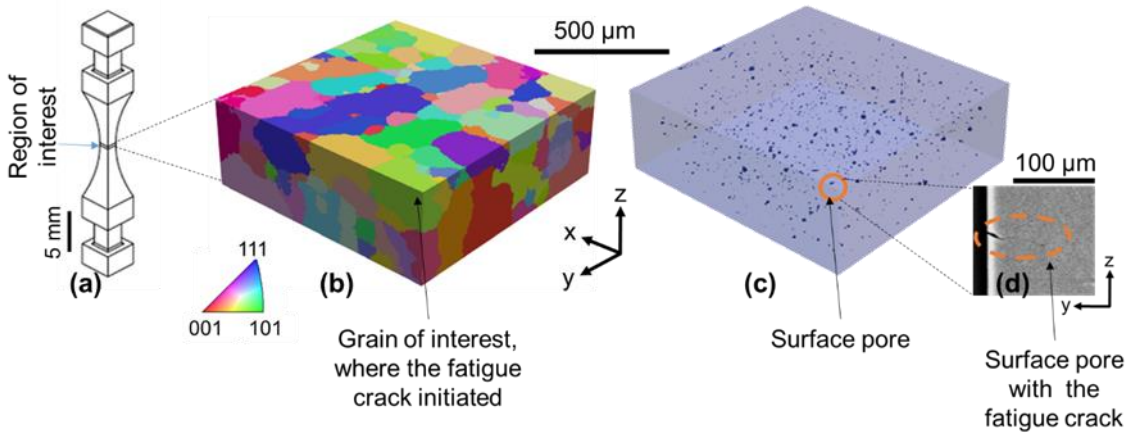

Figure 3.5(a) Schematic of the IN718 test specimen used for in situ fatigue testing with the ROI at the center as shown, (b) 3D NF-HEDM microstructure map of the ROI with grains colored via an inverse pole figure representation, (c) 3D porosity map reconstructed from µCT within the ROI along with the encircled surface pore where the fatigue crack initiated, and (d) µCT image of the fatigue crack from the surface pore.

The in situ high cycle fatigue (HCF) testing was conducted at beamline 1-ID of the Advanced Photon Source (APS) at Argonne National Laboratory using a beam energy of 71.676 keV (λ=0.0172972 nm). The specimen was subjected to fatigue loading from 0 to 71000 cycles with an R ratio of 0.01 and was cycled between 10 MPa (σ_{min}) and 800 MPa (σ_{max}) at a frequency of 20 Hz. This experiment was conducted in two parts: (i) 0 to 20 cycles and (ii) 20 to 71000 cycles. The first part of the experiment was performed to initialize the CPFE model, and the second part of the experiment was performed to obtain crack initiation data for use in validation efforts. A suite of non-destructive 3D high-energy X-ray characterization techniques, conducted in transmission geometry, namely, in situ NF-HEDM, FF-HEDM, and μCT were employed in this experiment.

During the first part of the experiment (0 to 20 cycles), NF-HEDM and FF-HEDM scans were performed on a 355 μm tall region of interest (ROI) encompassing the gauge section of the specimen, as shown in Figure 3.5(a). In the second part of the experiment (20 to 71000 cycles), FF-HEDM and μ-CT were performed on a 3 mm tall section (including the ROI). During the second part of the experiment, the larger region was necessary to capture the surrounding microstructure to the ROI and the appropriate boundary conditions for subsequent modeling activities and ensure the crack initiation location was captured in the ROI. A rotational and axial motion system [108] was used to apply cyclic load to the test specimen. This device is capable of simultaneously applying axial load, while rotating the sample, without obstructing the path of the X-ray beam. To aid with feature tracking across the aforementioned 3D characterization techniques, a gold cube affixed on the gauge section was used as a fiducial marker [109]. The details of each in situ high-energy X-ray technique along with the experimental set-up and data acquisition will be outlined in the forthcoming paragraphs.

FF-HEDM was used to obtain the grain centroids, grain-averaged orientations, and the evolution of the grain-averaged elastic strain tensors (and hence, grain-averaged stresses) with respect to the HCF loading cycles. The experimental setup for both parts of the experiment was calibrated using Ceria (CeO_2) powder and Au patterns. A GE area detector (2048 x 2048 pixels, 200 μm pitch), placed ~ 880 mm away from the specimen was used to capture the diffraction peaks corresponding to the grains that satisfied Bragg's condition every 0.25°, while the specimen was rotated 360° about its loading axis. At this distance, eight diffraction rings (corresponding to the {111}, {020}, {220}, {131}, {222}, {040}, {331}, and {240} crystallographic planes) were captured on the

detector. The first two rings were attenuated with a lead tape to shield the detector from their high diffracted-intensity measures. The FF-HEDM data was reconstructed by employing the Microstructural Imaging and Diffraction Analysis Software (MIDAS) [110,111] using a completeness value of 0.7. A spatial resolution of ~50 μm for the grain centroids, an angular resolution of 0.1^{o} for grain orientations and a resolution of 1e-4 for the lattice strains were achieved using the current set-up. Further details regarding both parts of the experiment are as follows:

- For the first part of the experiment (0 to 20 cycles), the scans for the ROI were obtained at 0 cycle, 1 cycle, 2 cycles, 5 cycles, 10 cycles, and 20 cycles, using a 50 μm tall beam. Seven boxes spanning the ROI (the specimen was translated vertically by 50 μm between each scan) were scanned to characterize the microstructure. Diffraction spots from six complete Debye-Scherrer rings ({220}, {131}, {222}, {040}, {331}, and {240} planes) were used for analysis and reconstructing FF-HEDM data.
- For the second part of the experiment (20-71000 cycles and 3mm tall section), 24 boxes stacked along the loading axis were scanned with a beam of height 125 μm. Scans were taken at 20, 200, 2K, 15K, 43K, 51K, 59K, and 71K cycles. Diffraction spots from the first four Debye Scherrer rings (belonging to {111}, {020}, {220}, and {131} crystallographic planes) were used to reconstruct the FF-HEDM data.

NF-HEDM was used to obtain the 3D grain map of the ROI at the initial state (0 cycle). Line focused beams, 2 μm tall and 2 mm wide, were used to acquire 71 scans to characterize the ROI. This NF-HEDM data was recorded every 0.25°, while the sample was rotated by 180° about its loading axis. A detector with a 3 mm field of view and 1.5 μm x 1.5 μm pixel size captured the diffraction data at two distances from the sample, ~ 5 and 7 mm, which helped to maximize the spatial resolution of this technique, and accurately determine the source and direction of the diffracted beam corresponding to each diffracted spot. The experimental setup was first calibrated using a gold cube with sharp grain features. These calibration parameters were further refined (using grains from the specimen itself) using an optimization technique until consistently well-defined grain boundaries were obtained throughout the reconstructed near-field slice. NF-HEDM scans were reconstructed using MIDAS, wherein a triangular grid with an edge size of 5 μm was used to obtain a high signal to noise ratio. The grain orientations obtained from FF-HEDM were

used to seed the forward modeling search-space within an orientation tolerance of 4°. The triangular mesh (containing orientation information) was then re-gridded onto a 3D voxel-based structure with a resolution of 2μm x 2μm x 5μm. This was followed by a segmentation procedure by allowing a maximum misorientation of 2° between adjacent voxels to obtain distinct grains. The 3D grain map of the ROI thus obtained is shown in Figure 3.5(b).

μCT was used to obtain the following information: (a) porosity map, (b) the location of microcrack initiation during the fatigue testing, (c) the perimeter of the ROI to create a mask for the grains reconstructed via NF-HEDM, and (d) the location of the gold cube in order to facilitate registration among the three characterization techniques. To scan the 3 mm region, three 1.2 mm tall boxes (stacked along the z-axis) were scanned with a 1.2 mm tall x 2 mm wide beam such that there was a 100μm overlap between two consecutive boxes on either end. A high resolution tomography detector, with a pixel size of 1.17 μm, was used to capture the raw data ~90 mm away from the specimen (at 20, 15K, 43K, 51K, 59K, and 71K cycles). To capture fine features (such as pores and micro cracks), radiographs were taken every 0.1° while the specimen was held in tension (at σ_{max}) and rotated by 360° about its loading axis. This resulted in 3600 radiographs, which were used to reconstruct the specimen volume using an in-house APS MATLAB code [112]. Further post-processing was done using a combination of MATLAB and ImageJ [105], and visualization of the reconstructed 3D volume was done using ParaView [113]. A spatial resolution of 2.34 μm was achieved with the current detector set-up. The porosity map within the ROI is shown in Figure 3.5(c). A fatigue micro crack was observed at a surface-connected pore after 51K cycles from the reconstructed data, which is depicted in Figure 3.5(d). Since the μCT scans were performed at discrete intervals, the exact time point of crack initiation is not known. However, the crack must have nucleated between 43K and 51K cycles.

4. CRYSTAL PLASTICITY BASED MODELING FRAMEWORK

In this chapter, the major elements of a crystal plasticity based framework is described in detail. This includes the creation of 3D virtual microstructures, description of constitutive model, calibration of the material parameters, and the regularizing schemes used in post-processing of results. Some aspects of this workflow process has been published in [114].

4.1 Creation of 3D virtual microstructures

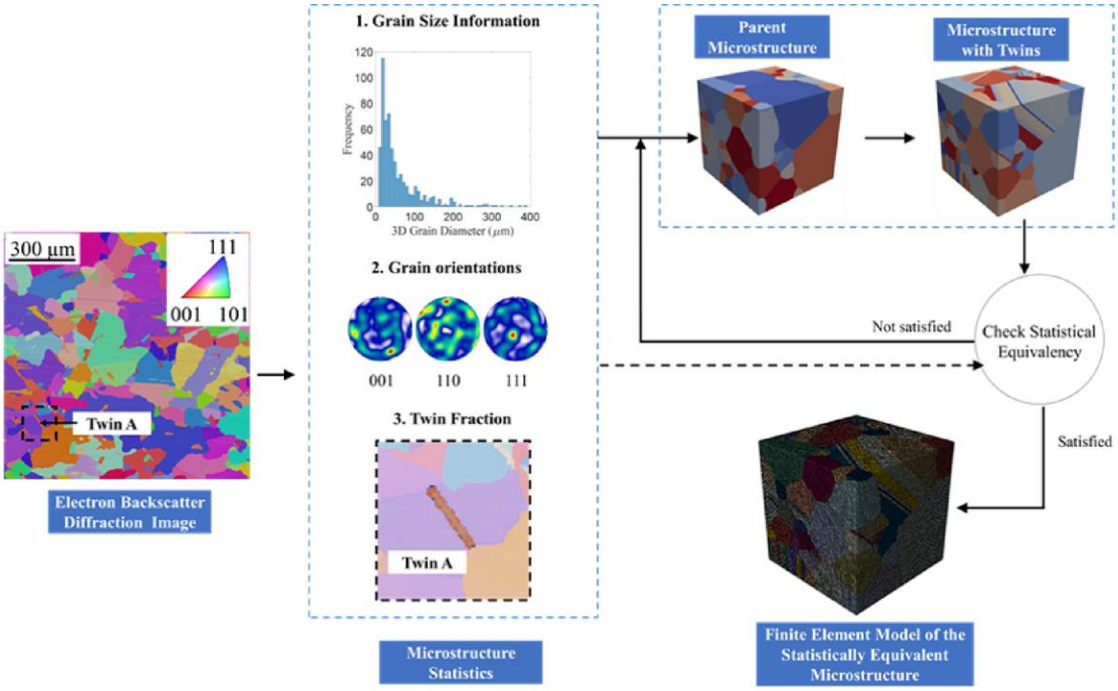

Figure 4.1. Automated creation of a 3D finite element model which is statistically representative of the EBSD microstructural attributes.

The steps involved in the creation of the discretized polycrystalline microstructural instantiations starting from the electron backscatter diffraction (EBSD) data is shown in Figure 4.1. In the first step, the microstructural statistical information, namely, the grain sizes and orientations and twin length fraction are obtained from the EBSD data. The grain sizes and orientations are extracted using the reconstruction filters in DREAM.3D [115]. The reconstruction procedure involves: (a) cleaning the experimental noise in the EBSD data, (b) segmentation of grains using a

misorientation threshold value[2], and (c) measuring grain sizes and orientations. The reader may refer to the DREAM.3D reconstruction tutorial and associated algorithms for additional details of these procedures [116,117]. The grain size corresponds to the diameter of an equivalent circle, as is appropriate for equiaxed grain materials, and the orientations are obtained in the form of Bunge Euler angles. From a single EBSD scan, only the 2D grain sizes are available, hence stereological methods are necessary to obtain the 3D grain sizes (diameter of the equivalent sphere) for accurate microstructure representation. The 2D grain sizes are converted to 3D data by multiplying a stereological factor of $4/\pi$ [117]. Annealing twins are generally prevalent in Ni-based superalloys, including IN718, owing to the material's relatively low stacking fault energy, and these features need to be included in subsequent modeling activities due to their significant effect on the corresponding mechanical behavior. The twin boundaries are identified from the EBSD data using the procedure detailed in Ref. [118]. Later, the twin length fraction, defined as the total length of the twin boundaries to that of all the grain boundaries, is obtained using DREAM.3D.

The second step involves the creation of 3D synthetic microstructures, including twins, using the statistics as obtained in the previous step. The synthetic building filters within DREAM.3D are used to obtain the 3D synthetic microstructure, which we refer to as parent microstructure. The inputs to the parent microstructure creation are the 3D grain sizes and the orientation information (obtained in the previous step), desired volume of the microstructure, and the size of a voxel.

The primary steps in the parent microstructure creation involve packing the grains inside the specified volume and matching the crystallography to the specified texture; the reader is referred to Refs. [116,117] for additional details. The parent microstructure generation is random in nature, i.e., different microstructures are obtained when the DREAM.3D pipeline is run multiple times with the same set of inputs. The parent microstructure is deliberately created with a higher mean grain size[3], as compared to the actual mean obtained from the EBSD, which is necessary to compensate for the reduction in the mean grain size after insertion of twins. The twins are inserted

[2] For a material with a random texture, as is the case for the present material, a misorientation threshold value of 5^o is generally used. For highly textured materials, a misorientation threshold value of ~1^o-2^o would be more appropriate.

[3] The increased grain size is dependent on the twin length fraction of the material. For the present material, the twin length fraction is ~0.5 corresponding to an increase of the mean parent grain size of 30%. In the present analysis, the parents and twins are treated independently in determining the grain size.

into the parent microstructure using the methodology described in Ref. [119]. The segmentation of a twin is performed along a randomly chosen {111} plane in a randomly chosen grain. The Euler angles for the twin are assigned such that the misorientation between the parent and twin is a 60^o twist with respect to the <111> plane normal. Twins are restricted to be inserted in large grains (greater than 80% of the largest grain) to preserve the average grain size of the microstructure with twins. The maximum number of twins per grain is restricted to three to avoid the creation of very small grains (diameter less than the minimum 3D grain size) after twin insertion. Also, only one twin variant per grain is permitted to avoid the intersection of twins. The creation of the parent microstructure, as well as the twin insertion process, is an iterative process and is continued until statistical equivalency is achieved between the attributes of the synthetic microstructure with twins and the EBSD data. The statistical equivalency criteria are defined using three metrics: (a) within 5% of the average grain size, (b) within 5% of the twin length fraction[4], and (c) within 2% of the Taylor factor with respect to the applied loading direction of the simulation. The Taylor factor serves as a scalar measure of the texture [120–122]. A tighter bound is enforced on the Taylor factor criterion to preserve the sensitivity of the mechanical response to the texture and a 5% tolerance for the grain size is acceptable as the crystal plasticity model used in the present study is length scale independent. The microstructure instantiation containing twins is referred to as the statistical equivalent microstructure (SEM) throughout the remainder of this dissertation. Fifteen SEMs are created for this study. Each SEM is a cube of 300 μm length. The number of grains in the SEMs vary from 190-204, which is sufficient to capture the random texture and the homogenized stress-strain behavior at the macroscale [5].

The final step involves the creation of a volume mesh of the SEMs for subsequent CPFE simulations. First, non-smooth surface meshes of the grain boundaries are obtained using DREAM.3D. Second, these non-smooth surface meshes are smoothed using the Laplacian smoothing algorithm available within DREAM.3D. The grain boundary smoothing is an important step to obtain realistic grain morphologies. The reader is referred to Ref. [116] for the usage of relevant DREAM.3D filters[5]. Third, the 3D volume mesh for each grain is obtained from the

[4] For the 3D synthetic microstructures, area fraction of the twins is estimated and is used to compare with the length fraction of twins obtained from 2D EBSD.

[5] Laplacian smoothing requires multiple parameters as input. In this work, the default parameters given in DREAM.3D software are used.

smooth surface mesh using Gmsh [123]. Finally, all grain meshes are combined using Gmsh to obtain the mesh for the entire SEM volume while maintaining the compatibility between nodes at the grain interfaces. Linear tetrahedron elements (C3D4) are used in this study.

The above procedure is automated within an in-house MATLAB program. Thus, the entire workflow, including calling the necessary DREAM.3D pipelines, twin insertion, identifying statistical equivalency, grain boundary smoothing and meshing, and volume meshing in Gmsh, is completed with a single execution of the program, via scripting between the various suite of programs and algorithms. Hence, a set of SEMs can be quickly created, which can be used to study the role of microstructure variability on the associated mechanical response. The automation of this process ensures that the associated features are statistically equivalent and thereby the input microstructure to the CP model is reliable. The 3D SEMs serve as input to CPFE simulations discussed in the forthcoming chapters 5 and 6.

4.2 Crystal plasticity model

A phenomenological CP model [6,124,125] is used, which considers the twelve FCC slip systems: $\langle 110 \rangle \{111\}$. The model is incorporated in ABAQUS within a user-defined material subroutine (UMAT). The kinematics of slip is captured using the multiplicative decomposition [126] of the total deformation gradient, $\mathbf{F}$, as

$$\mathbf{F} = \mathbf{F_e}\mathbf{F_p} \tag{4.1}$$

Here, $\mathbf{F_e}$ and $\mathbf{F_p}$ are the elastic and plastic portions of the total deformation gradient, respectively. The plastic velocity gradient, $\mathbf{L_p}$, is related to the shearing rates, $\dot{\gamma}^{\alpha}$, on a slip system α as

$$\mathbf{L_p} = \sum_{\alpha=1}^{12} \dot{\gamma}^{\alpha} \mathbf{s}^{\alpha} \otimes \mathbf{n}^{\alpha} \tag{4.2}$$

Here, $\mathbf{s}^{\alpha}$ is the slip direction and $\mathbf{n}^{\alpha}$ is the slip plane normal. A Hutchinson type flow rule [127] is used to relate the shear strain rates to the resolved shear stress, τ^{α}, as

$$\dot{\gamma}^{\alpha} = \dot{\gamma}_0 \left| \frac{\tau^{\alpha} - \chi^{\alpha}}{g^{\alpha}} \right|^{n} \operatorname{sgn}(\tau^{\alpha} - \chi^{\alpha}) \tag{4.3}$$

where $\dot{\gamma}_0$ is the reference shear strain rate; g and χ are the reference stress and back stress, respectively; n is the inverse strain-rate sensitivity exponent. The evolution laws for the reference and the back stresses are based on the Armstrong-Frederick type equations [128,129] and are given by

$$\dot{g}^{\alpha} = H \sum_{\beta=1}^{12} q^{\alpha\beta} \left|\dot{\gamma}^{\beta}\right| - H_d g^{\alpha} \sum_{\beta=1}^{12} \left|\dot{\gamma}^{\beta}\right| \tag{4.4}$$

$$\dot{\chi}^{\alpha} = A\dot{\gamma}^{\alpha} - A_d \chi^{\alpha} |\dot{\gamma}^{\alpha}| \tag{4.5}$$

where H and H_d are the direct hardening and dynamic recovery coefficients, respectively, for the reference stress; A and A_d are the direct hardening and dynamic recovery coefficients, respectively, for the back stress; $q^{\alpha\beta}$ is the hardening matrix which has values of 1 for self-hardening (diagonal terms) and 1.2 for latent hardening (off-diagonal terms) [130]. There are eight CP parameters: $\dot{\gamma}_0$, n, g_0 (initial value of g), H, H_d, χ_0 (initial value of χ), A, and A_d to be estimated, which are obtained using GA as described below.

4.3 Parameter estimation using genetic algorithm

In this study, the objective is to obtain a combination of the eight CP parameters that would accurately capture the macroscopic response of the material (both forward and reverse behavior) under uniaxial loading. The simplest approach is to manually adjust the CP parameters and carry out a series of simulations until the desired homogenized output is achieved. However, such an approach is time consuming and not suitable to accurately capture the reverse loading behavior (Bauschinger's effect) because the parameters are highly coupled and cannot be sequentially changed with a high degree of precision. Hence, the CP parameter estimation is posed as an unconstrained optimization problem given by:

$$\min_{\boldsymbol{\theta}} \; f(\boldsymbol{\theta}) = \sqrt{\frac{1}{N}\sum_{i=1}^{N}\left(1 - \frac{S_{sim}^{i}(\boldsymbol{\theta})}{S_{expt}^{i}}\right)^{2}} \tag{4.6}$$

where $\boldsymbol{\theta}$ is the set of CP parameters; S^i_{expt} is the stress value from the experiment and $S^i_{sim}(\boldsymbol{\theta})$ is the volume averaged stress value along loading direction from the CPFE simulation corresponding to the i^{th} point on the macroscopic stress-strain curve; N is the total number of equidistant points chosen on the stress-strain curve.

The optimization problem could be solved using many different approaches, including: (a) machine learning techniques, (b) gradient based optimization methods, and (c) non-gradient based optimization methods. The application of machine learning techniques requires a significant quantity of training data and, hence, are not chosen in this work. To make use of the gradient based

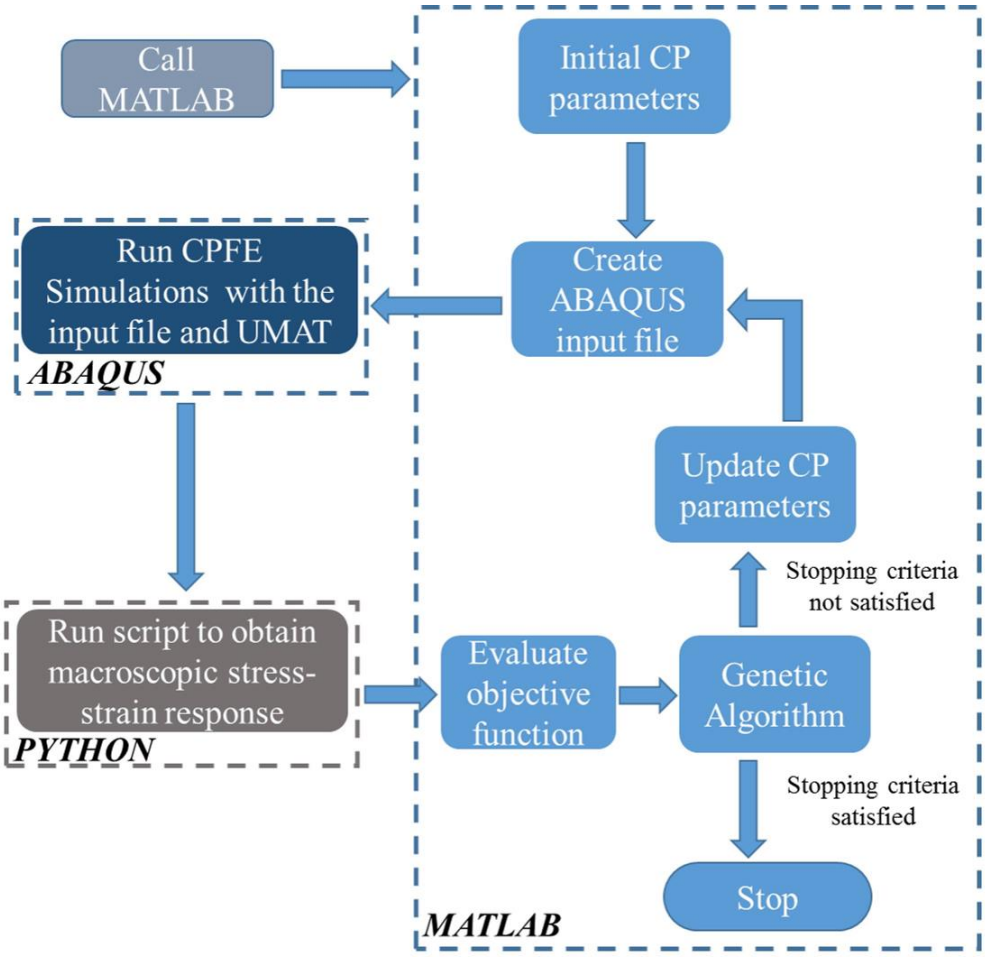

Figure 4.2. The schematic of an automated framework for the estimation of crystal plasticity parameters using a genetic algorithm.

approaches, one needs to numerically evaluate the gradients at $\boldsymbol{\theta}$, because $f(\boldsymbol{\theta})$ does not have a closed-form expression in terms of $\boldsymbol{\theta}$. Each function evaluation at $\boldsymbol{\theta}$ involves a CPFE simulation to obtain $S^i_{sim}(\boldsymbol{\theta})$. The numerical evaluation of gradients requires at least 9 CPFE simulations (using either forward or backward difference schemes) for each iteration and hence, is too computationally expensive. Moreover, the continuity and differentiability of $f(\boldsymbol{\theta})$ is not guaranteed for all $\boldsymbol{\theta} \in \mathbb{R}^8$, where $\mathbb{R}^8$ is the eight-dimensional space of real numbers corresponding to the number of CP parameters, a convergence using any gradient based method is not guaranteed. So, a non-gradient based method is well-suited to solve the problem given by Eqn. (4.6), and due to its simplicity, a GA is chosen for this work. The automated framework for the GA implementation in a high performance computing domain involving multiple software platforms is shown in Figure 4.2. The ABAQUS input file, containing mesh geometry, CP parameters ($\boldsymbol{\theta}$), and boundary conditions, is created using MATLAB. Subsequently, CPFE simulations are performed in ABAQUS. Next, $S^i_{sim}(\boldsymbol{\theta})$ is extracted from ABAQUS using a Python script. Afterwards, $f(\boldsymbol{\theta})$ is evaluated in MATLAB. The stopping criterion is set as $f(\boldsymbol{\theta}) \leq 0.03$, which corresponds to the percentage error determined to be acceptable in calibrating the model to the macroscopic experimental stress data (S^i_{expt}). The built-in MATLAB function `ga` is used for updating the parameters if the stopping criterion is not met.

Based on a sensitivity study with different mesh sizes, a coarse mesh of size 7.5 μm was found to yield a similar macroscopic stress response as compared to fine meshes and hence, was chosen for the fitting process. The model reduction resulted in a computational cost saving of ~100X (compared to a mesh size of 3 μm)[6], which is necessary to make this a tractable means for parameter estimation in an engineering workflow. The maximum number of generations (corresponds to global iteration number) is taken as 10 and the population size (corresponds to sub-iterations within each generation) is given as 100. For most cases, the convergence was achieved within a generation or two. The number of model evaluations could be estimated as the population size × (number of generations + 1).

[6] One CPFE simulation, comprised of two loading cycles, in the present study with a mesh size of 7.5 μm takes about 12-18 minutes using 160 processors.

Also, due to the uncertainty in values for the single crystal elastic constants of IN718 in the literature, these constants were obtained by back fitting the elastic portion of the experimental stress-strain response using the GA. The upper and lower bounds for the cubic constants (C11, C12, and C44) for the fit were taken from the literature [131–134]. All the model parameters thus obtained via the use of GA are shown in Table 4.1. The model calibration with the experimental macroscopic stress-strain curve for ten cycles until saturation of the hysteresis loops is shown in Figure 4.3.

Table 4.1 Parameters used in the CP simulations.

No.	Parameters	Values
1	C11	225.7 MPa
2	C12	151.2 MPa
3	C44	112.3 MPa
4	$\dot{\gamma}_0$	0.0004 s^{-1}
5	m	38
6	g_0	380 MPa
7	H	7800 MPa
8	H_d	19
9	A	14000 MPa
10	A_d	84
11	χ_0	10 MPa

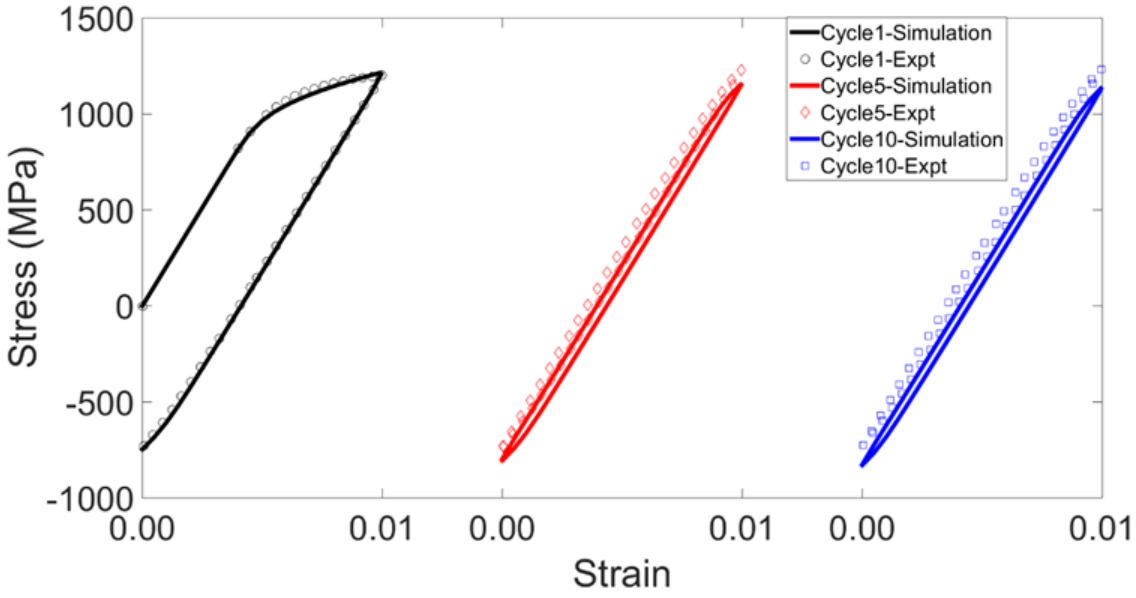

Figure 4.3. Comparison of the macroscopic stress-strain behavior of experiments and simulations using calibrated CP parameters until ten cycles.

4.4 Regularizing schemes

The presence of distorted elements in the meshing of 3D polycrystalline microstructures is unavoidable using the current workflow procedure. The distorted mesh elements arise, especially due to the smoothing of the grain boundaries to obtain realistic grain morphologies. The distorted elements are undesirable because they result in spurious stress values. Thus, it is necessary to identify the elements with the poor quality and then, mitigate their effects using regularization schemes. The quality of each element in each SEM is assessed by using the following geometrical measures of the tetrahedron as defined by β and γ.

$$\beta = \frac{\mathrm{CR}}{3 * \mathrm{IR}} \tag{4.7}$$

$$\gamma = \frac{S_{rms}^3}{8.48 * \mathrm{V}} \tag{4.8}$$

where CR is the radius of the circumscribed sphere, IR is the radius of the inscribed sphere, $S_{rms}\left(=\sqrt{\frac{1}{6}\sum_{i=1}^{6}(S_i)^2}\right)$ is the root mean square value of the edge lengths (S_i), and V is the volume of the tetrahedron. The schematic of a mesh element with relevant geometrical quantities (as in Eqns. (4.7) and (4.8)) are shown in Figure 4.4(a, b). The good quality elements correspond to $\beta \in [1,3]$ and $\gamma \in [1,3]$, and the rest of the elements are considered as poor quality elements [135]. The distribution of the mesh quality metrics for one of the SEMs is shown in Figure 4.4. Different volume averaging schemes, namely non-local averaging [66], band averaging [61], and the grain averaging, are used to mitigate the effects of the poor-quality elements, and to report consistent results that are mesh independent.

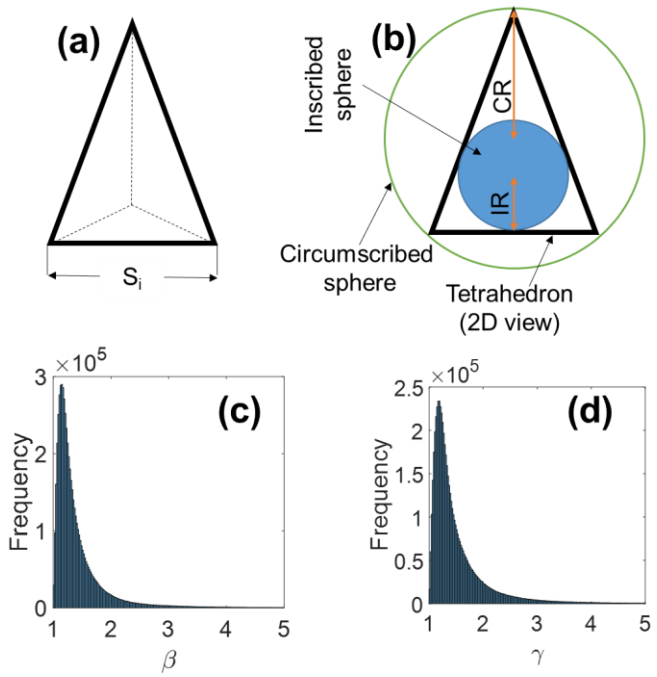

Figure 4.4 (a) 3D schematic of a tetrahedron with the edge length denoted by S_i for a side i, (b) 2D representation of a tetrahedron with the circumscribed sphere (with a radius CR) and the inscribed sphere (with a radius IR) shown, and distribution of mesh quality metrics: (c) β and (d) γ for all the elements within SEM #1. For both the quality metrics, values greater than three represent poor quality elements [135].

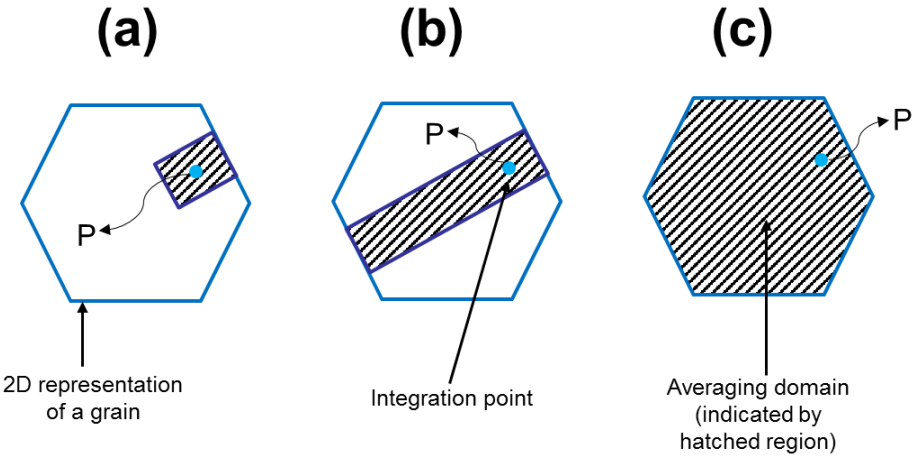

Figure 4.5 2D schematic of the different regularization schemes used in the post-processing of the micromechanical fields: (a) non-local averaging, (b) band averaging, and (c) grain averaging, defined at an integration point, P.

In the non-local averaging scheme, at each integration point (say P), a cuboidal volume as defined by the slip vector, slip normal, and the orthonormal in-plane vector is bounded such that the integration point is at the centroidal position of the averaging volume (Figure 4.5(a)). The bounded volume will enclose multiple integration points, and the average of all the field values inside the bounded volume is calculated. The process is repeated for all the integration points in the microstructure. Since there are twelve slip systems in an FCC polycrystal, we have twelve averaged values corresponding to each slip system. The maximum value among the twelve values is assigned to the point P. In performing the averaging, the volume is not allowed to cross the grain boundary as shown in Figure 4.5(a). The averaging scheme closely aligns with the physics of slip deformation, thereby retaining the associated gradients in the micromechanical fields. Also, by restricting the averaging domain to be within a grain enables preservation of the gradient developed across the grain boundary due to kinematic compatibility and elastic anisotropy. Band averaging is the limiting case of the non-local averaging scheme. When the cuboidal volume is extended along the slip vector, and the orthonormal in-plane vector is extended until the exterior surfaces of the grain, we obtain the band averaging volume (Figure 4.5(b)). In the grain averaging scheme, for each integration point within a grain, all the field values within the grain are averaged and assigned to that integration point. Therefore, each grain will have one unique value for a given field quantity.

The poor-quality elements, elements near the simulation boundary constraints, and elements near the pore are not included in the regularization calculations to avoid bias in the resulting values.

The size of the non-local averaging domain is dependent on the local finite element size and the loading conditions (low cycle fatigue or high cycle fatigue). In the low cycle fatigue conditions, the size of the averaging volume is taken as ~ 3-4 elements with respect to the slip direction and ~ 2-3 elements in the transverse directions based on a sensitivity study. This volume satisfies the requirement of smoothing spurious values and preserving the localization of the micromechanical fields. The volume corresponding to each integration point would be different due to the restrictions placed on the domain to be within the grain. In the high cycle fatigue conditions, as the macroscopic loading is less than the material's yield strength, some elements in the SEM will undergo plastic deformation, while the remaining elements will still be elastically loaded. Hence it is essential that the averaging volume is small to capture microplasticity, but at the same time, it has sufficient elements to result in mesh independent results. Hence, the size of the non-local averaging volume is chosen as 2*2*2 elements, and the average number of elements in the non-local averaging volume is found to be ~ 25, which is sufficient to smooth out oscillations.

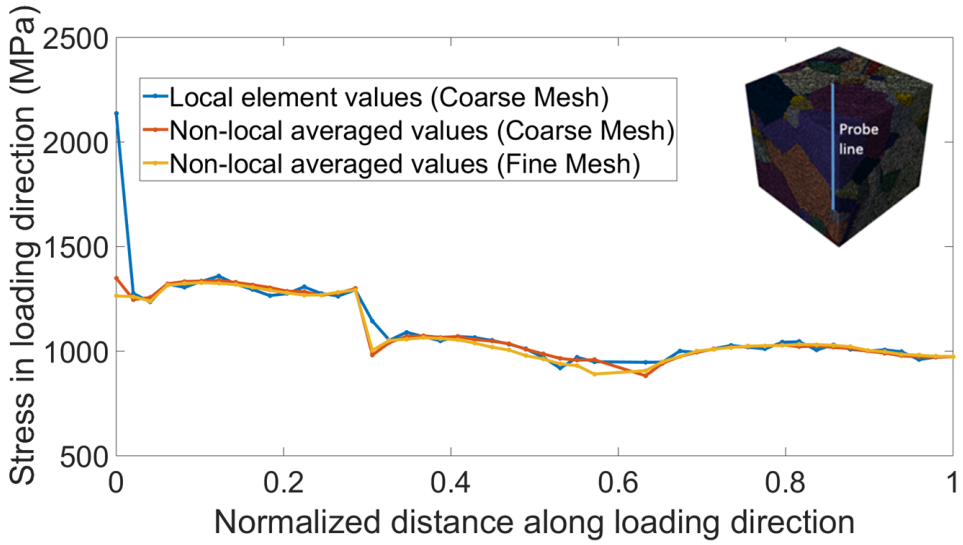

Figure 4.6 Comparisons of the stress values along a random probe line evaluated from the local element values of the coarse mesh, non-local averaged values obtained from coarse mesh, and non-local averaged values obtained from fine mesh.

Figure 4.6 shows the comparisons of the stress values along a random probe line in the FE microstructure in the loading direction. The three plots shown in Figure 4.6 correspond to the local element values obtained from the coarse mesh, non-local averaged values obtained from the coarse mesh, and the non-local averaged values obtained from the fine mesh. The details of the coarse mesh and the fine mesh are given in Table 4.2. The smoothing of the stress values due to the application of the averaging technique is evident from Figure 4.6 and the mesh sensitivity study using the non-local averaged stress values indicate that the coarse mesh shows converged results in comparison to the fine mesh, which justifies the choice of the coarse mesh in our simulations.

Table 4.2 A comparison between the coarse mesh and the fine mesh for the CP-FE models with respect to element size, number of nodes and elements, and computational time for one cycle.

Finite element model	Element Size (μm)	No. of Nodes	No. of Elements	Simulation time for 1 cycle
Coarse Mesh	3.2	0.7 M	3.8 M	~ 1 day
Fine Mesh	2	2.2 M	13.7 M	~ 10 days

5. ESTIMATION OF CRITICAL POROSITY CHARACTERISTICS

In this chapter, a CPFE based modeling framework is described to predict the limiting cases of porosity (pore size and proximity within a pore cluster) affecting the fatigue crack initiation of SLM IN718, which also addresses an existing gap in the current literature. Cyclic simulations are performed for multiple instantiations of the 3D microstructure containing pores of varying pore sizes, locations relative to the surrounding microstructure, and proximity between adjacent pores. Multiple instantiations in this study allow variation in both crystallographic orientation and grain morphology to understand the resulting sensitivity with different microstructures. Within this chapter, Section 5.1 presents the problem formulation with the results, and Sections 5.5 and 5.6 provide the discussions and conclusions of this work, respectively. The results and analysis provided in this chapter have been published in [66].

5.1 Input microstructures

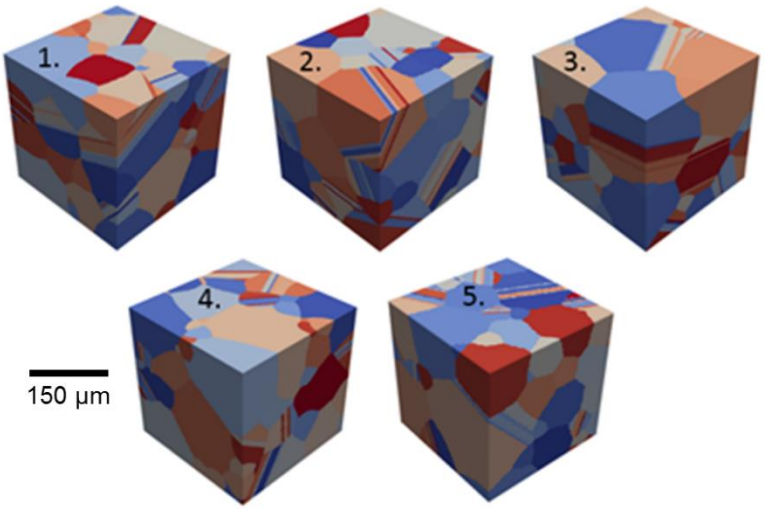

Figure 5.1 SEMs used as input to the CP-FE simulations that are statistically representative of the EBSD microstructural attributes and have similar macroscopic strength behavior.

A total of 5 SEMs (Figure 5.1) were created as input to the CPFE simulations that are statistically representative of the EBSD microstructural attributes and have similar macroscopic strength behavior. Each SEM is a cube of dimension 300µm. The number of grains within the SEMs varies

from 189-205. Linear tetrahedron elements (C3D4) are used in meshing. The global mesh size for each SEM is prescribed as 3.2 μm based on a sensitivity study.

5.2 Boundary conditions

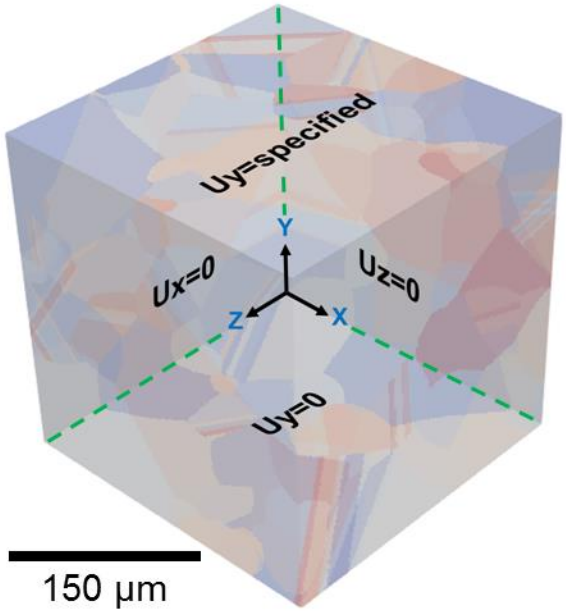

Figure 5.2 Displacement boundary conditions applied on the boundary faces of the microstructure model used in the CP-FE simulations. Ux is zero on the x=0 face, Uy is zero on the y=0 face, Uz is zero on the Z=0 face, Uy is specified on the top face, and the other two faces (X or Z=300 μm) are free.

Each CP-FE model under investigation is subjected to strain controlled fatigue cycling from 0 to 1%. A total of 47 CP-FE simulations are conducted within this study, and the computational time necessary for each simulation on 160 processors is ~4-5 days. As discussed in Section 5.4.2, the critical pore size estimation involves a comparison within the spatial distribution of the damage metrics. From a single CP-FE simulation, it was found that the spatial distribution of the damage metrics had a similar trend in terms of the most probable location of failure for both four cycles and ten cycles. Hence, the present analysis based upon the computational costs and identifying the most likely location of crack initiation, relies upon the results of CP-FE simulations after four loading cycles.

The boundary conditions used in the FE simulations are shown in Figure 5.2 and are consistent with those proposed in [136]. Ux, Uy, and Uz represent the displacements in x, y, and z directions, respectively. Ux is zero on the x=0 face, Uy is zero on the y=0 face, Uz is zero on the Z=0 face,

Uy is specified on the top face (Figure 5.2) based on the applied strain values, and the other two faces (X or Z = 300 μm) are free. In this work, we are primarily interested in the role of porosity in SLM IN718, and the presence of residual stress gradients and surface roughness effects are not taken into account.

5.3 Damage indicator parameters

To understand the fatigue behavior, four damage indicator parameters (DIPs) have been calculated in this study based on their prevalence to fatigue crack initiation as previously discussed in [5], namely, the plastic strain accumulation (PSA), elastic stress anisotropy (ESA), change in resolved shear stress (ΔRSS) and the triaxiality (Triax). PSA indicates the localization of plastic slip in the microstructure [137,138] and strain localization is well-known to be a precursor to crack initiation [39,139]. PSA is obtained as the time integral of the scalar product of the plastic velocity gradient, L_p,

$$\dot{p} = \sqrt{\frac{2}{3}\mathbf{L_p}:\mathbf{L_p}} \tag{5.1}$$

$$\text{PSA} = \int \dot{p}dt \tag{5.2}$$

ESA gives a scalar measure of the lattice incompatibility tensor [140] and is representative of the internal stresses caused by geometric mismatch of the slip system at the grain boundary.

$$\alpha = \text{Curl}\left(\mathbf{F_p}\right) = -\text{curl}\left(\mathbf{F_e}^{-1}\right) \tag{5.3}$$

$$ESA = \sqrt{\frac{3}{2}\alpha:\alpha} \tag{5.4}$$

RSS provides a measure of the shear stress on a slip system which drives the plastic deformation. ΔRSS is obtained between the maximum and the minimum strain points during a loading cycle, and the value of ΔRSS is taken as the maximum value over the 12 slip systems, β.

$$\tau^{\beta} = \boldsymbol{\sigma}:(s^{\beta} \otimes n^{\beta}) \tag{5.5}$$

$$\Delta\text{RSS} = \max_{\beta} \Delta\tau^{\beta} \tag{5.6}$$

Triax is the ratio of the hydrostatic stress to the equivalent stress. Hydrostatic stress influences the volume change of a material point which is an elastic process. Equivalent (or von Mises) stress is derived from the deviatoric part of the stress tensor and it affects the shape change of a material point. The relevance of triaxiality to crack initiation is discussed in [141].

$$Triax = \frac{\text{Hydrostatic stress}}{\text{Equivalent stress}} \tag{5.7}$$

ESA and Triax are obtained at the maximum applied strain point corresponding to the fourth cycle, PSA is obtained at the minimum applied strain point at the fourth cycle, and ΔRSS is obtained across the fourth cycle as a difference between the peak and minimum applied strains.

5.4 Results

In a polycrystalline microstructure with pores, the fatigue crack may either initiate at a crystallographic feature (grain boundary, triple/quad points, twin boundary, etc.) or at a pore. The goal of the critical pore study is to identify the scenarios under which the fatigue crack is likely to initiate at the pore rather than the crystallographic features.

Further, in this work, a microstructure with multiple pores will be referred to as a flawed model, a microstructure with no pore will be called a fully dense microstructure. Any micromechanical field quantity (stress, strain, etc.) around a pore in the flawed model depends on the size of the pore, anisotropy of the surrounding grains and the interaction effects (pore-pore and pore-boundary). Mathematically, any micromechanical field (ψ) near a pore could be approximated as:

$$\psi \sim \psi_{\text{avg}} + \Delta\psi_{\text{poresize}} + \Delta\psi_{\text{anisotropy}} + \Delta\psi_{\text{interaction}} \tag{5.8}$$

$\Delta\psi$ represents the perturbation due to the specified factor.

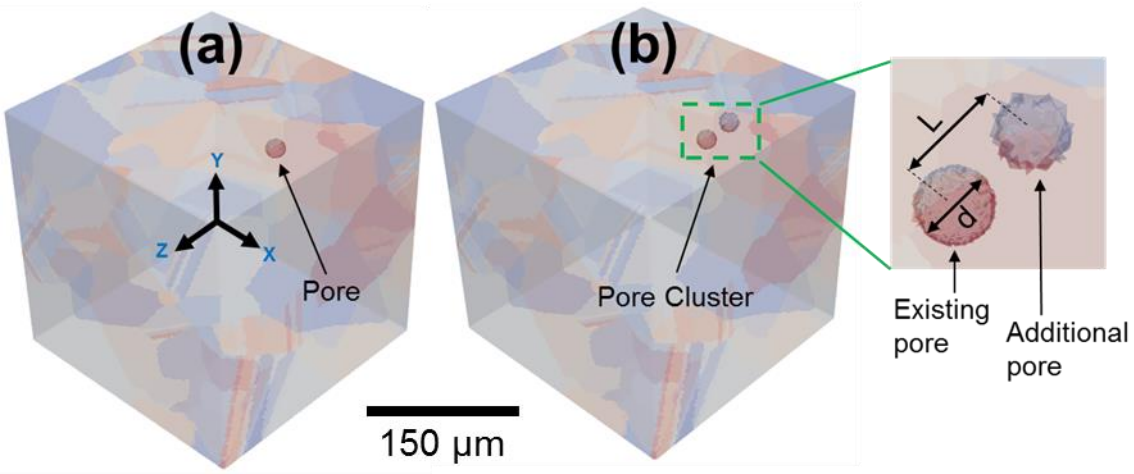

Figure 5.3 Representative microstructure models used in the critical pore study with (a) a single pore and (b) two pores.

The critical pore study is formulated as three connected studies based on Eqn. (5.8), namely, the pore placement study with respect to the SEM, critical size study, and the cluster study. Each study accounts for only one factor. The first two studies have a single pore in the microstructure as shown in Figure 5.3a, and the cluster study has two pores in the microstructure as shown in Figure 5.3b. The pore in the model is created by element deletion from the meshed model. Before deletion, the FE mesh is locally refined at the local neighborhood around the pore center with an element size of 1 μm. The refinement is carried out within a sphere of radius 10 μm greater than the pore radius. This provides a more realistic pore representation and a local refined mesh near the pore to capture gradients in the micromechanical fields. The nearest two layers of elements near the pore are not considered while obtaining the spatial distribution of the DIPs to avoid the effects of the local geometrical serrations caused by element deletion. The descriptions of each study with the mechanistic basis of the formulation and corresponding results are given below.

5.4.1 Pore placement study

In the pore placement study, the FE microstructures are set up in such a way to include only the influence of the surrounding anisotropy ($\Delta\psi_{anisotropy}$). This is accomplished by following three steps. First, the models are created with a single pore, which eliminates the pore-pore interaction effects. Second, the pore is deliberately placed in the bulk of the microstructure, which reduces the

pore-boundary interaction effects, and third, all the models are created with a fixed pore size of 30 μm, which eliminates the effect of the pore size. This study identifies the location in the fully dense microstructure, where a pore should be placed representing the worst-case scenario for a fatigue crack to initiate, as predicted by the DIPs.

It is well known that the intersection points in a fully-dense microstructure (grain boundaries, triple, and quad points) act as stress concentrators. From a study consisting of seven CP-FE simulations, it was found that a pore when placed at the intersection point (of the fully-dense microstructure) possessing the highest stress, resulted in the maximum values of the DIPs (PSA, ΔRSS, and Triax) near the pore. This information regarding the pore placement is used to set up the simulations for the critical size study.

5.4.2 Critical size study

In the critical size study, the influence of the pore size ($\Delta\psi_{poresize}$) is studied by using only a single pore placed at a fixed location (highest stress intersection point corresponding to each SEM), which eliminates the anisotropy and interaction effects. For each SEM, five models are created with one pore in each SEM having sizes of 10, 20, 30, 40, and 50 μm, respectively. This study estimates the critical pore size corresponding to each SEM, which is defined as the size beyond which the location of crack nucleation, as determined by the values of the resulting DIPs, transitions from crystallographic features to the pore vicinity. From the simulations, the critical size is obtained from the radial distribution function of the maximum values of the non-local averaged DIPs. It is estimated by identifying the pore size at which the DIPs near the pore attain the maximum value as compared to the rest of the microstructure.

The radial distribution function of all the DIPs for each SEM are plotted in Figures 5.4-5.8. The fully dense case (with no pore) is plotted in the figures to have a baseline comparison for the SEM models with a pore. The Figures 5.4-5.8 have the same range for each DIP for all SEMs to enable easier visual comparison. It could be observed that the radial distribution of each DIP corresponding to an SEM is distinct and is predominantly due to the variability of the microstructures across the SEMs. For a single SEM, the DIPs near the pore vicinity are different

for each pore size and they converge to the values of the fully-dense case farther from the pore center.

Of all DIPS, both the PSA and ΔRSS have a strong correlation with the pore size as can be seen in Figures 5.4-5.8. In most cases, both the PSA and ΔRSS monotonically increase with an increase in the pore size. In very few cases (as in Figure 5.8), there is a slight decrease of both the PSA and ΔRSS while going from a pore size of 40 to a pore size of 50. This could be attributed to a couple of reasons: a) the immediate neighborhood is different for each pore size or b) local refinement in mesh. On the other hand, both the ESA and Triax do not have a strong correlation with the pore size. The ESA involves gradients, which are numerically calculated during post- processing using the following equation [142]

$$\frac{\partial \phi}{\partial x_r} = \frac{\sum_{m=1}^{n} \frac{1}{r_m} \frac{(\phi_k - \phi_m)}{((x_r)_k - (x_r)_m)}}{\sum_{m=1}^{n} \frac{1}{r_m}} \tag{5.9}$$

$\frac{\partial \phi}{\partial x_r}$ is the partial derivative of a field quantity ϕ with respect to a Cartesian coordinate direction x_r. The partial derivative is evaluated at the k^{th} point using the information of the closest n (=10) neighboring points. r_m is the distance between the k^{th} point and the m^{th} neighboring point. ϕ corresponds to the plastic deformation gradient tensor (F_p) in calculating the ESA. Since ESA involves calculations of gradients explicitly, this quantity is more sensitive to the mesh and serrations near the pore, which would explain the inconsistent behavior of the ESA especially near the pore in Figures 5.4-5.8. As for the behavior of the Triax, it could be attributed to the fact that it is a ratio of two different stress measures. For all the SEMs, the Triax has been observed to be higher at the microstructural features than at the pore vicinity due to the additional volume constraints.

The peak values of all the DIPs, observed particularly near the microstructural features in Figures 5.4-5.8, are not subjected to a detailed investigation to find out the inherent microstructural features, as the focus of this work is more towards the porosity than understanding the microstructural attributes related to fatigue crack initiation.

From the observations above, only the PSA and ΔRSS are considered further in the assessment of the critical pore size. For each SEM, the critical pore size is obtained based on the radial functions of the PSA and ΔRSS. The critical pore size thus obtained for each SEM is plotted in Figure 5.9, and it varies from 20 – 40 μm across all the SEMs. As a conservative estimate the critical pore size could be taken as 20 μm, which is ~ 40 % with respect to the average grain size of 48 μm.

The maximum values of the PSA and ΔRSS at the pore vicinity for all the SEMs with respect to pore size is plotted in Figure 5.10. For the same pore size, there exists a considerable variation of the resulting PSA and ΔRSS. The deviation in the values could be strongly related to the difference in the surrounding microstructure associated with each SEM around the pore. Figure 5.11 shows the visualization of all the DIPs corresponding to SEM4 with a 20 µm pore. Figure 5.11 is mainly intended to depict the heterogeneous deformation behavior of the polycrystalline microstructure and the localization of the micromechanical fields near the pore. Each DIP is plotted with respect to the entire microstructure and about a cross-section across the pore. The PSA, ESA, ΔRSS and Triax are shown in Figure 5.11(a), (b), (c), and (d), respectively.

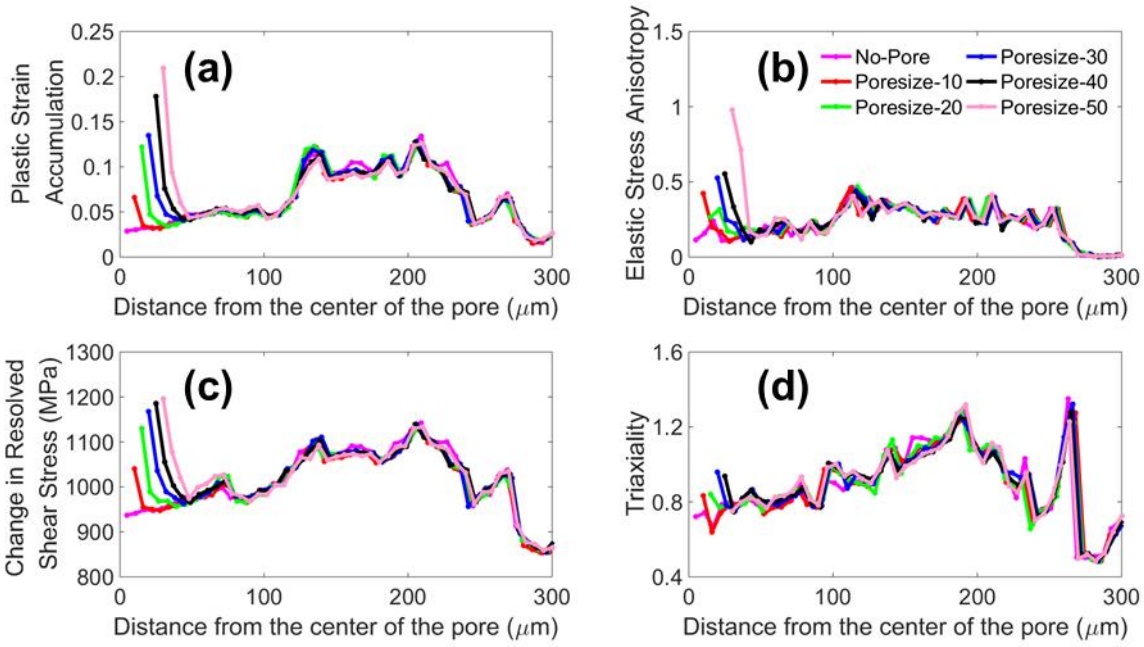

Figure 5.4 Radial distribution plots of the damage indicator parameters for SEM1 (a) Plastic strain accumulation, (b) Elastic stress anisotropy, (c) Change in resolved shear stress, and (d) Triaxiality.

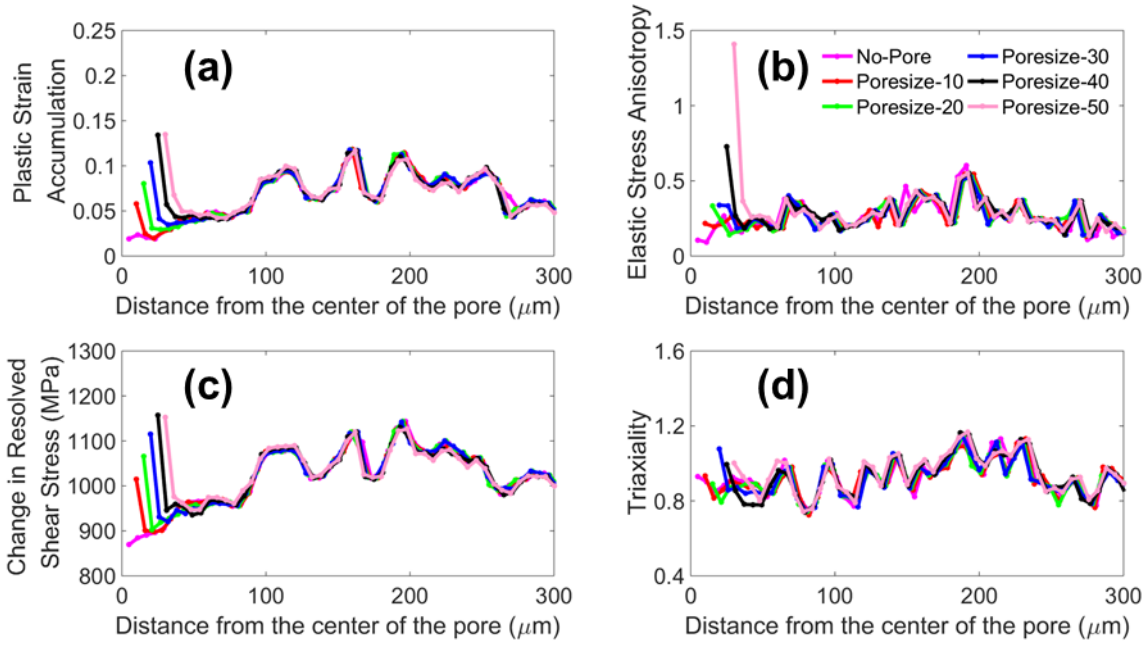

Figure 5.5 Radial distribution plots of the damage indicator parameters for SEM2 (a) Plastic strain accumulation, (b) Elastic stress anisotropy, (c) Change in resolved shear stress, and (d) Triaxiality.

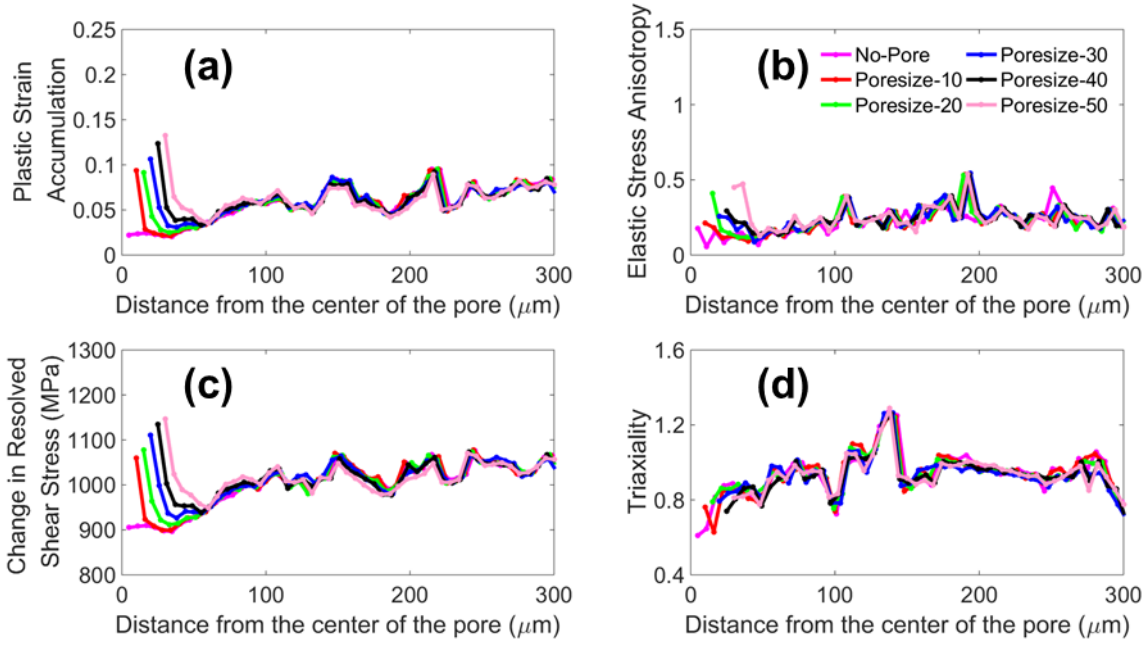

Figure 5.6 Radial distribution plots of the damage indicator parameters for SEM3 (a) Plastic strain accumulation, (b) Elastic stress anisotropy, (c) Change in resolved shear stress, and (d) Triaxiality.

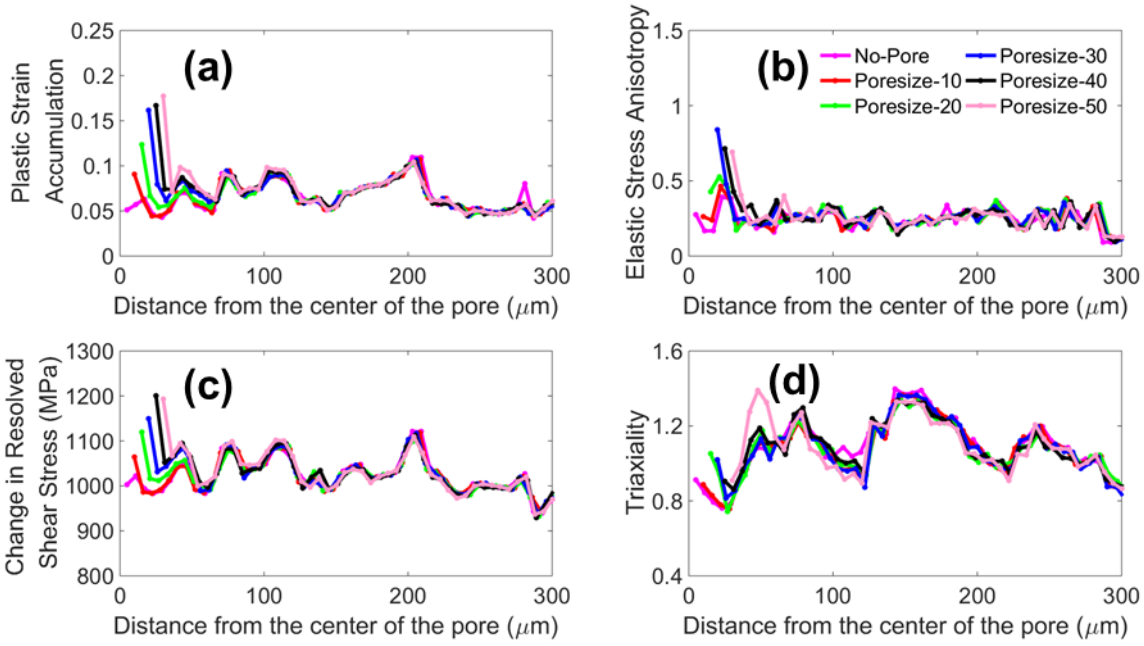

Figure 5.7 Radial distribution plots of the damage indicator parameters for SEM4 (a) Plastic strain accumulation, (b) Elastic stress anisotropy, (c) Change in resolved shear stress, and (d) Triaxiality.

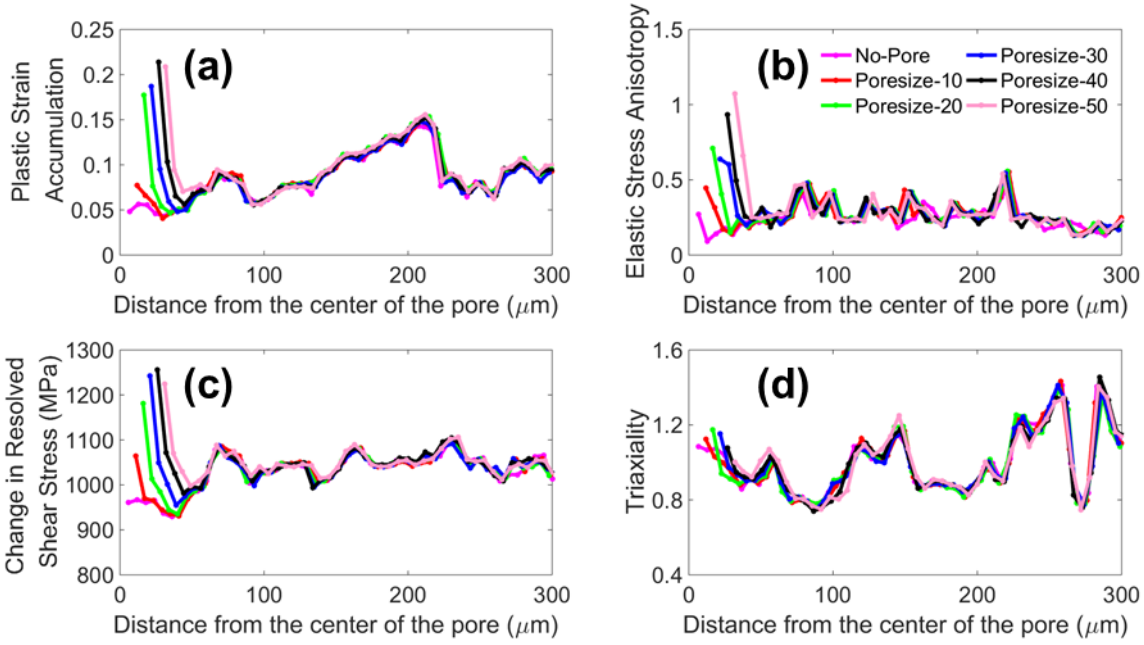

Figure 5.8 Radial distribution plots of the damage indicator parameters for SEM5 (a) Plastic strain accumulation, (b) Elastic stress anisotropy, (c) Change in resolved shear stress, and (d) Triaxiality.

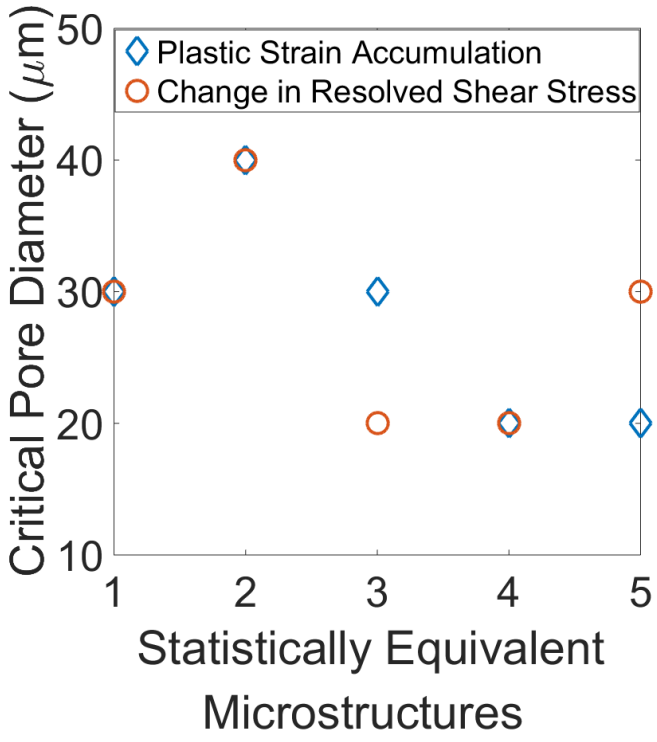

Figure 5.9 Critical pore diameter for each SEM with respect to plastic strain accumulation and change in resolved shear stress.

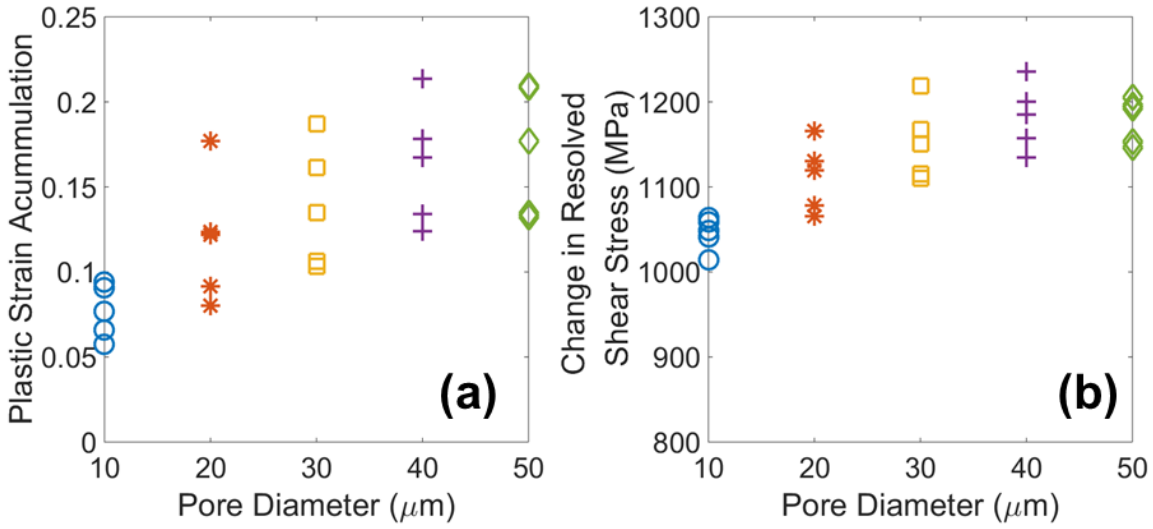

Figure 5.10 (a) Plastic strain accumulation, and (b) Change in resolved shear stress at the pore vicinity as a function of pore diameter for all SEMs.

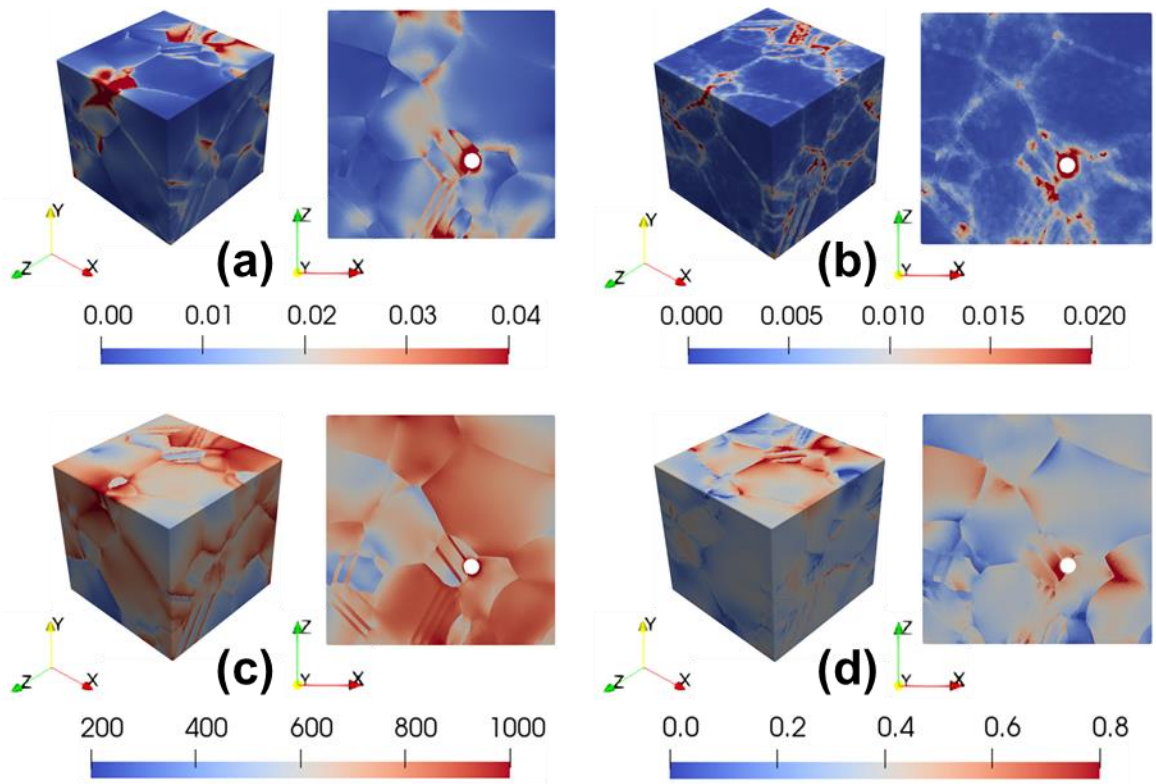

Figure 5.11 Visualization of the damage indicator parameters for SEM4 (with 20 µm pore) along with cross-sectional views near the pore showing the spatial variation of (a) Plastic strain accumulation, (b) Elastic stress anisotropy, (c) Change in resolved shear stress, and (d) Triaxiality.

5.4.3 Cluster study

In the cluster study, the influence of the pore-pore interaction is studied. All the models in this study have two pores (representing a pore cluster) of the same diameter, d, in the microstructure (Figure 5.3b) with their centers separated by a distance of L. The simulations are performed by fixing both the size and location of the existing pore (Figure 5.3b) and the position of the additional pore is varied, thereby varying L in each simulation. The cluster study models (Figure 5.3b) are created using the critical size study microstructures (Figure 5.3a). The additional pore (Figure 5.3b) is created on the plane (X-Z) perpendicular to the loading direction (Y) and radially adjacent to the point in the circumference of the existing pore that has the maximum PSA, which allows for the maximum interaction effects.

From the critical size study, SEM4 has the least critical pore size of 20 μm in terms of both PSA and ΔRSS and hence, it is chosen for the cluster study as it is representative of the worst-case scenario. The first set of cluster models identify the critical separation distance below which a combination of two sub-critical pores (d = 10 μm) is likely to initiate a fatigue crack. This is estimated by comparing the simulation results of the pore cluster study with the results of the critical size study.

Figures 5.12 (a) and (b) display the variation of the PSA and ΔRSS for various L/d ratios. The critical value in Figure 5.12 corresponds to the respective DIP values obtained from the CP-FE simulation of a single 20 μm pore in SEM4 from the critical size study. For the pore cluster of d = 10 μm, the PSA (Figure 5.12 a) exceeds the critical value when L/d equals 1.5, whereas ΔRSS does not exceed the critical value in any case. With respect to PSA, it could be concluded that when the separation distance, L, is less than or equal to 15 μm, a fatigue crack is likely to initiate at the pore cluster.

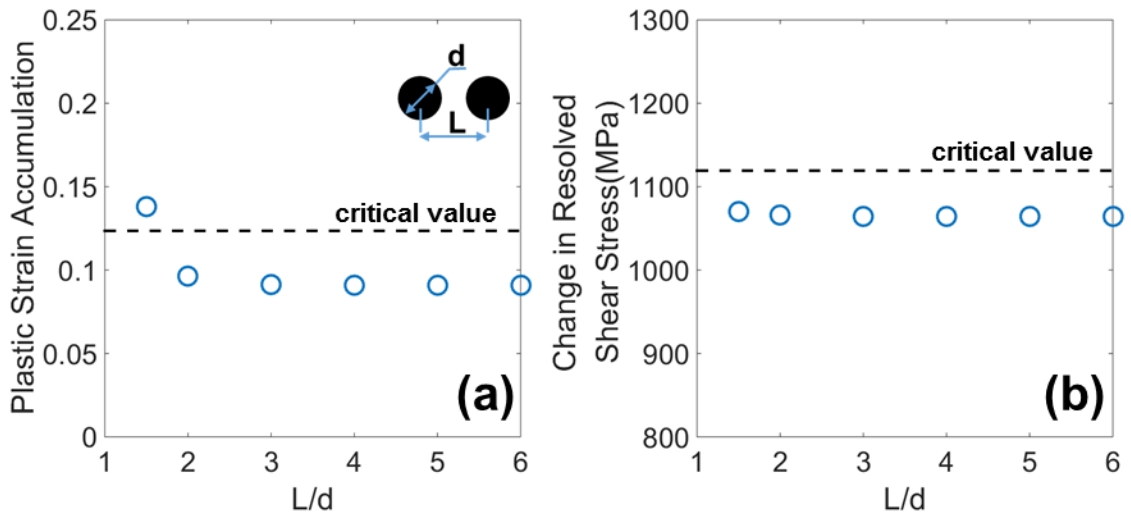

Figure 5.12 Variation of the (a) Plastic strain accumulation and (b) Change in resolved shear stress obtained for the cluster study (d = 10 μm).

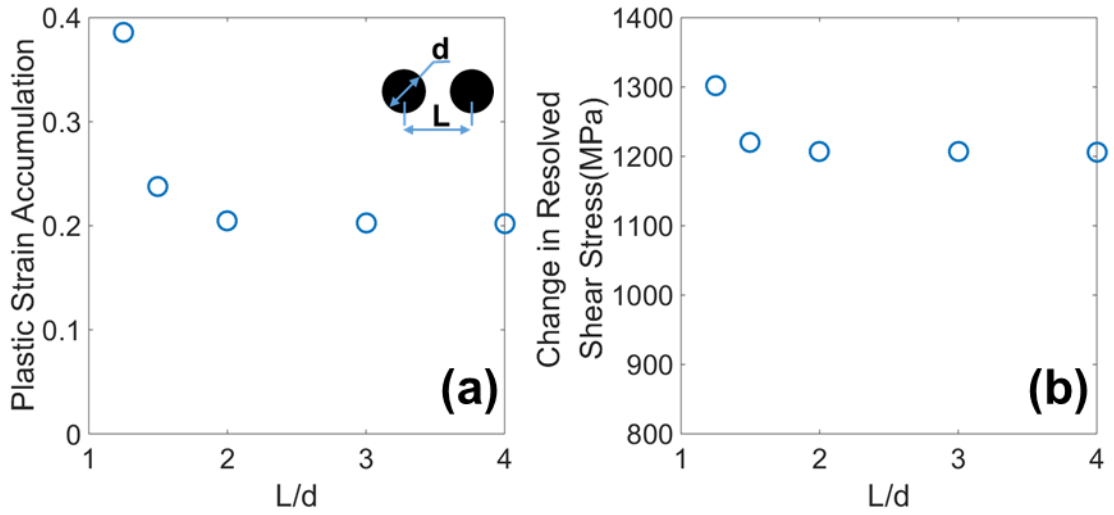

Figure 5.13 Variation of the (a) Plastic strain accumulation and (b) Change in resolved shear stress obtained for the cluster study (d = 20 µm).

The second set of studies are performed with two pores each having a size of 20 μm in order to understand the nature of the pore-pore interaction effects on both the PSA and ΔRSS as a function of L/d. Investigation of Figures 5.12 and 5.13 show that interaction effects are most dominant when L/d ratio is less than or equals 2.

5.5 Discussion

Based on the results of the CP-FE simulations, the size of a critical single pore to cause a potential debit in the fatigue life of SLM IN718 is determined to be 20 μm. From this conservative assessment, a standalone pore of size 20 μm or greater within the microstructure is likely to initiate a fatigue crack. Moreover, additional pores in the vicinity of the initial critical pore would result in a further detriment to the fatigue life. Even sub-critical pores with diameters of 10 μm could cause fatigue failure when the separation distance between them is less than 15 μm, due to the pore-to-pore interaction. The results of the CP-FE simulations are compared with the µXSCT characterization (Figure 3.3) to identify the probability of limiting porosity within representative SLM IN718 material. From Figure 3.3, the probability of a single pore greater than 20 μm in size is 0.2%, while the probability of pores possessing a diameter of 10 to 20 μm is equal to 1.8%. In general, the probability of pores being spaced less than 15 μm apart is 41.6%. From the probability values determined from the µXSCT characterization, based on their size and separation distance,

~1% pores are likely to providing a fatigue debit. For this SLM IN718 material, a tomography measurement with resolution of 10 μm (5 μm voxel size based on Nyquist sampling) would be sufficient for detection of critical porosity within the material. In addition, the process build parameters and subsequent post-processing treatments could be tailored to control the porosity within the critical limits as obtained from the simulation results.

The final mode of failure from a pore is due to the pore-boundary interaction. Although the pore-boundary interactions are not explicitly modeled, it is possible to obtain a rough estimate from the results of the porosity cluster study. Based on symmetry, we propose the approximation as shown in Figure 5.14. A pore cluster separated by a distance, L, is idealized into a pore-boundary configuration with a separation of L/2. Of course, the traction free-boundary conditions of the free surface and the resulting surface deformation would result in a breakdown of this simplifying assumption. Nevertheless, the imposed symmetry condition would be more detrimental to the values of the DIPs than the free surface, as the additional out-of-plane constraints from the symmetry condition would result in additional localization of the micromechanical fields compared to the free surface condition. Hence, the symmetry assumption depicted in Figure 5.14 provides a conservative estimate. From the cluster study, it was determined that a pore cluster, in which pores are separated by less than 15 μm would provide a debit in the fatigue life and the pore-to-pore interaction would be dominant when the L/d ratio is less than 2. Based on these results, a surface connected pore or pore immediately sub-surface by a distance equivalent to its diameter would result in localization of the micromechanical fields and likely be a site for fatigue crack initiation.

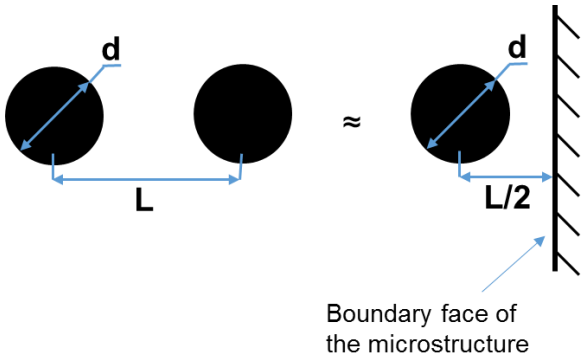

Figure 5.14 Approximating pore-pore interaction to an equivalent pore-boundary interaction.

The CP-FE simulations in this study represent an idealized microstructure, which does not introduce residual stresses, non-metallic inclusions [143], surface roughness, as large as (ALA) grain sizes [4], or notches due to geometric discontinuities, which would further reduce the fatigue life and act as a competing failure mechanism in the presence of porosity. Residual stresses have a less significant effect on crack initiation, as post-processing heat treatment significantly reduces them [7]. Surface defects, including surface roughness and surface connected porosity, are another prominent source of crack initiation in SLM materials [21,144,145]. Any surface defect could be modeled as an equivalent sized surface pore [31,34] using the current framework. Thus, by including more representative defects within the simulation, it is anticipated that the critical pore size would increase, as pore induced crack initiation would serve as a competing mechanism with other flaw-mediated sources of failure. Thus, the current study represents a conservative approach (or worst-case scenario) for the critical pore size. As the first attempt at validation, the SLM IN718 material was machined into eight micro-fatigue specimens with gauge volume of 1 mm^3. This material, corresponding to the porosity characterization in Figure 3.3, was cyclically loaded until failure. Fractography was conducted on the failed fracture surfaces, and in each specimen, porosity was not the cause of failure. Hence, based on the porosity characterization for this material, it was determined from the present modeling analysis that ~ 1% of the pores in the characterization volume are potentially likely to initiate a fatigue crack, albeit this low percentage was in agreement with the experiments, since pore initiated failure was not observed from the fractography analysis. This is the topic of on-going research aimed at predicting the fatigue lifetime of SLM IN718 material.

5.6 Conclusions

- A crystal plasticity based modeling framework is developed to quantify the critical scenarios of porosity towards the fatigue crack initiation of SLM IN718, where,

    - Statistical equivalent microstructures are created as input to crystal plasticity simulations, which are statistically representative of the microstructural attributes and macroscopic stress response.
    - Crystal plasticity parameter estimation is posed as an optimization problem and is solved using a genetic algorithm.
    - A spatial non-local averaging technique is introduced to capture the variations of the micromechanical fields, which allows the usage of a coarser mesh.
    - The problem of critical porosity study is formulated as three connected studies based on the mechanics of pore deformation, which are the pore placement relative to the neighboring microstructure, critical size of a single pore, and the separation distance of two pores representing a pore cluster.

- For the SLM IN718 materials with average grain size of 48 μm, the size of a critical single pore to cause fatigue failure is obtained as 20 μm. It was also found that even sub-critical pores of 10 μm in diameter could cause fatigue failure when the separation distance between these pores is less than 15 μm, due to the pore-to-pore interaction. Based on a statistical argument, the percentage of critical porosity within the μXSCT characterization volume is estimated as ~ 1%.

- The modeling framework developed in this study has been used to study critical porosity but can be extended to other defects. This work is potentially beneficial in qualifying SLM materials given the natural porosity inherent to the manufacturing process, by reducing the number of necessary fatigue experiments. Additionally, the results of this study can be used to help identify appropriate process build parameters based on the resulting porosity, choice of non-destructive evaluation methods based on the resolution needed to capture the critical pore size, and subsequent post-processing steps necessary to mitigate pores larger than the critical size.

6. EXAMINING METRICS FOR FATIGUE LIFE PREDICTIONS INCLUDING THE ROLE OF SIMULATION VOLUME AND MICROSTRUCTURAL CONSTRAINTS

In this chapter, a comparative assessment of multiple fatigue metrics based on microstructure-sensitive CPFE simulations of many virtual microstructures are performed, to obtain the probable location of failure and the scatter in fatigue life, considering the failures at both the surface and sub-surface, including the role of porosity. In addition, we perform additional sets of CPFE simulations to understand the role of simulation volume as well as the boundary conditions on the prediction of the fatigue scatter. Within this chapter, Section 6.1 describes the crystal plasticity based fatigue modeling framework, Section 6.2 presents the results, and Sections 6.3 and 6.4 provide the discussions and conclusions of this work, respectively. The results and analysis provided in this chapter have been published in [146].

6.1 Fatigue life prediction framework

6.1.1 Microstructural models

Fifteen SEMs are created for this study, as shown in Figure 6.1. The pores are created randomly within the SEMs such that the volume fraction of the pores across the SEMs matches the volume fraction from µXSCT characterization. Also, the sizes of the pores are sampled from the tails of the distribution obtained from the µXSCT characterization [66] and are prescribed to be 10, 20, 30, and 40 µm. The pores are inserted to serve as a competing failure mechanism. As per the previous studies by the authors [66,107], a pore becomes significant only if its size is equal or greater than 10 µm and hence, is chosen to be the minimum size. The details of the number of pores and corresponding sizes in each SEM have been shown in Table 3.1. The creation of pores in the discretized SEMs is performed via element deletion. Before deletion, the local neighborhood around each pore is refined using an element size of 1 µm. The radius of the sphere of refinement is 10 µm greater than the actual pore radius. The refinement helps in obtaining a near-spherical pore morphology and preserves the gradients developed near the pore. Constraints are added such that each SEM can have a maximum of two pores, which permits more uniform distribution of the pores across the SEMs, and the intersection of pores during the creation process is prevented.

Each SEM is a cube of dimension 300 μm. The number of grains within the SEMs varies from 190-204. Linear tetrahedron elements (C3D4) are used in meshing. The global mesh size for each SEM is prescribed as 3 μm based on a sensitivity study reported in Ref. [66]. The number of nodes across the SEMs range from 0.74 to 1 million and the number of elements span from 4.5 to 6.2 million.

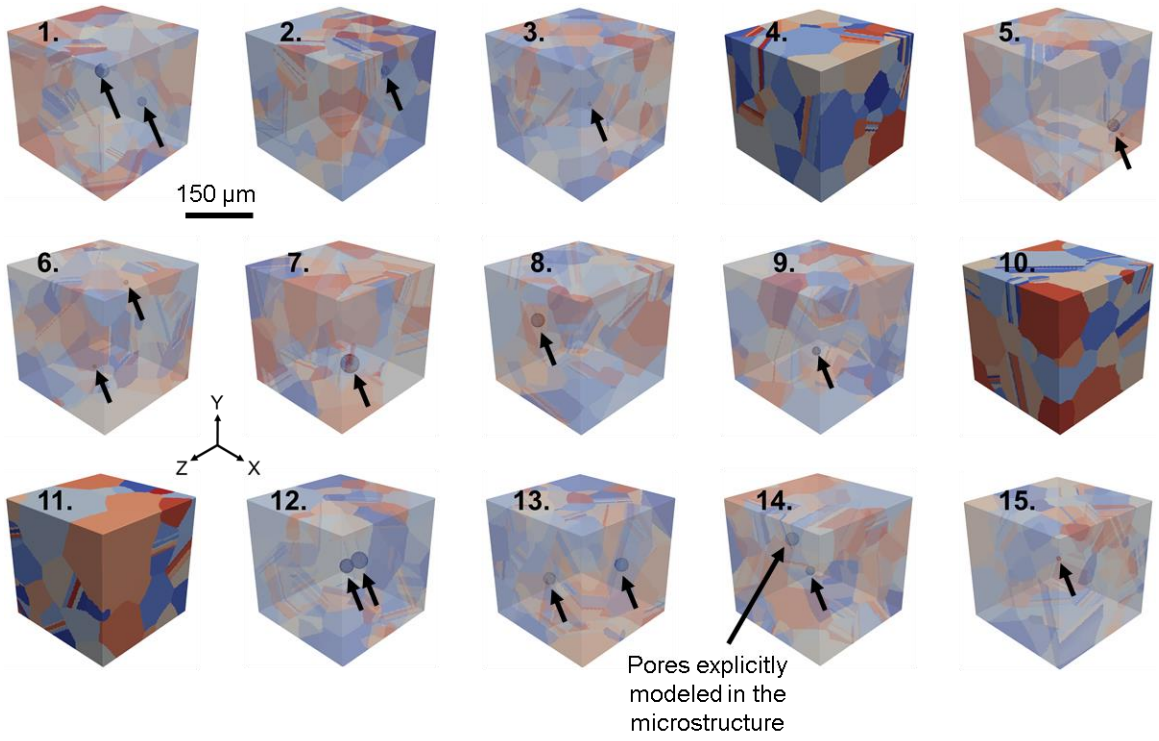

Figure 6.1 Fifteen statistically equivalent microstructures (SEMs) used as input to the crystal plasticity simulations and subsequently the fatigue life predictions are shown. Twelve SEMs (shown with a transparent view) contain pores indicated via black arrows and the other three (opaque view) are fully dense. It should be noted that the two pores in SEM # 12 are not close to each other. Microstructures are colored by unique grain IDs. The pore size details for each SEM are shown in Table 3.1.

Table 6.1 The number of pores and the corresponding pore diameter for each SEM (shown in Figure 6.1) are indicated. The number of pores in each SEM vary from 0 to 2 and the pore diameter varies from 10 to 40 μm.

SEM#	No. of pores	Pore diameter (μm)	
1	2	20	30
2	1	20	-
3	1	10	-
4	0	-	-
5	2	30	10
6	2	10	10
7	1	40	-
8	1	30	-
9	1	20	-
10	0	-	-
11	0	-	-
12	2	40	30
13	2	30	30
14	2	20	30
15	1	10	-

6.1.2 Boundary conditions

Each SEM model is subjected to a stress-controlled cyclic loading with R_σ =0.01 and σ_{max} = 800 MPa for ten loading cycles until the saturation of the local plastic strain response. The loading conditions are the same as that of the experimental fatigue testing. The average time to completion for a CPFE simulation is about five days, while running on 160 processors in parallel. The boundary conditions used in the CPFE simulations are shown in Figure 6.2. Normal displacements

on the three adjacent orthogonal faces (as defined by X=0, Y=0, and Z=0) are constrained. Normal stress is specified on the top face (Y=300 µm) of the microstructure. The other two faces of the microstructure (X=300 µm, Z=300 µm) are free from any constraints. In this work, the failure modes due to crystallographic features and pores are primarily considered. The role of residual stresses was not considered in the modeling activity since the samples underwent rigorous post-processing resulting in significantly lower residual stress values as compared to macroscopic loading conditions [86], moreover we could potentially expect relaxation of the initial residual stresses with cyclic loading especially at non-zero mean stress (R_σ =0) loading conditions [147]. Furthermore, the effect of surface roughness was not considered since the test coupons were ground and polished [86].

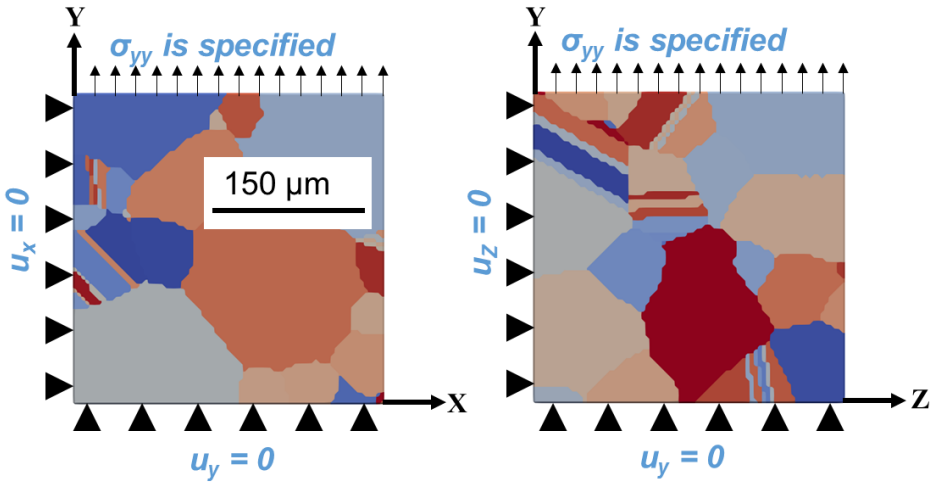

Figure 6.2 Finite element boundary conditions applied on the faces of the microstructure model used in the CPFE simulations. u_x is zero on the X=0 face, u_y is zero on the Y=0 face, u_z is zero on the Z=0 face, σ_{yy} is specified on the top face (Y=300 µm), and the other two faces (X or Z=300 µm) are unconstrained.

6.1.3 Fatigue metrics for location and life prediction

In this work, the fatigue metrics are used to obtain the likely location of fatigue crack initiation and to predict the fatigue life. The metrics are chosen to be positive and monotonically increasing with the number of loading cycles, to enable fatigue life prediction. The choice of metrics was based on previous studies in literature, including Morrow [46], Fatemi and Socie [48], McDowell and co-workers [56–61], Dunne and colleagues [65,68], and Bandyopadhyay et al. [148]. All of the aforementioned studies have emphasized the importance of both plastic strain and local stresses

in predicting the crack initiation events. Hence, in this work, we assess the fatigue life using different metrics, most of which are formulated as a composite measure of plastic strain and local stresses. Six candidate metrics have been formulated. To have a baseline comparison, one metric is defined purely in terms of plastic strain, and the rest of the five metrics are a combination of plastic strain and a measure of the local stress state.

The first metric is the plastic strain accumulation (PSA), which indicates the cumulative slip calculated at an integration point due to the shear across all the individual slip systems [137,138]. Slip localization is well-known to be a precursor to crack initiation [39,139], and experimental evidence suggests that PSA could potentially capture the location of crack initiation [64,65,68]. PSA is obtained as the integral of the double dot product of the plastic velocity gradient, $\mathbf{L_p}$,

$$\textbf{M1:} \quad \text{PSA} = \int \sqrt{\frac{2}{3}\mathbf{L_p}:\mathbf{L_p}}\, dt \tag{6.1}$$

The second metric is the cumulative plastic strain energy density (W^p), which corresponds to the dissipative energy due to plastic deformation. The relevance of the dissipative energy to fatigue crack initiation has been shown in the works of Skelton [149] and Korsunsky et al. [150].

$$\textbf{M2:} \quad W^p = \oint \sigma : \boldsymbol{L_p}\, dt \tag{6.2}$$

Where $\boldsymbol{\sigma}$ is the Cauchy stress tensor. The W^p has accounted for the local stress in an implicit manner. Since the Cauchy stress is a continuum level parameter, we consider the slip level stress measures, namely, the maximum resolved shear stress (τ_{max}) and a Dang Van type measure ($\tau_{max} + \sigma_h$) [151] to formulate the next four fatigue metrics. τ_{max} provides a measure of the maximum shear stress at an integration point, out of the twelve slip systems.

$$\tau_{max} = \max_{\alpha}[\boldsymbol{\sigma}:(\mathbf{s}^{\alpha} \otimes \mathbf{n}^{\alpha})] \tag{6.3}$$

The hydrostatic stress, σ_h, influences the volume change at a material point and a tensile hydrostatic stress is known to be conducive to crack formation and growth [151][152].

$$\sigma_h = \frac{\text{trace}\,(\boldsymbol{\sigma})}{3} \tag{6.4}$$

Taking inspiration from the classical multi-axial fatigue approaches [151,153], simple combinations, namely the product and sum forms, are used. The third and fourth fatigue metrics are obtained using the product of stress measures and PSA, as given by:

$$\textbf{M3:} \quad \text{PSA} * (\tau_{\max} + \sigma_h) \tag{6.5}$$

$$\textbf{M4:} \quad \text{PSA} * \tau_{\max} \tag{6.6}$$

The fifth and sixth fatigue metrics are obtained by a linear combination of stresses and PSA. Since, PSA and stresses have different units; they are first normalized and then added. The fifth and sixth metrics are given by:

$$\textbf{M5:} \quad \frac{\text{PSA}}{\langle \text{PSA} \rangle} + \frac{\tau_{\max}}{\langle \tau_{\max} \rangle} \tag{6.7}$$

$$\textbf{M6:} \quad \frac{\text{PSA}}{\langle \text{PSA} \rangle} + \frac{\tau_{\max} + \sigma_h}{\langle \tau_{\max} + \sigma_h \rangle} \tag{6.8}$$

Where $\langle . \rangle$ denotes the maximum value of the given field quantity among all the integration points within a given SEM at the last cycle analyzed. These six metrics will be used subsequently to identify the location of failure within an SEM and predict the fatigue life of each SEM.

6.1.4 Fatigue model calibration and prediction

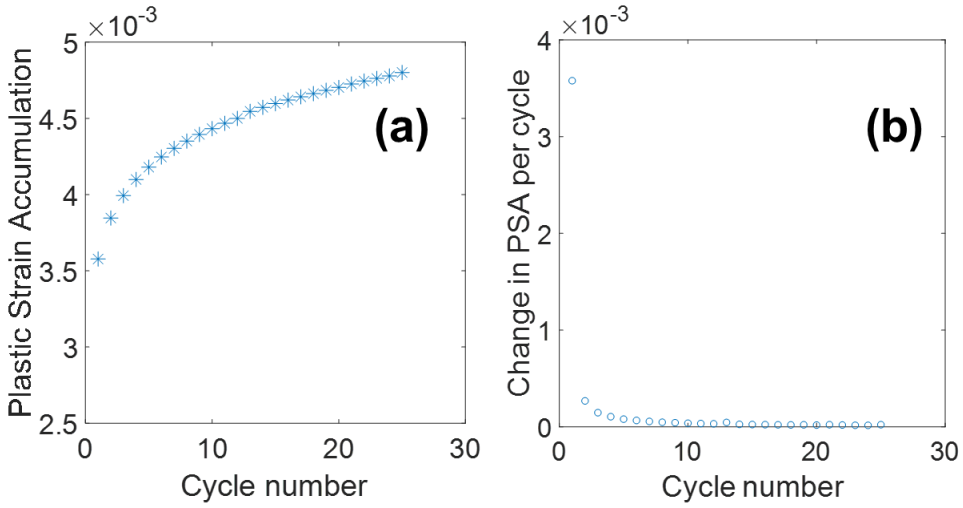

Figure 6.3 (a) Evolution of the plastic strain accumulation with fatigue loading cycles at an integration point, (b) Change in plastic strain accumulation per cycle indicating local plastic shake down at approximately ten cycles.

The evolution of the non-local averaged PSA, and the change in PSA per cycle until 25 loading cycles are shown in Figures 6.3(a) and 6.3(b), respectively. From Figure 6.3(b), we observe that the local plastic strain saturates after ten cycles, which means that there will be constant increments of plastic strain after cycle ten. Similar behavior was observed for the other metrics as well. Based upon the above observation, the value of any fatigue metric, after cycle ten, can be obtained from linear extrapolation. Let ϕ_i^j be the fatigue metric for the ith microstructure, for a given approach (j refers to the combination of the particular fatigue metric (M1-M6) and averaging scheme). The value of ϕ_i^j at N cycles (N >>10) is obtained as:

$$(\phi_i^j)\big|_N = (\phi_i^j)\big|_{10} + (\Delta\phi_i^j)\big|_{10} * N \tag{6.9}$$

where, $(\Delta\phi_i^j)\big|_{10}$ is the increment in ϕ_i^j from cycle nine to cycle ten.

Due to the inherent stochasticity of fatigue, life predictions require a non-deterministic approach. Here, a series of i microstructures are randomly generated (yet their distributions of microstructural attributes are statistically similar). The microstructure generation results in different neighboring

grains in each SEM, thus adding a non-deterministic approach to lifetime prediction [4,5]. After ten cycles of loading is applied to each SEM, through the CPFE simulation described in Section 3.2, the predicted location of the failure (or the hotspot) for a given SEM is identified as the element ID (upon applying the regularization scheme) with the maximum value of the fatigue metric of interest. Following hotspot identification, the fatigue prognosis of the set of the i SEMs is performed as a two-step process: (i) calibration and (ii) life prediction. The calibration involves estimating the critical value of a particular fatigue metric ϕ^j across the distribution of SEMs analyzed. Such a critical value is unique to a specific combination of the fatigue metric and regularizing scheme, and is obtained as follows. The set of the ϕ_i^j form a distribution for the evolution of the fatigue metric with increasing cycle numbers, *N*, using Eqn. (6.9). The distribution of extrapolated ϕ_i^j (for i = 1 to 15 SEMs) is obtained as a series of linear equations. The median value of this distribution is set equal to the experimentally obtained median fatigue life, and used to identify the critical value of the fatigue metric ϕ^j. With input from the calibration, the fatigue life of the ith SEM (N_{SEM}) for a given ϕ^j is predicted using a rearranged form of Eqn. (6.9), given as:

$$N_{SEM} = \frac{(\phi_i^j)\big|_{critical} - (\phi_i^j)\big|_{10}}{(\Delta\phi_i^j)\big|_{10}} \tag{6.10}$$

6.2 Results

The hotspots predicted by the non-local averaged, band averaged, and grain averaged values of PSA (**M1**) are shown as white circles in the bottom row of Figure 6.4. The hotspot predicted by the non-local averaged value of the PSA is near a pore, while both the band- and grain-averaged values of PSA predict different hotspot locations. The non-local averaged PSA is able to capture the localized effect near the pore as is expected due to the geometrical stress concentration, whereas both the band- and grain- averaged PSA are unable to capture this behavior since both the schemes homogenize the PSA over larger volumes, which makes the localization behavior diminish. The grains corresponding to each hotspot are highlighted in green on the top row of Figure 6.4 and are different for each averaging scheme. In each SEM, there is a distribution of the grain sizes. The size of the averaging volume for the band- and the grain- averaging schemes are

dependent on the size of the grain. Therefore, there is a significant variation in the number of elements inside the averaging volumes (especially for the band- or grain- averaging schemes) depending on the spatial location of the integration point, which possibly results in non-realistic hotspot predictions. Furthermore, both the band- and grain- averaged values do not provide any insight into the different modes of failure. Hence, for the above reasons, the non-local averaging is considered as the appropriate scheme and is used in further analysis.

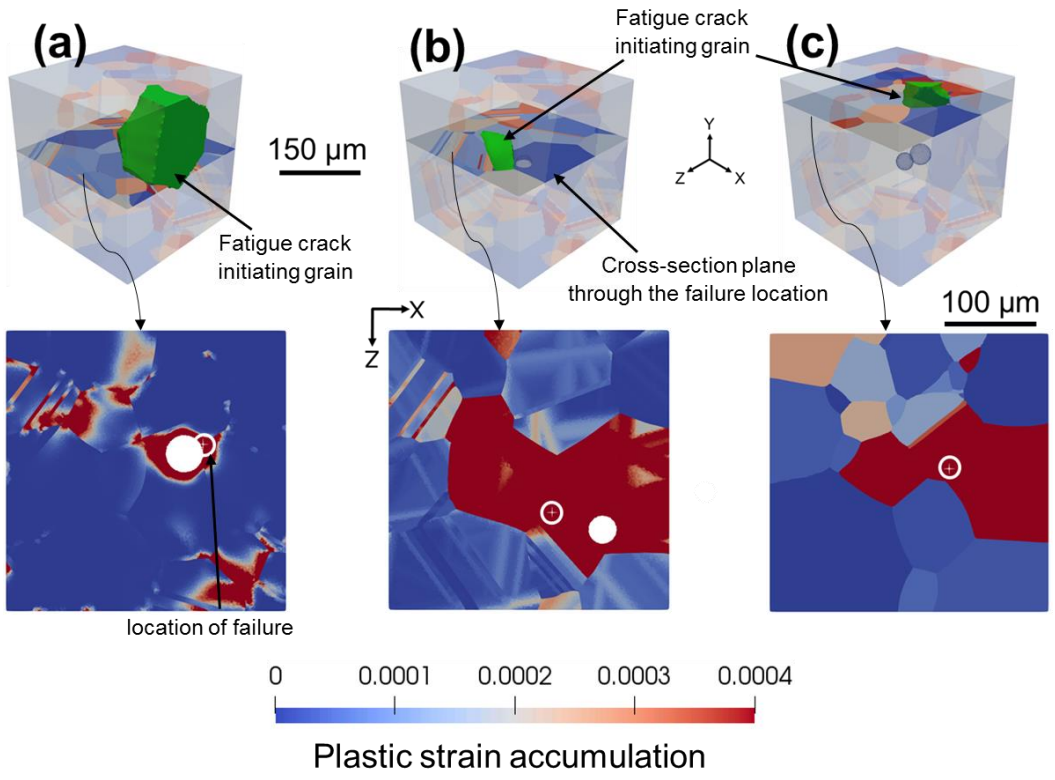

Figure 6.4 The top row shows the fatigue crack initiating grains (highlighted in green) and the corresponding X-Z cross-section through the failure location, and the bottom row shows the physical location of failure on the X-Z plane as predicted by the: (a) non-local averaged values, (b) band-averaged values, and (c) grain-averaged values of plastic strain accumulation (**M1**).

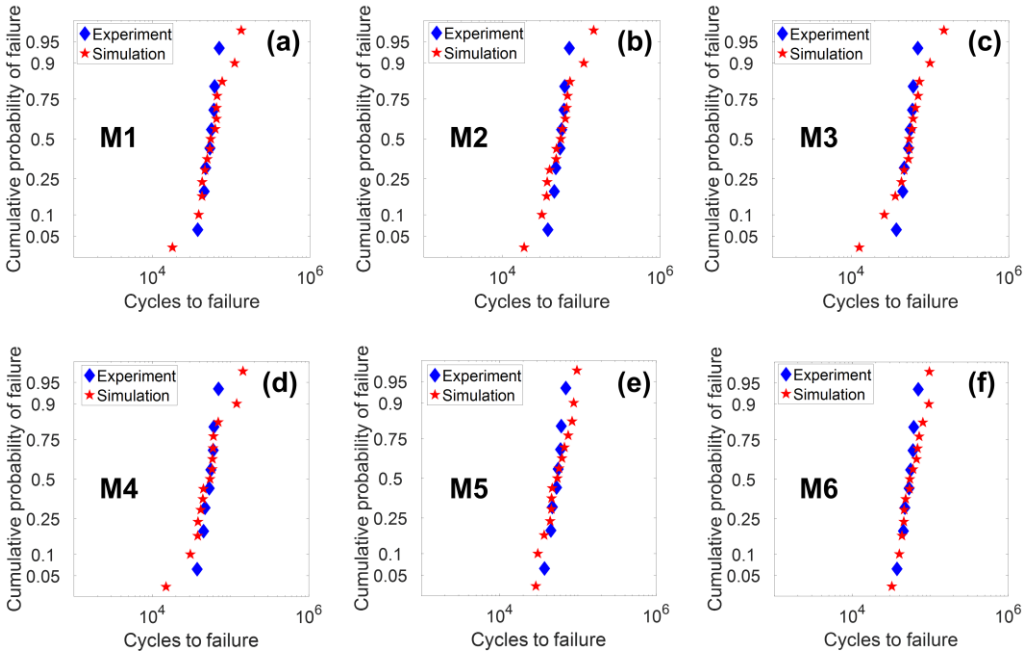

Figure 6.5 Fatigue life predictions of IN718 using the non-local averaged values of the metrics (a) **M1**, (b) **M2**, (c) **M3**, (d) **M4**, (e) **M5**, and (f) **M6.**

.

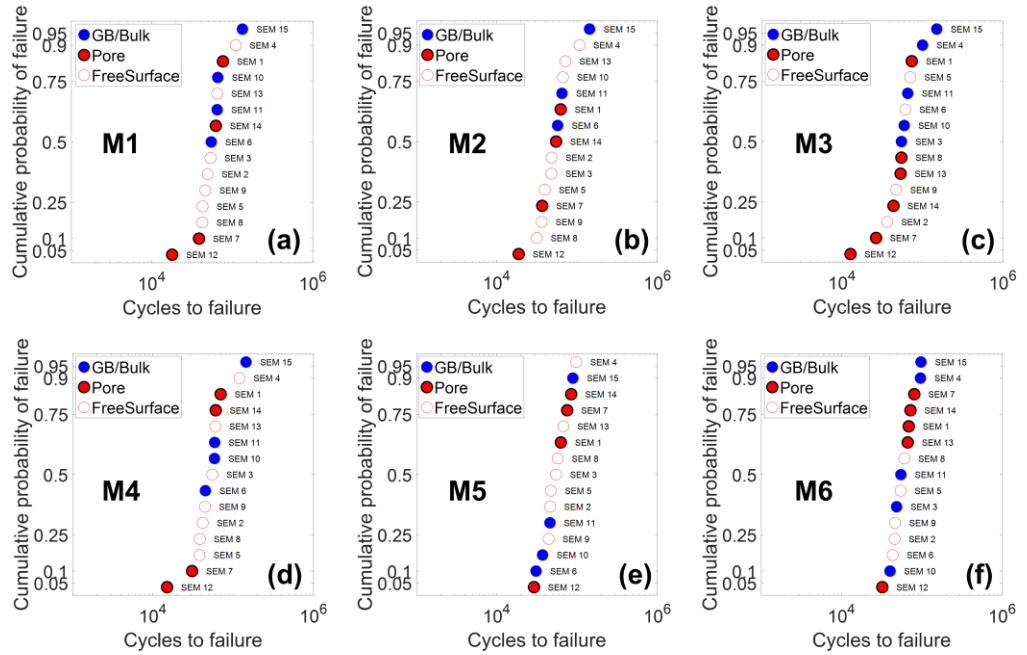

Figure 6.6 Different modes of failure (including the failure at a pore, free surface, and near a grain/twin boundary in the bulk) along with the SEM IDs overlaid on the fatigue life plot obtained using non-local averaged values of the metrics (a) **M1**, (b) **M2**, (c) **M3**, (d) **M4**, (e) **M5**, and (f) **M6.**

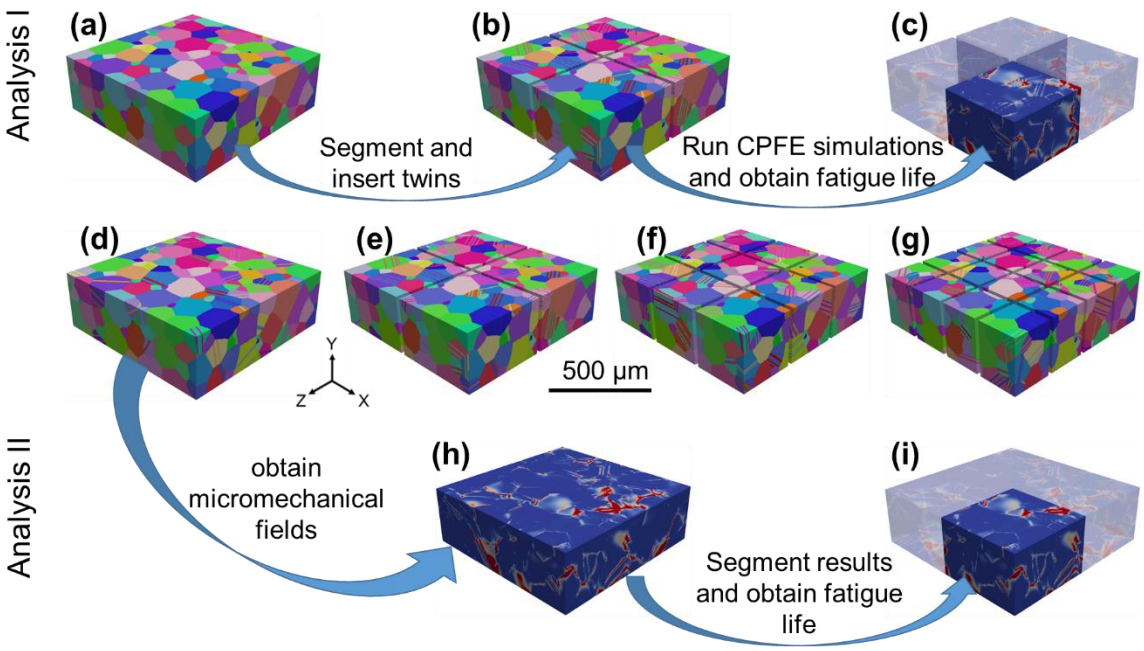

Figure 6.7 Two additional analyses are performed to understand the role of the simulation volume and the boundary conditions on the fatigue life estimation. In the first analysis, 30 microstructures having four distinct volumes are created and utilized to perform CPFE simulations and, subsequently, the fatigue life predictions. One large model (d) is obtained by inserting twins into the parent microstructure (a) and the remaining 29 microstructures, as shown in ((e)-(g)), are obtained by first segmenting the parent microstructure (a) equally in divisions of four, nine, and sixteen, respectively, and inserting twins in each resulting volume segment. Traction-free BCs (as in Figure 6.2) is used in each of the 30 simulations. In analysis II, no additional CPFE simulations are performed. The micromechanical fields (h) from the CPFE simulation of the model (d) are segmented equally in divisions of four, nine, and sixteen to obtain 29 sub-volumes and fatigue life estimation is performed for each sub-volume. Each sub-volume will have unique microstructural constraints (or BCs) based on the location of the sub-domain in the model (d).

The fatigue scatter predictions using the non-local averaged values of the six fatigue metrics are shown in Figure 6.5. The fatigue lives were calculated using the method described in Section 3.5. The fatigue lives from the experiments are within the ranges of lives calculated from the six metrics from the CPFE simulations indicating that all of the six metrics perform reasonably well in capturing the range of the fatigue life. Moreover, the slope of the lognormal distribution (i.e. the scatter) is well captured by all of the metrics, albeit there are differences at the extreme values of the distribution.

The modes of failure (corresponding to each point in Figure 6.5) are shown in Figure 6.6. A mode of failure is identified and labeled as per the spatial location of the predicted hotspot for each SEM. There are three different modes of failure, labeled as (a) GB/bulk, indicating that the hotspot is in

the subsurface and in the vicinity of a grain/twin boundary, or a triple/quad junction, (b) pore, depicting that the hotspot is near a pore, and (c) free surface, representing that the hotspot element is touching any of the free surfaces (namely, X=300 μm or Z=300 μm) in an SEM. Alongside the failure mode, the corresponding SEM is also shown in Figure 6.6.

The predictions of scatter in fatigue lives, thus far, were performed using a simulation volume of 300*300*300 μm^3, which is lesser than the actual volume of the gauge section of the sample (1000*300*1000 μm^3) used in fatigue testing. With the increase in the simulation volume, the number of grains inside the microstructure would increase, which can potentially alter the maximum values of the fatigue metrics due to the grain interactions and in turn, the fatigue lives. Second, traction-free boundary conditions (as discussed in Section 3.2), were used for every SEM to calculate the scatter in fatigue lives (Figure 6.5). Hence, it is important to critically assess the effect of both the simulation volume and boundary constraints on the life predictions. To this end, two additional sets of analyses were performed.

The first analysis is designed to understand the effect of the simulation volume on the fatigue life predictions. In the first analysis, CPFE simulations and fatigue life estimation of 30 different microstructures (Figure 6.7(d)-(g)) having four distinct simulation volumes (the largest microstructure (Figure 6.7(d)) has a volume close to the gauge volume of the test specimen) were carried out with the traction-free BCs, as in Figure 6.2. All the 30 microstructures (Figure 6.7(d)-(g)) were created from a single parent microstructure (Figure 6.7(a)), which consists of no twins and has a dimension of 900*300*900 μm^3. The first microstructure (Figure 6.7(d)) is created by inserting twins into the parent microstructure. The remaining 29 models are obtained by segmenting the parent microstructure equally in divisions of four (Figure 6.7(e)), nine (Figure 6.7(f)), and sixteen (Figure 6.7(g)), respectively, and inserting twins in each of the segments independently. The creation process mentioned above associates each of the 30 microstructures to the parent microstructure, analogous to sampling smaller populations of the microstructure. The dimensions of each model in Figure 6.7 (e), (f), and (g) is 450*300*450 μm^3, 300*300*300 μm^3, 225*300*225 μm^3, respectively. The number of grains in model (d) is 1423, and the number of grains varies from 313-559 in model (e), 147-265 in model (f), and 84-160 in model (g). All the 30 models thus created are statistically representative in terms of microstructural attributes while

the microstructures in Figure 6.7(g) do not necessarily possess equivalent strength characteristics, therefore, are not considered SEMs.

The second analysis is set-up to investigate the role of the microstructural constraints on the life estimation. In this analysis, while no additional simulations were carried out, the micromechanical fields (Figure 6.7(h)) obtained from the CPFE simulation of the largest model (Figure 6.7(d)) are utilized to perform life calculations. In this work, a sub-volume (Figure 6.7(i)) is defined as a sub-set of the meshed model mapped with the micromechanical fields (Figure 6.7(h)). Multiple sub-volumes having three distinct volumes are sampled and fatigue life for each sub-volume is estimated. Such sampling will capture the realistic microstructure constraints associated with the sub-volumes and its effect on the resulting fatigue life. The micromechanical fields (Figure 6.7(h)) are segmented equally in divisions of four, nine, and sixteen, to obtain 29 sub-volumes of dimensions 450*300*450 μm^3, 300*300*300 μm^3, and 225*300*225 μm^3, respectively. The process in the first analysis is shown in the first row of Figure 6.7, while the second analysis is depicted in the last row of Figure 6.7.

The fatigue lives for both the analyses are obtained using the non-local averaged PSA (**M1**) and are shown in Figure 6.8 and Figure 6.9, respectively. The critical value of PSA (as per Eqn. (6.9)) is estimated using the microstructure in Figure 6.7(d). Moreover, a lognormal reference line is plotted for identically sized microstructures and sub-volumes in Figure 6.8 and Figure 6.9. Furthermore, the fatigue lives at a probability of 0.001 is obtained for both analyses via extrapolation and is shown in the table in the inset of Figure 6.8 and Figure 6.9. In these analyses, we are more interested in the slope of the lognormal distribution (i.e. the scatter) as a function of simulation volumes. From Figure 6.6, it could be seen that the pores do alter the minimum fatigue life but do not significantly change the slope of the distribution. For this reason, for the above two size analyses, pores were not inserted in the microstructures.

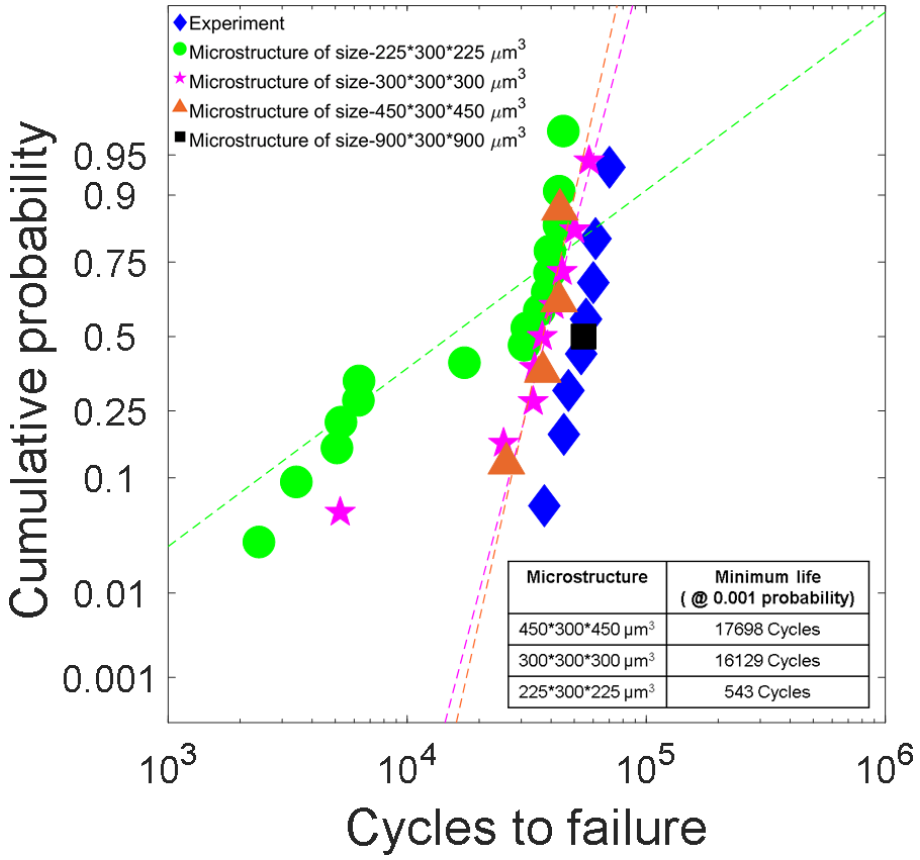

Figure 6.8 Fatigue life prediction using non-local averaged values of PSA for Analysis I. The critical value of PSA is obtained from the largest microstructure (900*300*900 µm^3). The table shows the minimum life (corresponding to a probability of 0.001) for each microstructure set (having identical simulation volume) obtained by extrapolation.

6.3 Discussion

In this work, a phenomenological crystal plasticity model is used which is a length-scale independent model, due to computational efficiency considerations compared to strain gradient models. However, the usage of the non-local averaging scheme in the post-processing of the mesoscale fields indirectly leads to the inclusion of a local length-scale dependence to the field values, since the regularizing scheme accounts for the nearest neighbors in the calculations. From Figure 6.4, it has been shown that the non-local averaging scheme preserves the microstructural heterogeneity and localization behavior as compared with the band- and grain- averaging schemes, which is consistent with the findings reported in Ref. [64].

The scatter in the fatigue lives is caused by the inherent variability in the material microstructure, namely the grain sizes, morphologies, and orientations, grain boundary character distribution, and pore sizes and locations [4,5]. Each SEM under consideration (Figure 6.1) has a unique arrangement of grains and pores. Although the macroscopic loading conditions are the same, the microstructural variability results in different spatial distributions of the mesoscale field quantities among the SEMs and different maximum values of the associated fatigue metrics causing the scatter in fatigue lives, as shown in Figure 6.5. The fatigue life predictions from the six fatigue metrics are in good agreement with the experimental data. A detailed assessment of the modes of failure is necessary to understand the performance of the metrics as compared to one another.

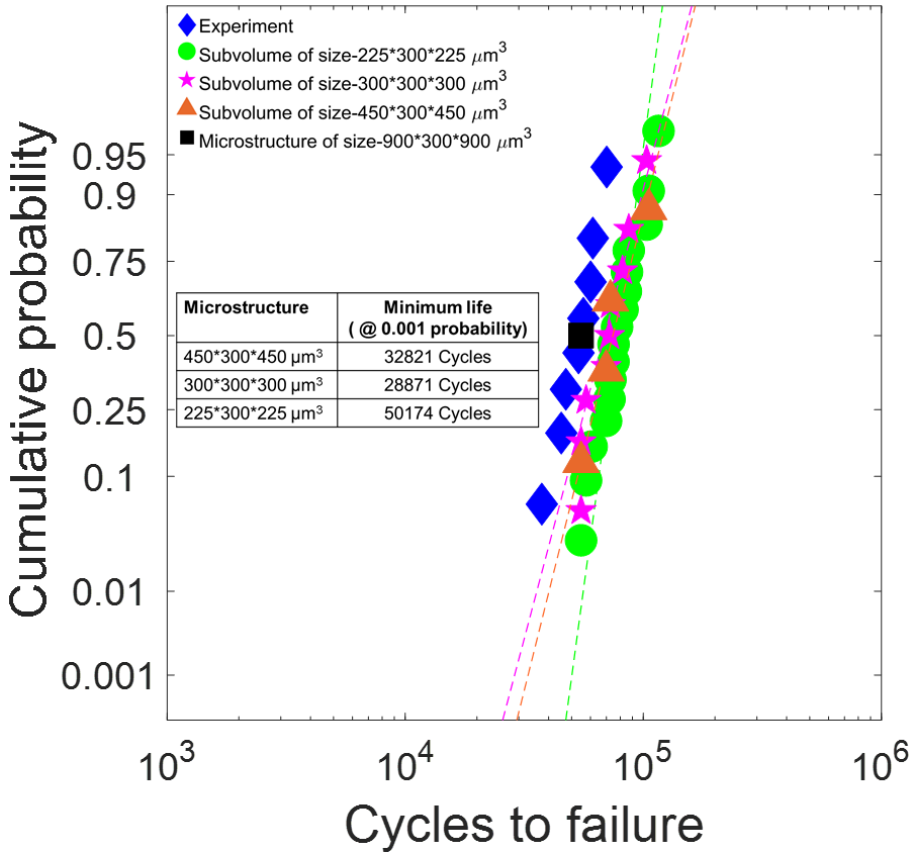

Figure 6.9 Fatigue life prediction using non-local averaged values of PSA for Analysis II. The critical value of PSA is obtained from the largest microstructure (900*300*900 µm^3). The table shows the minimum life (corresponding to a probability of 0.001) for each sub-volume set obtained by extrapolation.

The predicted modes of failure, namely, the free surfaces, a grain/twin boundary in the bulk, and a pore, are mechanistically relevant to fatigue crack initiation and subsequent small crack

propagation. At a free surface, there is less constraint to plastic flow because of the traction free condition, which causes glide of dislocations potentially resulting in the formation of surface extrusions and subsequent crack initiation [154,155]. At a grain/twin boundary in the bulk, dislocations can pile up resulting in the increase of the local stress concentration, leading to a crack [156,157]. A pore is a geometrical discontinuity, which causes a local stress concentration and has less constraint to plastic flow, due to the lack of material, causing the pore to be a potential crack initiator depending on the size, location, and proximity to an adjacent pore or free surface [66]. The six metrics considered in this study can potentially capture all three modes of failure.

Four pores (from SEMs 1, 7, 12, and 14) are consistently being identified as the failure mode by all six metrics, as seen from Figure 6.6. The metrics **M3** and **M6** identify additional pores as failure modes as compared to the other four metrics. There is an inherent bias towards the pores by the metrics formulated from $\tau_{max}+\sigma_h$. This is possibly due to the reason that these are stress-enhanced metrics made of two different stress quantities and hence, have a significant influence on the geometric stress concentration of the pores. In a statistical sense, they also predict less free surface failures (< 50%), while in experiments, a significant percentage of failures are from the free surface. Additionally, the metrics, **M5** and **M6**, result in non-conservative scatter predictions as compared to the scatter predicted by the remaining four metrics (Figure 6.6). For the above reasons, the metrics **M3**, **M5**, and **M6**, are considered less significant as compared to the remaining three metrics. Out of the remaining three metrics, **M1** and **M3** will be assessed here. The modes of failure predicted by **M1** and **M3** are identical for each SEM under consideration, as shown in Figure 6.6. The correlation between the metrics mentioned above is because of the coupling between the resolved shear stress and the shear strains at a slip system level, as shown in the flow rule expression, and potentially, a single slip-system is more dominant than others. This observation is consistent with the results reported in the references [62–64]. Since these two metrics are tightly correlated, one of them, **M1,** is considered for further analysis.

Between the predictions using **M1** and **M2**, there is a very slight difference in the modes of failure as observed from Figure 6.6. For SEM10, **M1** predicts the failure mode to be at the GB in the bulk of the specimen, while **M2** predicts failure at the free surface. A closer look at the hotspot element predicted by **M2** reveals that the location of failure corresponds to that of the intersection between a grain boundary and a free surface. Such failure instances were also observed experimentally in

the prior works [68,93]. However, for this exception, both results from **M1** and **M2** estimate ~50% of failures at a free surface, which correlates in a statistical sense to post mortem fractography results, where we observed a higher number of failures at free surfaces. While the modes of failures are similar, a detailed analysis of the hotspot elements revealed that the predictions by **M1** and **M2** are the same for eight of the SEMs but are different for the other seven SEMs. Unlike **M3, M2** considers the contribution of the entire Cauchy stress tensor; hence takes into account the multi-axial effects at a spatial location within the SEM, which potentially causes a difference in the location of failure prediction as compared to **M1**. However, it should be noted that hotspot elements as predicted by **M1** in the non-conforming cases also have extreme values of the **M2** (>99.999th percentile) although not exhibiting the maximum value.

The post mortem fractography has indicated that none of the samples showed a pore-mediated failure, out of the eight samples analyzed (Figure 3.4), while we see ~25% failures from pores using the fatigue metrics, **M1** or **M2** (Figure 6.6). This discrepancy is expected and is due to the stochasticity in the insertion of pores in the microstructures (Section 3.1). First, the pore sizes are sampled from the tails of the distribution (>98th percentile) obtained from the μXSCT characterization, making the pores more favorable to fail in simulations as compared to the experiments. Second, the microstructure surrounding the pore has a strong influence in governing the failure between the pore and other modes [66], which is not the same in simulations and experiments. The pore-driven failure cases seen in the simulations have provided additional insights as discussed and do not affect the key takeaways of the present work.

The use of microstructures with reduced volumes (as compared to the test specimen or components) is a common practice in the crystal plasticity modeling community, mainly due to the computational cost involved in simulating large microstructures. For example, the CPFE simulation of the largest microstructure (Figure 6.7(d)) takes ~12x times longer to complete the simulation as compared to the 300*300*300 μm^3 SEMs (Figure 6.1). In this work, we have systematically varied the simulation volumes (Figure 6.7) and obtained the fatigue lives as shown in Figure 6.8. The median fatigue life of the largest microstructure (Figure 6.7(d)) is 54707, which corresponds to the median experimental life, because the calibration for the critical value of the failure metric was performed with the largest microstructure. From Figure 6.8, the median fatigue lives of the microstructures in Figure 6.7 (e), (f), and (g) are 40049, 36721, and 31238, respectively,

which means that the median lives are increasing with increase in the simulation volume, which is quite contrary to the weakest link theory [4]. This discrepancy is potentially due to the use of the traction-free boundary conditions used in all the 30 microstructure in Analysis I (Figure 6.7). As the size of the microstructure decreases, the number of grains within the microstructure decreases, which in turn causes a larger percentage of grains in the simulation volume to be adjacent to one of the free surfaces, causing the deformation to be accommodated more at the surface than at the bulk. The effect of traction-free BCs becomes very pronounced in the smallest microstructures (Figure 6.7(g)), which possess fewer grains in the bulk of the material. Out of the sixteen microstructures of the smallest volume simulated, fourteen exhibited free-surface mediated failures. Moreover, a significant scatter, and a non-uniform slope is observed for the smallest sized microstructures (225*300*225 μm^3) from Figure 6.8, which could be attributed to this size microstructure not containing a sufficient number of grains to represent the strength characteristics of the material (i.e. not constituting an SEM), which potentially caused a significant variation in the resulting maximum values of the PSA. Hence, the smallest sized microstructures with traction-free BCs are not suitable to obtain consistent results in fatigue scatter. The slope of the lognormal distribution obtained from the microstructures of sizes, 300*300*300 μm^3 and 450*300*450 μm^3 is reasonably uniform and correlates well with the experimental slope. Overall, the results in Figures 11 indicate a complex interaction between the simulation volume and the BCs in governing the scatter in fatigue lives.

In order to decouple the size of the domain used for life predictions and the corresponding boundary conditions, an additional analysis (Analysis II) used the resulting micromechanical fields from the largest CPFE simulation for subsequent predicted lifetime assessment. The micromechanical fields from the 900*300*900 μm^3 (Figure 6.7(h)) were segmented into different sub-volumes. Each sub-volume will experience a unique set of surrounding constraints based on its spatial location in the largest microstructure. For each sub-domain in the maximum value of the PSA value was obtained through a non-local regularization scheme to assess the predicted fatigue life, as shown in Figure 6.9. The median lives for sub-volumes of sizes, 450*300*450 μm^3, 300*300*300 μm^3, 225*300*225 μm^3 are 71274, 72109, 76277, which indicates that the median lives are decreasing with increase in the volume, which is consistent with the weakest link theory and reported in Ref. [4]. The maximum value of PSA among a set of identically sized sub-volumes will correspond to the maximum PSA value of the entire microstructure (Figure 6.7(h)). This could

be seen in Figure 6.9, where the minimum fatigue lives for different sub-volume sets exhibit the same value (align along the y-axis). By definition, a weakest link model will result in lower lives for larger simulation volumes, which can be problematic when comparing CPFE simulations to components are multiple length scales greater in size. It can be seen that this phenomenon starts to saturate in the results shown. Moreover, in Analysis I, the introduction of a relatively larger of percentage of grains subjected to free surfaces (and thereby traction free surfaces) result in more likely locations of failure and therefore lower fatigue lives. It should be noted that pre-determining the realistic microstructural constraints for the CPFE simulations of SEMs is challenging, and additional work is needed to ascertain appropriate simulation volumes and boundary conditions for comparison of CPFE results to specimen and component level data. Albeit, given the significant percentage of fatigue failures occurring at the free surfaces, traction-free BCs on SEMs for input into CPFE is a suitable choice to deduce the mode of failure.

The optimal simulation volume of the microstructure (or the number of grains in the microstructure) with the use of traction-free BCs is the one that can accurately capture the slope of the experimental fatigue life distribution. From Figure 6.8, the microstructures of size 450*300*450 μm^3 (containing 445 grains on average) seem to be the most optimal out of the simulations conducted in this study. However, models of size 300*300*300 μm^3 (containing 192 grains on average) are reasonable except for an outlier in the plot. The deviation could be potentially due to fewer grains (149) in that particular microstructure. Moreover, the models of size 300*300*300 μm^3 are computationally tractable as compared to the microstructures of size 450*300*450 μm^3, which takes ~3x more computational time to complete these simulations as compared to the former. For safe-life design methodologies, which are based on determining the statistically minimum fatigue life, the life to failure at a probability of 0.001 (or B0.1 life) is estimated by extrapolation of the data points [40–42]. The B0.1 lives were predicted and are shown in the inset of Figure 6.8. The minimum lives for the microstructures 450*300*450 μm^3 and 300*300*300 μm^3 are very close to each other, which also confirms the optimality of the microstructure of size 300*300*300 μm^3. From the above results, it is concluded that a minimum of ~200 grains are potentially sufficient within the polycrystalline aggregate to obtain reliable estimates of fatigue lives using CPFE simulations. It is emphasized that the above analyses were performed for a microstructure with an equiaxed grain structure and random texture.

The crystal plasticity-based fatigue lifing framework could be used to generate a substantial amount of fatigue life data to obtain the minimum statistical life for the safe-life approach, thus reducing the overall experiments needed to be conducted. A physically-based model as the one used in this work can significantly reduce the time and cost in the current qualification procedures [158], especially for AM materials, which involves significant uncertainty in the fatigue performance and also enables a simulation-based design framework moving away from empiricism.

6.4 Conclusions

In the present work, six fatigue metrics from microstructure-sensitive crystal plasticity finite element simulations were used to assess the fatigue behavior of an additively manufactured material. Additional CPFE simulations were performed to understand the role of the simulation volume and microstructure constraints in the resulting fatigue scatter predictions. The key points are summarized below:

- The non-local averaging technique is used to mitigate the spurious effects of distorted elements in the SEMs, while also associating a length-scale to the mesoscale metric under consideration. It is also shown to preserve the localization of the mechanical fields caused by the heterogeneous deformation when compared to the band- and grain-averaging schemes.
- Six fatigue metrics are used, one is plastic strain-based, and the rest of the five metrics are a composite measure of plastic strain, and local stress state. All six metrics predict the scatter in fatigue life with reasonable accuracy as compared to the experimental fatigue data.
- The metrics containing the stress term, $\tau_{max}+ \sigma_h$ (**M4 and M6**), exhibited a bias towards the pore-mediated failures. The hotspot predictions by PSA (**M1**) and W^p (**M2**) showed a larger number of surface-mediated failures, which agrees with observations from post mortem fractography results. The hotspot elements predicted by **M1** and **M2** were different in some of the cases, however, the hotspot elements predicted by **M1** were found to have extreme values (>99.999th percentile) of **M2** although not exhibiting the maximum value.

- The prediction of scatter in fatigue lives is significantly dependent on both the choice of the simulation volume and the microstructure constraints. The minimum number of grains within the polycrystalline aggregate to obtain reliable estimates of fatigue lives were estimated to be ~200 grains with the use of the traction-free boundary conditions, although additional size studies are necessary to use these CPFE simulations within a fatigue prognosis framework.
- The crystal plasticity-based fatigue lifing framework is potentially beneficial in realizing the safe-life design with significant reduction in the experiments to identify the statistical minimum fatigue life, and accelerating the material qualification process.

7. VALIDATING THE MICROSTRUCTURE-SENSITIVE FATIGUE CRACK INITIATION USING CRYSTAL PLASTICITY SIMULATIONS AND HIGH-ENERGY X-RAY EXPERIMENTS

In this chapter, high-fidelity CPFE models are created with different twin instantiations, using multi-modal data sets including the 3D microstructure map (from NF-HEDM), porosity information (from μCT), accurate boundary conditions (from FF-HEDM), and representative twin distributions (from EBSD). These models are then used to validate the location of fatigue crack initiation as observed from μCT and to understand the role of twins on the influence of local micromechanical fields and crack initiation. The remainder of the chapter is organized as follows. Section 7.1 details the simulation framework including the constitutive model description. Results and discussion are presented in Sections 7.2 and 5, respectively. Lastly, the conclusions of this work are given in Section 7.4. The results and analysis provided in this chapter have been published in the Ref. [159].

7.1 Simulation setup

7.1.1 Microstructural model creation

The grain- and pore- maps obtained from high-energy X-ray experiments, and the statistical twin information obtained via EBSD analysis are utilized to instantiate three models (with different twin instantiations) as input to the CPFE simulations and subsequent failure location analysis. Hexahedral elements are used for model, as the mesh can be directly generated from the voxel-based microstructures. A mesh size of 6 μm is chosen for this study, which ensures that there will be ~ 4000 elements per grain in the FE model, which is sufficient to capture the intragranular heterogeneous deformation for subsequent failure predictions [160] and also makes the CPFE simulations computationally tractable.

Three voxel-based simulation volumes, each of dimension 978 x 978 x 798 μm were created to represent the gauge section of the fatigue test specimen (Figure 7.1(a)). Each voxel in the simulation was then mapped with either the grain information (including identification number (ID) and orientation) or a pore ID. The first volume does not consist of any twins while the second

and third volume are instantiated with twins. Each volume could be divided into three partitions as per the z-plane, namely, the ROI at the center of the simulation and the padding regions on both ends of the ROI (Figure 7.1(b)). Each padding region has a height of 222 μm and the ROI at the center is 354 μm tall. The mapping of information to the unassigned voxels of the simulation volumes are described in the forthcoming paragraphs.

First, the resolution of the initial grain map obtained from NF-HEDM was coarsened to 6 x 6 x 6 μm using DREAM.3D [115] and three different variants (Figure 7.1(e)-(g)) were created by including the pores and segmenting the twins. It should be noted that the μCT porosity data has a fine resolution (1.17 μm) as compared to the working resolution of 6 μm. By volume equivalence, one voxel in the post-processed NF-HEDM grain map corresponds to 135 voxels in the μCT dataset. The mapping process of pores from μCT data to post-processed NF-HEDM grain map is as follows. For each voxel, say P, in the post-processed NF-HEDM grain map, 135 voxels (nearest to the centroidal position of P) are identified in the μCT dataset. If more than 40% of the voxels (out of 135) in the μCT data represent an intensity value that is associated with the threshold of a pore, then the P^{th} voxel is labeled as a pore in the variant model. The threshold value of 40% was determined by a sensitivity analysis. The first microstructure variant, without annealing twins, is shown in Figure 7.1(e). The second and the third microstructure variants are both created by first segmenting twins in the post-processed NF-HEDM followed by the mapping of pores (using the same procedure outlined above). The segmentation of the twins is performed as per the procedure outlined in Ref. [114], which ensures that the twins inserted match the EBSD characterization data in a statistical sense. Moreover, the twin segmentation process is random in nature and hence, the second and third microstructure variants have different instantiation of twins, as shown in Figures 2(f), and (g), respectively. The three microstructure variants were respectively mapped (on a voxel to voxel basis) to the ROI of the three simulation volumes (Figure 7.1(b)).

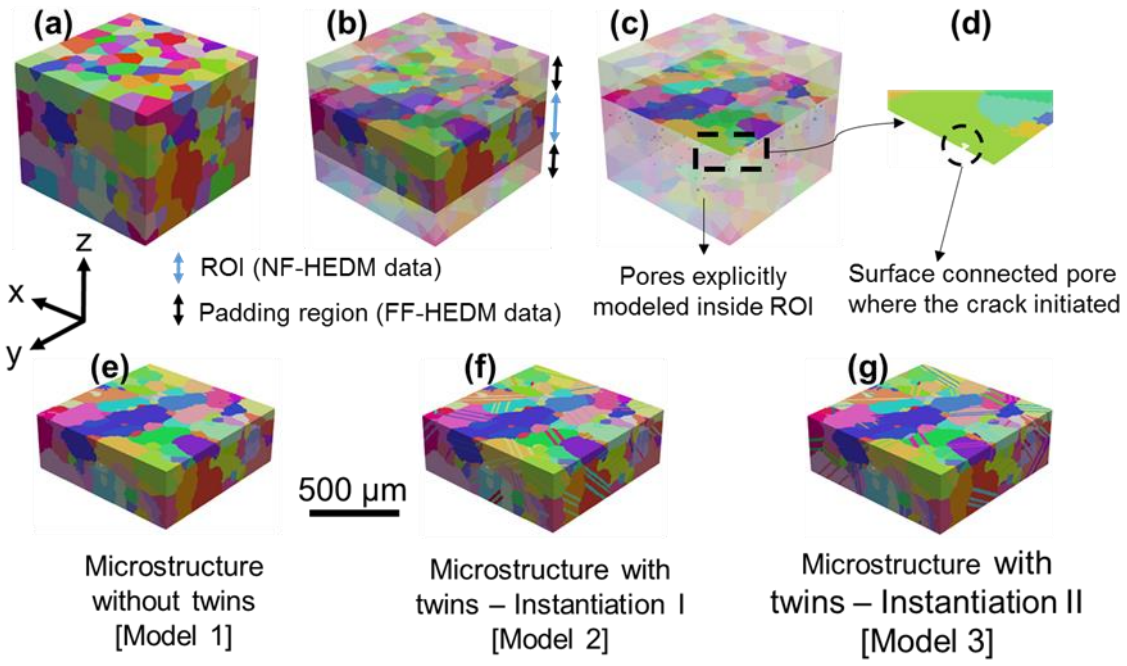

Figure 7.1(a) The general construction of the microstructure model for use in CPFE simulations, (b) the partitions in the microstructure model, namely, the ROI (opaque view) and the padding regions (transparent view), (c) the plane of failure observed from the experiment and the pores explicitly modeled inside the ROI, (d) the magnified view of the surface pore where the experimental crack initiated, and the ROI of the: (e) microstructural model without twins, (f) microstructural model with twins (Instantiation I), and (g) microstructural model with twins (Instantiation II). All the three microstructural models have the same padding regions.

Second, the FF-HEDM data is used to map the voxels in the padding regions (Figure 7.1(b)) of the simulation volumes. The padding regions are additional volumes of the material included in the simulation domain primarily for the application of the boundary conditions (BCs). The addition of these regions effectively shifts the boundary faces vertically (on which the loading is applied) farther from the ROI. The inclusion of the padding regions thus eliminates any spurious effects on the results obtained in the ROI, caused due to the BCs, as per the Saint-Venant's principle. For each simulation volume, the information in the top and bottom z-faces of the ROI region is extended in the respective directions to the length of seven voxels (i.e. 42 μm) to provide a smooth transition in the microstructural features between the ROI and the padding regions. Each unassigned voxel in the top- ($618\ \mu m < z \leq 978\ \mu m$) and bottom- ($0 \leq z < 180\ \mu m$) padding regions is mapped to the nearest grain centroid obtained from the FF-HEDM data. The assignment procedure outlined here closely follows the references [94,95], which results in a Voronoi

representation for the remaining volume (composed of unassigned voxels in the padding regions). In order to avoid any sudden transitions between the ROI and padding regions, a grain boundary smoothing algorithm, as described in Ref. [98], is employed only for the grains within the padding regions without disturbing the structure of the ROI region. Lastly, the voxel-based simulation volumes are converted to a hexahedron mesh (C3D8 elements) using DREAM.3D, and the elements labelled as pores were deleted from the FE mesh.

7.1.2 Loading and boundary conditions

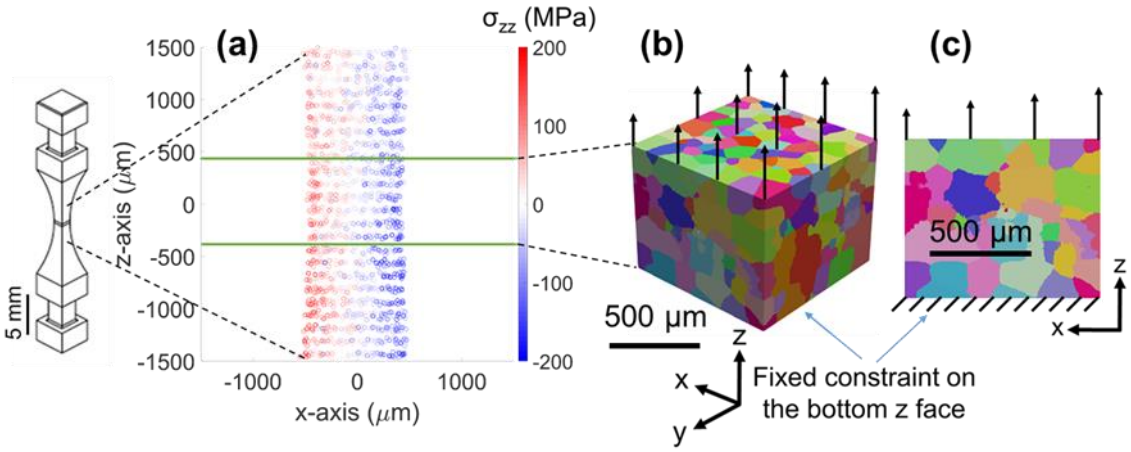

Figure 7.2(a) The grain averaged stresses in the loading direction (σ_{zz}) at the minimum load point as obtained from FF-HEDM data over a length of 3 mm in the specimen. The bounds within the green lines represent the height considered for microstructure model creation including the ROI and padding regions (Figure 7.1). The gradient in stress distribution along x signifies the existence of a slight bending moment, and the boundary conditions used in the CPFE simulations during the loading step shown on the (b) 3D microstructure and (c) the 2D x-z plane. The bottom z face is fixed and a combined bending and axial stress is applied on the top z face.

It is important to accurately capture the loading state of the specimen from the experiment to aid in comparisons with the CPFE simulation results. To this end, the grain-averaged stress data in the loading direction (σ_{zz}) obtained from the FF-HEDM (at cycle 21), as shown in Figure 7.2(a), is analyzed. The σ_{zz} plot obtained at the minimum load point indicates a stress gradient along the x-axis, which is due to the existence of a slight bending moment about y-axis (Figure 7.2). The resultant bending moment (M_{yy}) is calculated using the following equation:

$$M_{yy} = \iint x\, \sigma_{zz} dx\, dy \tag{1}$$

M_{yy} was obtained to be 30 N-mm. Following this analysis, the stress due to bending was calculated as

$$\sigma_{\text{bending}} = -M_{yy}\, x / I_{yy} \tag{2}$$

where, x is the x-coordinate of a given voxel centroid, I_{yy} is the area moment of inertia about the y-axis.

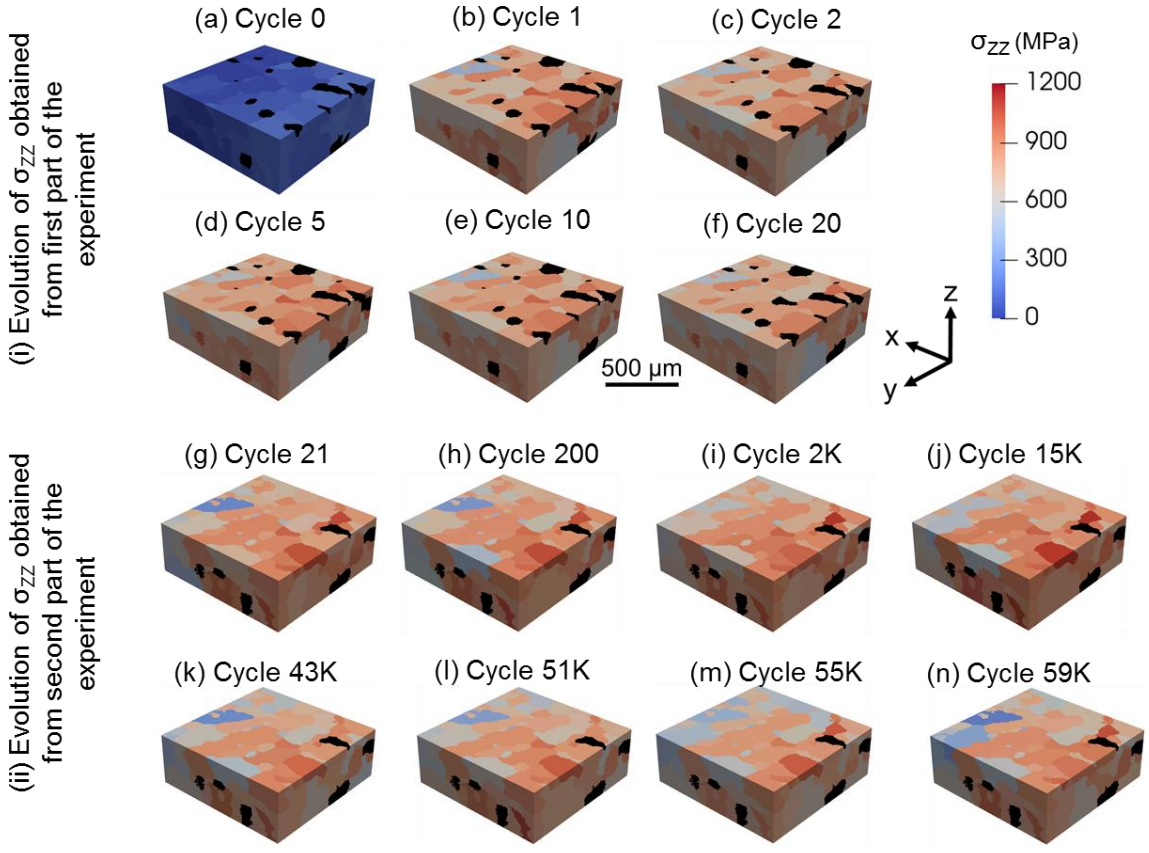

Figure 7.3 Evolution of the grain-averaged stresses in the loading direction (σzz) with loading cycles obtained from FF-HEDM experiments corresponding to (a) the first part of the experiment ((a)-(f)) (b) the second part of the experiment ((g)-(n)). Stress at cycle 0 corresponds to the residual state and for cycles 1 – 59K, the stress is obtained at the peak loading point of the cycle.

As mentioned in Section 363.5, the maximum applied axial stress ($\sigma_{\max}$) is 800 MPa. The effective applied stress on the specimen at the maximum loading point is the addition of the $\sigma_{\max}$ and σ_{bending} components, as shown in Figure 7.2(b,c). The prediction of the most probable location of crack initiation is based on the maximum values of the fatigue metrics, which constitute the local stress tensor and the accumulated slip. Hence, the choice of loading cycles for the CPFE simulations relies on the spatial evolution of stress and accumulated slip. To this end, the spatial evolution of grain-averaged σ_{zz} with the loading cycles obtained from FF-HEDM, as shown in Figure 7.3, is analyzed. It should be noted that the loading conditions of the test specimen were obtained based on the FF-HEDM data acquired during the second part of the experiment. From the σ_{zz} plots corresponding to cycles 21 – 59K (Figure 7.3), the spatial heterogeneity of the stress distribution is preserved with the loading cycles although there were minor variations in the magnitude of stress values. For the grain of interest (where the crack initiated), the maximum variation of stress with the loading cycles was less than 8%, indicating that there was no significant evolution of the stress values. When there is no stress redistribution with the loading cycles, the spatial heterogeneity of the accumulated slip is also preserved with the loading cycles [161]. Based on the above observations and the computational costs, each simulation volume is subjected to one loading cycle with the effective stress values. One CPFE simulation takes ~ 15 days to be completed when run on 300 processors in parallel.

7.2 Results

From the experimental analysis, the fatigue crack nucleated near a pore located at a free surface from the μCT data. Crack initiation is strongly related to a high degree of heterogeneity in the deformation caused by the irreversible dislocation motion with cyclic loading [39]. FF-HEDM provides essential information to quantify the deformation heterogeneity via gradients in the elastic strain and local lattice misorientations [162,163], which could be used to obtain insights into

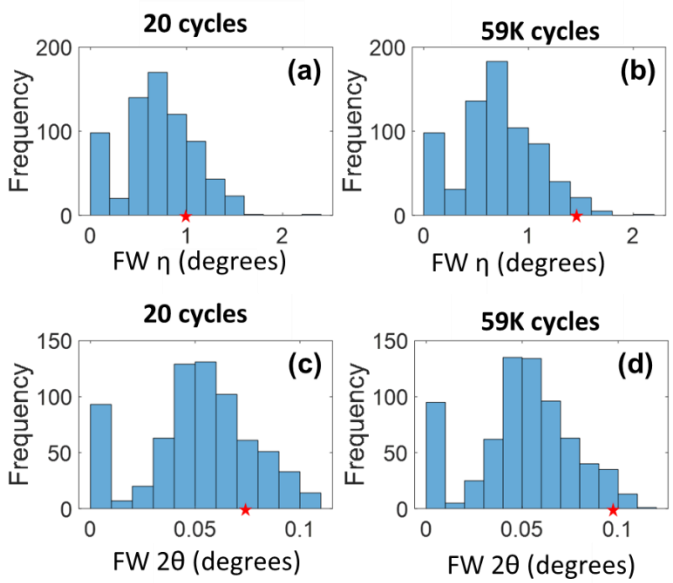

Figure 7.4 Histogram of the averaged full width (FW) in η coordinate at (a) 20 cycles and (b) 59000 cycles, and in 2θ coordinate at (c) 20 cycles and (d) 59K cycles obtained from FF-HEDM experiments within the ROI region and with the grain of interest marked by a red star.

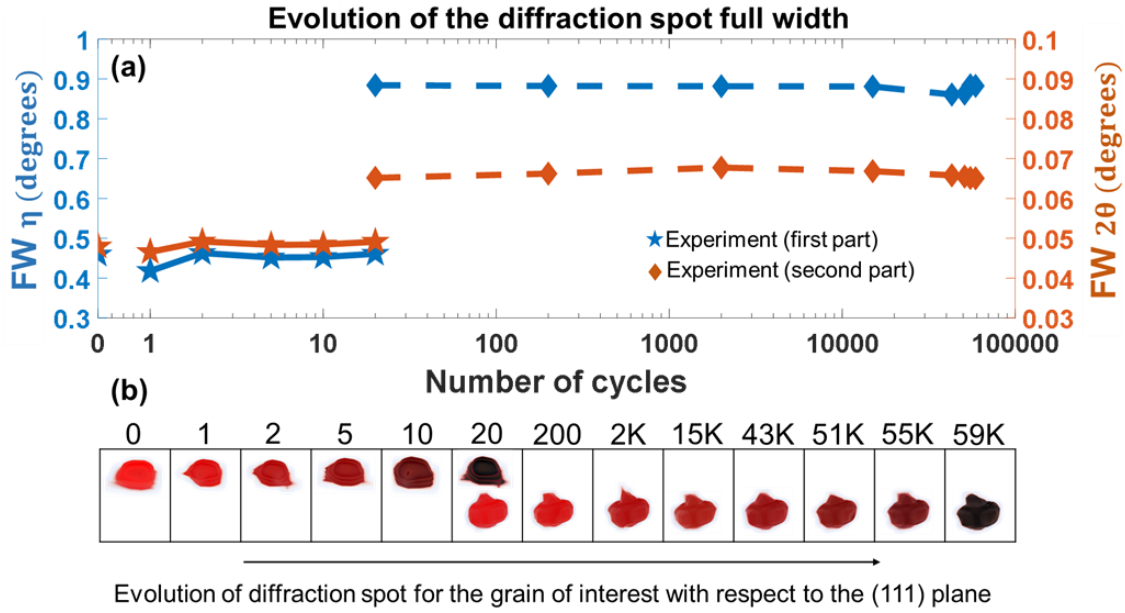

Figure 7.5 Evolution of the (a) full width (FW) in directions η and 2θ, and (b) diffraction spot corresponding to the (111) plane for the grain of interest with respect to the applied loading cycles.

deformation and failure of the polycrystalline material. The aforementioned gradient measures could be obtained by quantifying the changes in the shape of a diffraction spot as outlined in [164],

assuming that the background noise and distortions with respect to the point spread function on the detector remain constant. The full width (FW) values of the distribution in the radial (2θ) and azimuthal (η) coordinates provide information on the grain-averaged- intragranular elastic strain heterogeneity and intragranular misorientation. To improve the ability to capture vital information corresponding to minute changes within a grain, which can manifest as faint spreads in the 2θ and η directions, the extent of the full width has been reported instead of commonly reported full width at half maximum (FWHM) spreads. In Figure 7.4, the histograms of the FW (averaged over the four spots corresponding to the most active slip plane, i.e. the (111)) in 2θ and η coordinates for all the grains within the ROI is shown. Moreover, the value of the FW for the crack-initiated grain is marked in the histogram. The crack initiating grain displays high values of the FW in both the 2θ and η directions, although the crack initiating grain does not correspond to the maximum value. One of the primary reasons for this observation is that the grain-averaged information is not sufficient, in and of itself, to probe the micro-crack nucleation event, which is a highly-localized intragranular event for coarse grain material, without large notches or inclusions present. In addition, the evolution of the FW values in 2θ and η coordinates for the crack initiating grain with cyclic loading is shown in Figure 7.5. We do not see a significant evolution in the FW values (Figure 6) potentially due to the reason that the macroscopic loading is in the HCF regime, which means there is micro plasticity within the microstructure, occurring at the sub-grain level. The experimentally derived grain-scale metrics are important to understand the heterogeneous deformation; however, these metrics are not sufficient to pinpoint the underlying mechanisms of crack initiation. The limitation of the grain-scale resolution in the X-ray experiments could be overcome by the use of the experimentally informed CPFE simulations, which offers a higher resolution (voxel by voxel) representation of the micromechanical fields.

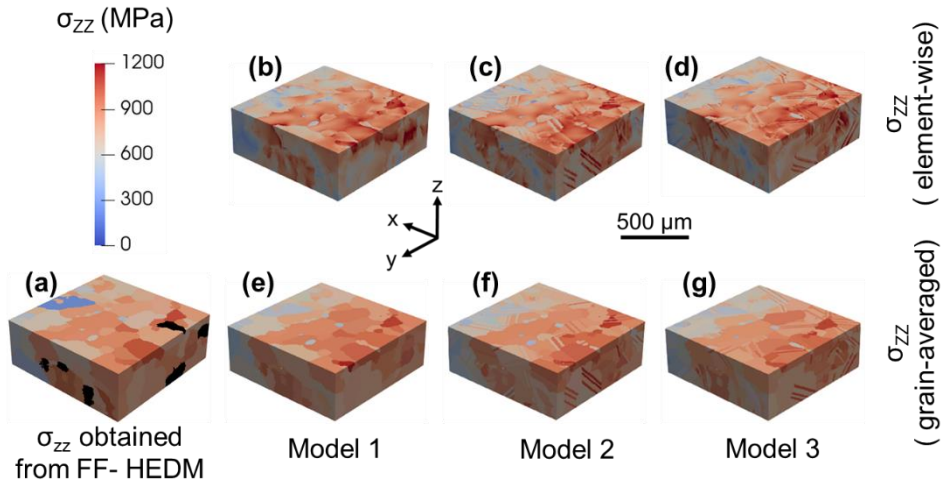

Figure 7.6 Comparing the stress in the loading direction (σ_{zz}) obtained from the (a) FF-HEDM experiments, and (b) CPFE simulations of the three models. The simulation results are shown for ((b)-(d)) element and ((e)-(g)) grain-averaged. σ_{zz} in the experiment was obtained in cycle 21, and σ_{zz} in simulations were obtained at cycle one; all stress values are shown at the maximum loading point. The black colored features indicate unregistered grains.

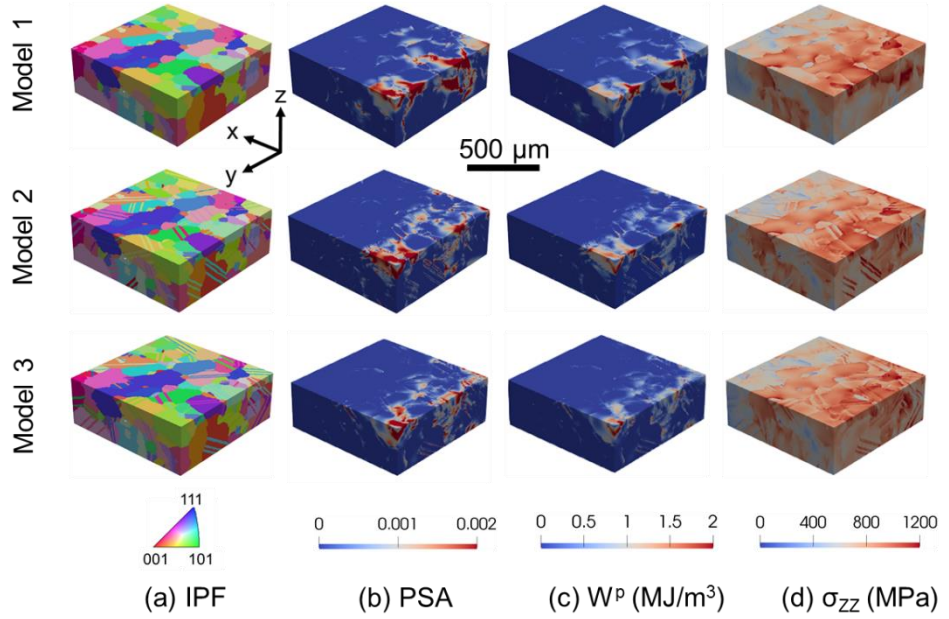

Figure 7.7 Comparison of (a) grain maps via an inverse pole figure (IPF) representation, (b) plastic strain accumulation (PSA), (c) plastic strain energy density (W^p), and (d) stress in the loading direction (σ_{zz}), among the three models.

Three CPFE models (with different twin instantiations) were reconstructed using the experimental data to represent the fatigue test specimen. Moreover, the realistic boundary conditions were captured using the stress data obtained from FF-HEDM. A slight bending moment was observed due impart to the small gauge section of the sample and tight tolerance in manufacturing the sample. This bending moment was taken into account in the model by applying appropriate boundary conditions. As an initial verification step, the grain-averaged stress values in the loading direction obtained from the FF-HEDM and CPFE simulations are compared, as shown in Figure 7.6. The grain-averaged stress plots from the experiment and the models look similar, implying that CPFE model (including the BCs and CP parameters) was appropriate. One CPFE simulation was performed without accounting for the bending moment, the details are provided in Appendix A. After building confidence in capturing the grain-scale stress distributions, the CPFE model is used to predict the potential failure locations and assess the fatigue model's predictive capability.

To identify the likely locations of failure, surrogate measures calculated from CPFE simulations are most commonly used. In this work, two metrics are chosen from a previous study by the authors to investigate crack initiation [146]. The first metric is the plastic strain accumulation (PSA) [137,138], which is the cumulative slip measure with contributions from each active slip system and is defined as

$$\mathrm{PSA} = \int \sqrt{\frac{2}{3}\mathbf{L_p}:\mathbf{L_p}}\, dt \tag{7.1}$$

The second metric is the cumulative plastic strain energy density ($\mathrm{W^p}$), which corresponds to the dissipative energy due to plastic deformation [148–150]. It is defined as

$$\mathrm{W^p} = \oint \boldsymbol{\sigma}:\boldsymbol{L_p} dt \tag{7.2}$$

where, $\boldsymbol{\sigma}$ is the Cauchy stress tensor.

The PSA, W^p, and σ_{ZZ} obtained from the CPFE simulations of the three models are compared in Figure 7.7. The figure indicates differences in the spatial distribution of the respective mesoscale fields among the three models associated with the local microstructural heterogeneity due to the different twin instantiations among the three models.

The most likely location of failure (or the hotspot) for each model was identified using the maximum value of the metrics, PSA and W^p. Hence, two hotspots are obtained per model. For Model 1, the hotspot determined by the PSA metric is obtained at the point indicated as X_B and the hotspot predicted by the W^p metric is located at X_c, as shown in Figure 7.8. Location X_B is adjacent to a grain boundary with a misorientation of ~ 46^o and a free surface, and X_C is adjacent to a grain boundary with a misorientation of ~ 54^o and at a pore. For Models 2 and 3 (i.e. with statistical twin insertion), both the metrics, PSA and W^p, predicted location X_A as the hotspot (Figure 7.8). X_A is at a surface-connected pore and happens to be the actual crack location as observed from the experiment.

To understand the reason for the shift in the predicted failure locations (to X_A) after twin insertion, a thorough quantitative analysis of the failure metrics at X_A, X_B, and X_C is performed. From Table 7.1, the PSA at X_B significantly decreases in Models 2 and 3, this describes the shift as per the PSA predictive metric. In Models 2 and 3, the value of W^p, decreases at X_C and increases at X_A, which explains the shift in the failure location to X_A as per W^p. The detailed analysis regarding the failure predictions from various models and the role of twins on the influence of the local micromechanical fields are explained in the next section.

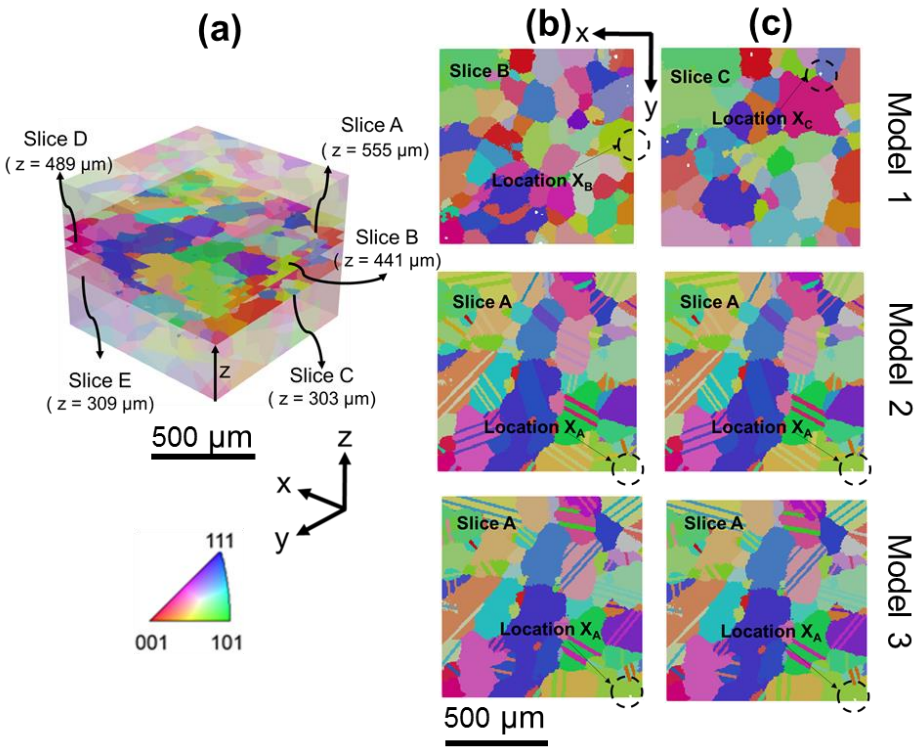

Figure 7.8(a) x-y slices of interest with their respective z position from the bottom face, and the failure locations from the CPFE simulations of the three models predicted using (b) the plastic strain accumulation metric and (c) the plastic strain energy density metric. Slices D and E are referenced in the Appendix (Figure A1).

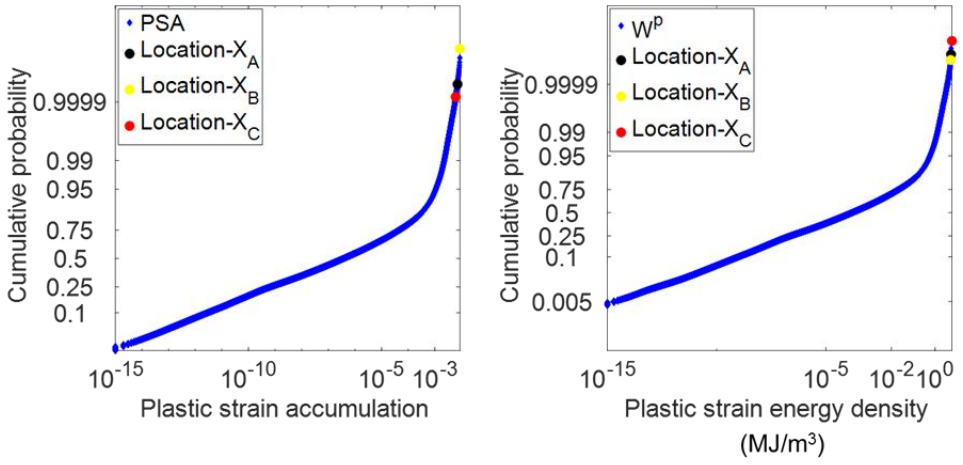

Figure 7.9 Cumulative distribution plots of (a) plastic strain accumulation and (b) plastic strain energy density within the ROI of Model 1 with the failure locations X_A, X_B, and X_C overlaid.

7.3 Discussion

In this study, we link the CPFE model and the high-energy X-ray experiments at a grain-scale to validate the predicted location of microstructure-sensitive fatigue crack initiation using the fatigue metrics, namely, PSA and W^p. Moreover, the integrated framework is used to investigate the microstructural rationale behind the crack initiation and understand the role of twins on the local micromechanical fields and crack initiation.

Table 7.1 The values of the metrics, PSA, and W^p at points of interest (X_A, X_B, and X_C) obtained for each model.

Location	**Micromechanical fields**	**Model 1**	**Model 2**	**Model 3**
X_A	PSA	0.0071	0.0079	0.0072
	W^P (MJ/m^3)	5.3776	6.3252	5.6386
X_B	PSA	0.0088	0.0013	0.0017
	W^P (MJ/m^3)	5.1638	0.7542	0.8971
X_C	PSA	0.0060	0.0045	0.0045
	W^P (MJ/m^3)	5.9391	5.0094	3.7796

Table 7.2 The stress components at the location X_B obtained for each model.

Stress components (MPa)	Model 1	Model 2	Model 3
σ_{XX}	-109.25	2.60	45.83
σ_{YY}	241.38	122.33	169.80
σ_{ZZ}	1159.80	930.54	974.91
σ_{XY}	37.17	21.35	71.00
σ_{XZ}	108.32	8.30	-48.71
σ_{YZ}	166.99	-57.28	-216.54

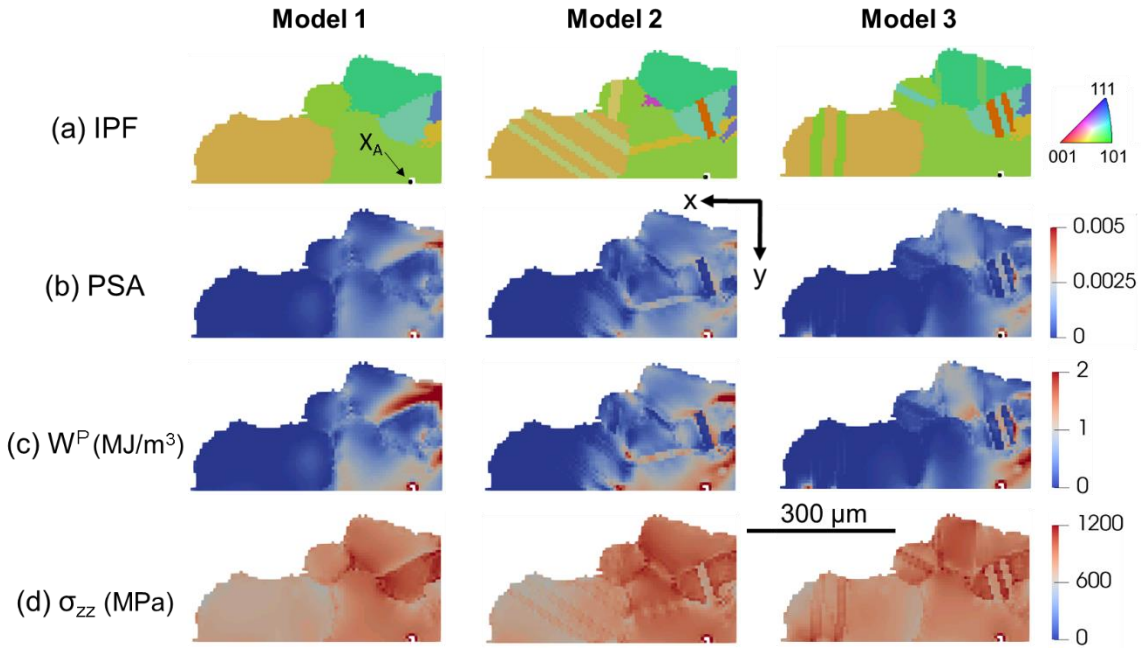

Figure 7.10(a) The inverse pole figure map (IPF) of the grain slice containing the point X_A along with the nearest neighbors from each model, and the corresponding micromechanical fields obtained from each simulation: (b) plastic strain accumulation (PSA), (c) plastic strain energy density (W^p), and (d) stress in the loading direction (σ_{zz}).

From the experimental characterization, the fatigue crack initiates near a surface-connected pore on the test specimen, which is consistent with the experimental findings reported in prior studies [9,165]. The mechanistic reasons for the crack initiation could potentially be due to the following:

(i) pores act as stress concentrator points, and in particular, a pore close to the surface is more detrimental than a pore at the bulk [66,165], and (ii) free surface facilitates glide of dislocations due to the traction free boundary condition leading to accommodation of more plastic deformation [166].

From Figure 7.8, the predictions for the locations of failure as per the PSA and W^p metrics using Model 1 (i.e. the microstructure without twins) do not coincide with the actual location of failure. However, the failure predictions using Models 2 and 3 (i.e. the microstructures with twins) have provided an unambiguous one-to-one match of the location of crack initiation with the extreme values of the failure metrics. It is clear that the insertion of twins have improved the accuracy of the predicted location of failure; however, to understand how significantly twins have altered the micromechanical field values at X_A, the cumulative probability of PSA and W^p within the ROI of Model 1 are assessed, as shown in Figure 7.9. The value of the PSA metric at X_A is at the 99.998^{th} percentile and the value of W^p metric at X_A is the fourth highest value. Hence, the values of both the failure metrics belong to the extreme tails of the distribution, albeit they do not correspond to the highest value of each metric.

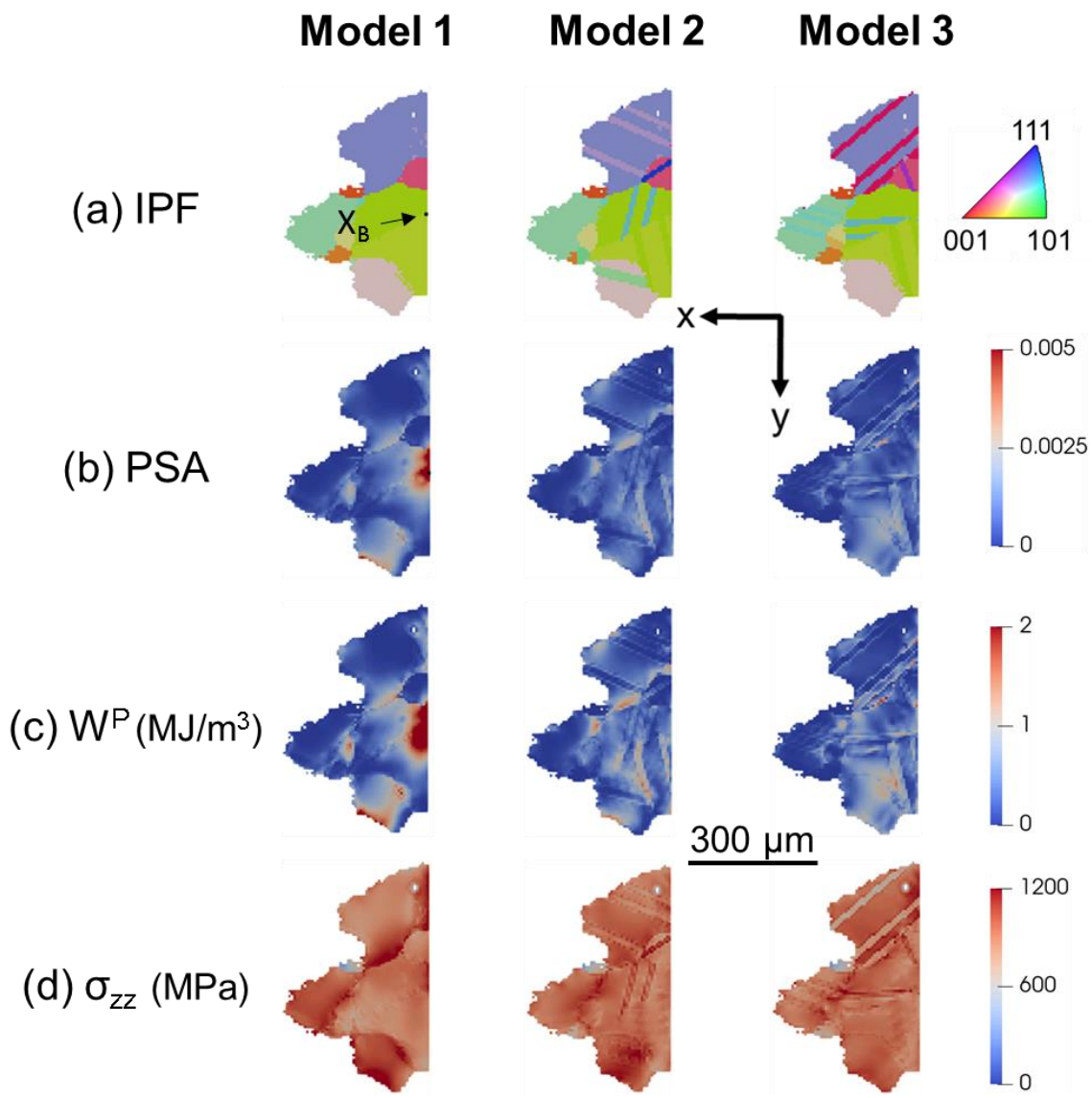

Figure 7.11(a) The inverse pole figure map (IPF) of the grain slice containing the point X_B along with the nearest neighbors from each model, and the corresponding micromechanical fields obtained from each simulation: (b) plastic strain accumulation (PSA), (c) plastic strain energy density (W^p), and (d) stress in the loading direction (σ_{zz}).

After twin insertion, there is an increase in the values of both failure metrics at X_A, while at the locations X_B and X_C, there is a decrease in the values of the failure metrics (Table 7.1). To understand the role of twins in general, the location X_B is chosen for further analysis, since at X_B there was a drastic decrease of the failure metrics. To this end, more fundamental quantities such as the local stress tensor and the individual slip system activity are obtained at X_B from all the models. From Table 7.2 , the insertion of twins have resulted in changes to the entire stress tensor.

Some of the stress components (σ_{xx}, σ_{yz}) have changed their sign. The change in the stress tensor is due to the elastic and plastic incompatibilities induced by the twin boundaries. A similar observation was also made by Peralta et al. [90] via analytical studies. A slip system, α, is considered active if the quantity $\left|\frac{\tau-\chi}{g}\right| \geq 1$. From the analysis, it was found that the insertion of the twins have changed the slip system activity in Models 2 and 3. In Model 1, the slip systems $(\bar{1}11)[\bar{1}\bar{1}0]$ and $(\bar{1}\bar{1}1)[011]$ were active. In Model 2, the slip systems $(\bar{1}\bar{1}1)[110]$ and $(1\bar{1}1)[\bar{1}01]$ were active, and in Model 3, only the slip system $(\bar{1}11)[\bar{1}\bar{1}0]$ was active. This is due to the change of the local stress state. The spatial comparison of PSA and WP at the locations of interest (X_A, X_B, and X_C) for the three models are shown in Figures 7.10-7.12, respectively, which illustrates the role of twins on the local micromechanical fields. We are able to validate the location of failure despite the lack of deterministic knowledge of the twin placement within Models 2 and 3. In summary, twins can be favorable to fatigue life by providing a strengthening mechanism to the material without resulting in substantial loss of ductility, but twins can also be a likely location for crack initiation, once a persistent slip band has formed [55].

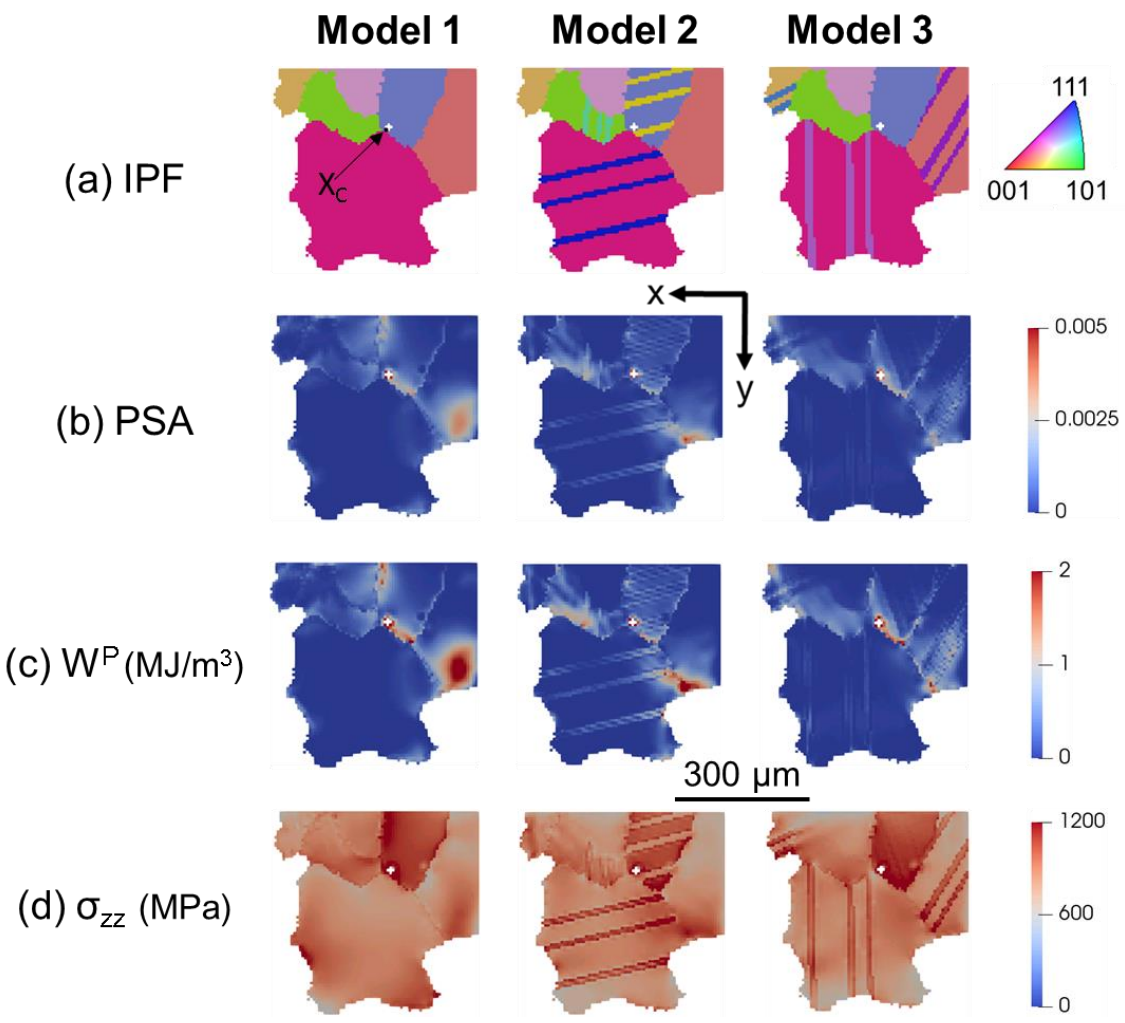

Figure 7.12(a) The inverse pole figure map (IPF) of the grain slice containing the point X_C along with the nearest neighbors from each model, and the corresponding micromechanical fields obtained from each simulation: (b) plastic strain accumulation (PSA), (c) plastic strain energy density (W^p), and (d) stress in the loading direction (σ_{zz}).

The validation study performed in this work builds confidence in assessing the fatigue crack-initiation using the failure metrics, namely PSA, and W^p, obtained via crystal plasticity simulations. The current qualification procedures require extensive experimental testing, which is both time and cost intensive [3]. A validated microstructure-sensitive failure model, such as the one shown in this work, provides a pathway to perform a suite of virtual experiments under different loading conditions, thus reducing a significant number of physical testing. This study is a step forward in realizing a microstructural sensitive model-based accelerated qualification approach.

7.4 Conclusions

In this work, we create three CPFE models (with different twin instantiations) informed from the multi-modal characterization data obtained from NF-HEDM, FF-HEDM, μCT, and EBSD. These models are subsequently used to perform validation studies with respect to the location of crack initiation and to understand the role of twins on crack initiation. The key findings of this study are summarized below:

- From the μCT analysis, the fatigue crack was found to initiate at a surface-connected pore.
- The predicted locations of failure using microstructure without twins do not coincide with the actual location of failure, while the probabilistic insertion of twins (i.e. in Models 2 and 3) have resulted in an exact correlation for the location of crack initiation with the extreme values of the failure metrics, namely, PSA and W^P.
- The insertion of twins within the model cause changes in the local stress tensor and the slip system activity, which in turn influences the calculated values of the fatigue metrics. There is no uniform correlation between the twin insertion and the resulting failure metrics.

8. CONCLUSIONS AND FUTURE WORK

8.1 Conclusions

The overall objective of this dissertation was to supplement the understanding of various aspects of the fatigue response of an additively manufactured alloy as a function of material microstructure and defects with the use of both predictive crystal plasticity modeling and experiments. To realize this objective, first a suite of tools necessary to perform crystal plasticity simulations is developed. The toolset includes: (a) an automated framework to create and mesh 3D statistically equivalent microstructures based on the information of the microstructural attributes (grain size data, twin fraction, and texture) obtained from electron backscatter diffraction, (b) a genetic algorithm based framework to estimate the material parameters using the macroscopic stress-strain response, and (c) a regularization scheme to mitigate the spurious effects of the distorted elements inherent to the meshing process and report consistent results. Using this toolset, four studies were performed as a part of this dissertation:

8.1.1 Estimation of critical porosity characteristics

- Pores were explicitly added to the microstructural instantiations by systematically varying the location, size and proximity between pores. With damage indicator parameters obtained from the crystal plasticity simulations, the likely locations of failure were assessed and classified as pore-mediated and crystallographic features-induced.
- The major finding of this study is the estimation of the characteristics such as the pore size and proximity (to an adjacent pore or free surface) that led to the occurrence of only pore-mediated failures.
- This work potentially influences decisions in process parameter optimization, and choice of non-destructive characterization methods.

8.1.2 Examining metrics for fatigue life prediction

- Multiple metrics based on plastic strain and local stress were used to predict the locations of failure relative to the microstructural features and were compared to the fractography

results. Two of the metrics, plastic strain accumulation and plastic strain energy density, correlated well in a statistical sense with the fractography experiments.

- The same set of metrics were used to obtain the scatter in the fatigue life due to microstructural variability and compared with the experimental scatter data. The scatter predictions from all metrics agreed well with the experiments.
- The highlight of this study is the identification of appropriate fatigue metrics in the fatigue prognosis of additively manufactured materials.

8.1.3 Role of simulation volume and microstructural constraints on life predictions

- Two sets of analyses were performed in this study. In the first analysis, the microstructure is segmented into smaller sized microstructures, with each microstructure used as an input for the CPFE simulation and the associated fatigue life predictions. While in the second analysis, the large simulation volume is used as input into the CPFE simulation and the resulting micromechanical fields are segmented for use in fatigue prognosis (effectively changing the boundary conditions to account for the neighboring microstructural constraints).
- The major finding of this study is two-fold: (i) it was shown that the fatigue life prediction is governed by a complex interaction between the simulation volume and the boundary conditions, and (ii) with the use of traction free boundary conditions, the minimum number of grains in the microstructural instantiation to reliably predict the scatter in fatigue life ~ 200 grains. These findings provide informed guidelines for the fatigue prognosis using reduced simulation volumes.

8.1.4 Validation of microstructure-sensitive fatigue crack initiation using crystal plasticity simulations and high-energy X-ray experiments

- 3D microstructural models, with various twin distributions, were developed based on high-energy X-ray experiments, specifically grain and pore maps, as well as appropriate boundary conditions. These CPFE models were used to probe the fatigue crack initiation of IN718 produced via additive manufacturing, thus evaluating the predictive capabilities of the CPFE model.

- The results indicated an unambiguous one to one correlation for the location of crack initiation with the extreme values of the failure metrics, namely, plastic strain accumulation and the plastic strain energy density, thus building confidence in the usage of crystal plasticity models for the fatigue assessment.

Overall, the four studies in this dissertation provide a promising step towards the realization of using a suite of virtual experiments to complement and reduce the number of full-scale physical testing, thereby resulting in a microstructural sensitive model-based accelerated qualification of a material for use in safety-critical applications.

8.2 Future work

Based on the research studies performed in this dissertation, here is a list of potential problems for the future work:

- In Chapter 4, the generation of 3D mesh for the polycrystalline microstructure involves multiple tools and the distortion of few elements is unavoidable due to the current workflow procedure that ensures a smooth topology to the grain boundaries. This limitation could be addressed by the development of a robust meshing routine to obtain high quality elements as well as provisions for localized meshing near the grain boundaries.
- In Chapter 5, a CPFE framework was used to study the role of porosity towards the crack initiation behavior of IN718. The same framework could be used to include additional defect structures such as inclusions and surface roughness, and study the synergetic effects of all the defect structures on the fatigue behavior of IN718.
- In Chapter 5, the critical pore characteristics (in terms of the pore size and clustering) were estimated for a specific average grain size. As changes in the process parameters leads to changes in the average grain size, the current estimate may not be valid. However, the CPFE framework proposed in Chapter 5 could be used to obtain the estimates of critical porosity characteristics as a function of the average grain size.
- In Chapter 6, it was shown that CPFE simulations of large microstructures (close to the size of the specimen's gauge section) is computationally intensive. The development of

more efficient solvers will provide opportunities for gaining mechanistic insights into failure at a specimen scale.

- In Chapter 7, the validation efforts were performed corresponding to a single mode of failure (i.e. at a surface-connected pore). This study could be further enhanced by performing validation studies corresponding to multiple modes of failure by using the methods described in Chapter 7.

APPENDIX A. PREDICTING LOCATION OF FAILURE USING UNIAXIAL BOUNDARY CONDITIONS

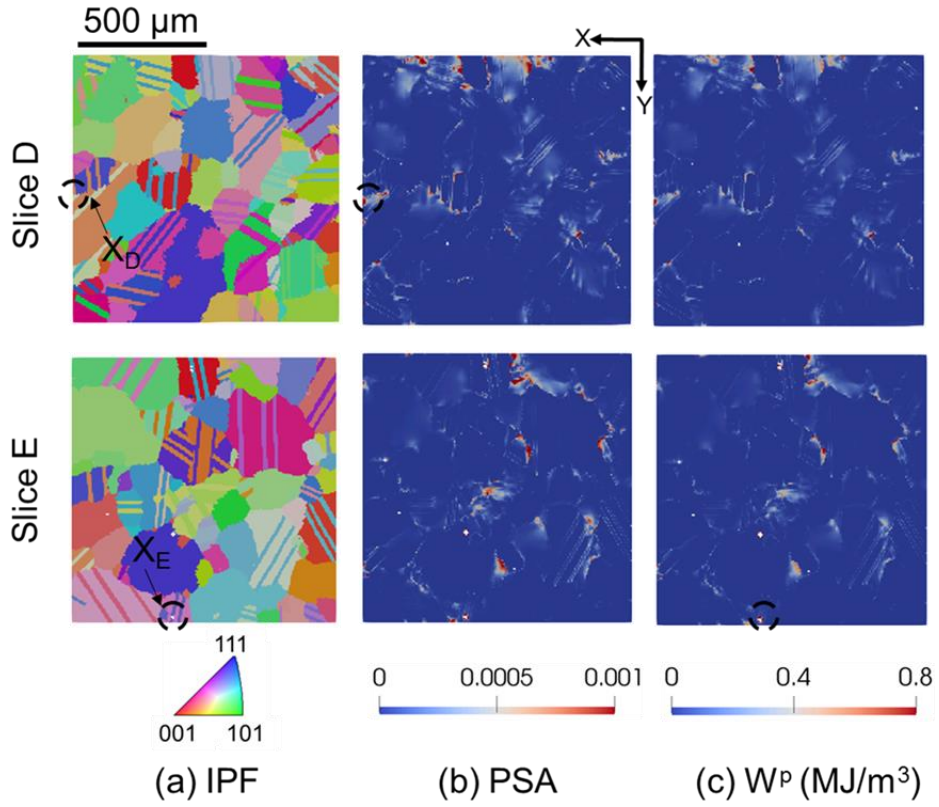

Figure A1(a) An inverse pole figure (IPF) representation of the predicted planes of failure (slices D and E) using Model 3 with uniaxial loading conditions, (b) the plastic strain accumulation plot, and (c) plastic strain energy density plot of the slices D and E, with the respective locations of failure encircled. Location XD is predicted by PSA and XE by Wp.

The prediction of microstructure-sensitive fatigue crack initiation in the CPFE modeling community is commonly carried out using the application of simplified boundary conditions (BCs). This is mainly due to the difficulty in obtaining the exact BCs, assumptions that the specimen is perfectly aligned, or limitations in the size of the simulation volume. However, in this study, HEDM experiments were used to extract the stresses in grains adjacent to the volume of interest, thereby providing the BCs to apply to the simulation. These BCs were used for failure predictions

as discussed in earlier Sections. This data also provides an opportunity to study the role of BCs towards the prediction of fatigue crack initiation. To this end, one CPFE simulation was performed using Model 3 by the application of simple uniaxial loading conditions, which was achieved by setting the σ_{bending} component to zero as described in Section 3.2. The model was subjected to one loading cycle with a maximum stress of σ_{max} at R=0, and subsequently the likely locations of failure were predicted using the metrics, PSA, and W^p. The predicted hotspots as per the metrics, PSA and W^p, were obtained to be X_D and X_E, respectively, as shown in Figure A1. The z coordinates of slices D and E (Figure A1) relative to the simulation volume is given in Figure 7.8. Location XD is situated at a grain boundary near the free surface and XE is located sub-surface at the intersection of a pore and a twin boundary. It was previously shown that Model 3, when subjected to the experimentally determined loading conditions (tension and slight bending), predicted X_A as the location of failure, which was the experimentally observed location of failure. Thus, by not accounting for the slight bending moment (Figure 3) in the current simulation, we observe a shift in the predicted locations of failure.

REFERENCES

[1] M. Seifi, A. Salem, J. Beuth, O. Harrysson, J.J. Lewandowski, Overview of Materials Qualification Needs for Metal Additive Manufacturing, Jom. 68 (2016) 747–764. doi:10.1007/s11837-015-1810-0.

[2] A. Yadollahi, N. Shamsaei, Additive manufacturing of fatigue resistant materials: Challenges and opportunities, Int. J. Fatigue. 98 (2017) 14–31. doi:10.1016/j.ijfatigue.2017.01.001.

[3] W.E. Frazier, Metal additive manufacturing: A review, J. Mater. Eng. Perform. 23 (2014) 1917–1928. doi:10.1007/s11665-014-0958-z.

[4] M.D. Sangid, H.J. Maier, H. Sehitoglu, An energy-based microstructure model to account for fatigue scatter in polycrystals, J. Mech. Phys. Solids. 59 (2011) 595–609. doi:10.1016/j.jmps.2010.12.014.

[5] S.R. Yeratapally, M.G. Glavicic, M. Hardy, M.D. Sangid, Microstructure based fatigue life prediction framework for polycrystalline nickel-base superalloys with emphasis on the role played by twin boundaries in crack initiation, Acta Mater. 107 (2016) 152–167. doi:10.1016/j.actamat.2016.01.038.

[6] F. Roters, P. Eisenlohr, L. Hantcherli, D.D. Tjahjanto, T.R. Bieler, D. Raabe, Overview of constitutive laws, kinematics, homogenization and multiscale methods in crystal plasticity finite-element modeling: Theory, experiments, applications, Acta Mater. 58 (2010) 1152–1211. doi:10.1016/j.actamat.2009.10.058.

[7] S. Leuders, M. Thöne, a. Riemer, T. Niendorf, T. Tröster, H. a. Richard, H.J. Maier, On the mechanical behaviour of titanium alloy TiAl6V4 manufactured by selective laser melting: Fatigue resistance and crack growth performance, Int. J. Fatigue. 48 (2013) 300–307. doi:10.1016/j.ijfatigue.2012.11.011.

[8] P. Edwards, M. Ramulu, Fatigue performance evaluation of selective laser melted Ti-6Al-4V, Mater. Sci. Eng. A. 598 (2014) 327–337. doi:10.1016/j.msea.2014.01.041.

[9] S. Tammas-Williams, P.J. Withers, I. Todd, P.B. Prangnell, The Influence of Porosity on Fatigue Crack Initiation in Additively Manufactured Titanium Components, Sci. Rep. 7 (2017) 1–13. doi:10.1038/s41598-017-06504-5.

[10] E. Brandl, U. Heckenberger, V. Holzinger, D. Buchbinder, Additive manufactured AlSi10Mg samples using Selective Laser Melting (SLM): Microstructure, high cycle fatigue, and fracture behavior, Mater. Des. 34 (2012) 159–169. doi:10.1016/j.matdes.2011.07.067.

[11] M.J. Couper, A.E. Neeson, J.R. Griffiths, Casting Defects and the Fatigue Behaviour of an Aluminium Casting Alloy, Fatigue Fract. Eng. Mater. Struct. 13 (1990) 213–227. doi:10.1111/j.1460-2695.1990.tb00594.x.

[12] Q.G. Wang, D. Apelian, D.A. Lados, Fatigue behavior of A356-T6 aluminum cast alloys. Part I. Effect of casting defects, J. Light Met. 1 (2001) 73–84. doi:10.1016/S1471-5317(00)00008-0.

[13] H. Danninger, B. Weiss, The influence of defects on high cycle fatigue of metallic materials, J. Mater. Process. Technol. 143–144 (2003) 179–184. doi:10.1016/S0924-0136(03)00409-6.

[14] S.J. Polasik, J.J. Williams, N. Chawla, Fatigue crack initiation and propagation of binder-treated powder metallurgy steels, Metall. Mater. Trans. A. 33 (2002) 73–81. doi:10.1007/s11661-002-0006-8.

[15] H.T. Pang, P.A.S. Reed, Fatigue crack initiation and short crack growth in nickel-base turbine disc alloys - The effects of microstructure and operating parameters, Int. J. Fatigue. 25 (2003) 1089–1099. doi:10.1016/S0142-1123(03)00146-4.

[16] S. Dezecot, J.Y. Buffiere, A. Koster, V. Maurel, F. Szmytka, E. Charkaluk, N. Dahdah, A. El Bartali, N. Limodin, J.F. Witz, In situ 3D characterization of high temperature fatigue damage mechanisms in a cast aluminum alloy using synchrotron X-ray tomography, Scr. Mater. 113 (2016) 254–258. doi:10.1016/j.scriptamat.2015.11.017.

[17] S. Benedictus-deVries, A. Bakker, G.C. a. M. Janssen, H. de Wit, Fatigue Crack Initiation Behavior of Welded AA5083 in a Seawater Environment, J. Eng. Mater. Technol. 126 (2004) 199. doi:10.1115/1.1651098.

[18] X. Zhou, D. Wang, X. Liu, D.D. Zhang, S. Qu, J. Ma, G. London, Z. Shen, W. Liu, 3D-imaging of selective laser melting defects in a Co-Cr-Mo alloy by synchrotron radiation micro-CT, Acta Mater. 98 (2015) 1–16. doi:10.1016/j.actamat.2015.07.014.

[19] R. Cunningham, S.P. Narra, C. Montgomery, J. Beuth, A.D. Rollett, Synchrotron-Based X-ray Microtomography Characterization of the Effect of Processing Variables on Porosity Formation in Laser Power-Bed Additive Manufacturing of Ti-6Al-4V, Jom. 69 (2017) 479–484. doi:10.1007/s11837-016-2234-1.

[20] S. Siddique, M. Imran, M. Rauer, M. Kaloudis, E. Wycisk, C. Emmelmann, F. Walther, Computed tomography for characterization of fatigue performance of selective laser melted parts, Mater. Des. 83 (2015) 661–669. doi:10.1016/j.matdes.2015.06.063.

[21] G. Kasperovich, J. Haubrich, J. Gussone, G. Requena, Correlation between porosity and processing parameters in TiAl6V4 produced by selective laser melting, Mater. Des. 105 (2016) 160–170. doi:10.1016/j.matdes.2016.05.070.

[22] R. Cunningham, A. Nicolas, J. Madsen, E. Fodran, E. Anagnostou, M.D. Sangid, A.D. Rollett, Analyzing the effects of powder and post-processing on porosity and properties of electron beam melted Ti-6Al-4V, Mater. Res. Lett. 5 (2017) 516–525. doi:10.1080/21663831.2017.1340911.

[23] S. Khademzadeh, S. Carmignato, N. Parvin, F. Zanini, P.F. Bariani, Micro porosity analysis in additive manufactured NiTi parts using micro computed tomography and electron microscopy, Mater. Des. 90 (2016) 745–752. doi:10.1016/j.matdes.2015.10.161.

[24] K. Jurrens, Energetics Incorporated, Measurement Science Roadmap for Metal-Based Additive Manufacturing, Addit. Manuf. (2013) 86. doi:10.1007/s13398-014-0173-7.2.

[25] F.A. McClintock, A Criterion for Ductile Fracture by the Growth of Holes, J. Appl. Mech. (1968) 363–371.

[26] J.R. Rice, D.M. Tracey, On the ductile enlargement of voids in triaxial stress fields∗, J. Mech. Phys. Solids. 17 (1969) 201–217. doi:10.1016/0022-5096(69)90033-7.

[27] A. Needleman, Void growth in an elastic-plastic medium., 1 (1972). doi:10.1115/1.3422899.

[28] A.L. Gurson, Continuum Theory of Ductile Rupture by Void Nucleation and Growth: Part I—Yield Criteria and Flow Rules for Porous Ductile Media, J. Eng. Mater. Technol. 99 (1977) 2. doi:10.1115/1.3443401.

[29] V. Tvergaard, Tvergaard - On localization in ductile materials containing spherical voids.pdf, 18 (1982) 237–252.

[30] J. Koplik, a. Needleman, Void growth and coalescence in porous plastic solids, Int. J. Solids Struct. 24 (1988) 835–853. doi:10.1016/0020-7683(88)90051-0.

[31] K. Gall, M.F. Horstemeyer, B.W. Degner, D.L. McDowell, J. Fan, On the driving force for fatigue crack formation from inclusions and voids in a cast A356 aluminum alloy, Int. J. Fract. 108 (2001) 207–233. doi:10.1023/A:1011033304600.

[32] J. Fan, D.L. McDowell, M.F. Horstemeyer, K. Gall, Cyclic plasticity at pores and inclusions in cast Al-Si alloys, Eng. Fract. Mech. 70 (2003) 1281–1302. doi:10.1016/S0013-7944(02)00097-8.

[33] Z. Xu, W. Wen, T. Zhai, Effects of pore position in depth on stress/strain concentration and fatigue crack initiation, Metall. Mater. Trans. A Phys. Metall. Mater. Sci. 43 (2012) 2763–2770. doi:10.1007/s11661-011-0947-x.

[34] P. Baicchi, G. Nicoletto, E. Riva, Modeling the influence of pores on fatigue crack initiation in a cast Al-Si alloy, Int. Conf. CRACK PATHS 2006. (2006) 2–9. http://www.gruppofrattura.it/index.php?option=com_docman&task=doc_download&gid=152&Itemid=228.

[35] H. Gao, Z. Zhang, Y. Lai, J. Li, Y. Liu, Influence of crystallographic orientation on growth behavior of spherical voids, J. Cent. South Univ. Technol. (Engl. Ed.). 15 (2008) 830–834. doi:10.1007/s11771.

[36] J.D. Carroll, L.N. Brewer, C.C. Battaile, B.L. Boyce, J.M. Emery, The effect of grain size on local deformation near a void-like stress concentration, Int. J. Plast. 39 (2012) 46–60. doi:10.1016/j.ijplas.2012.06.002.

[37] C.C. Battaile, J.M. Emery, L.N. Brewer, B.L. Boyce, Crystal plasticity simulations of microstructure-induced uncertainty in strain concentration near voids in brass, Philos. Mag. 95 (2015) 1069–1079. doi:10.1080/14786435.2015.1009958.

[38] D.L. McDowell, F.P.E. Dunne, Microstructure-sensitive computational modeling of fatigue crack formation, Int. J. Fatigue. 32 (2010) 1521–1542. doi:10.1016/j.ijfatigue.2010.01.003.

[39] M.D. Sangid, The physics of fatigue crack initiation, Int. J. Fatigue. 57 (2013) 58–72. doi:10.1016/j.ijfatigue.2012.10.009.

[40] J.M. Larsen, S.K. Jha, C.J. Szczepanski, M.J. Caton, R. John, A.H. Rosenberger, D.J. Buchanan, P.J. Golden, J.R. Jira, Reducing uncertainty in fatigue life limits of turbine engine alloys, Int. J. Fatigue. 57 (2013) 103–112. doi:10.1016/j.ijfatigue.2013.01.012.

[41] A.L. Hutson, S.K. Jha, W.J. Porter, J.M. Larsen, Activation of life-limiting fatigue damage mechanisms in Ti – 6Al – 2Sn – 4Zr – 6Mo, 66 (2014) 1–10. doi:10.1016/j.ijfatigue.2014.02.011.

[42] J.M. Larsen, M.J. Caton, S.K. Jha, A.H. Rosenberger, Understanding Materials Uncertainty for Prognosis of Advanced Turbine Engine Materials, (2010) 1–12.

[43] O.H. Basquin, The exponential law of endurance tests, Am. Soc. Test. Mater. 10 (1910) 625–630.

[44] L.F. Coffin Jr., A study of the effects of cyclic thermal stresses on a ductile metal, 1953.

[45] S. S. Manson, Behavior of materials under conditions of thermal stress, 1953.

[46] J. D. Morrow, Cyclic plastic strain energy and fatigue of metals, in: Intern. Frict. Damping, Cycl. Plast., ASTM International, PA, 1965: pp. 45–87.

[47] K.N. Smith, P. Watson, T.H. Topper, A Stress-Strain Function for the Fatigue of Metals, J. Mater. (1970) 767–778.

[48] A. Fatemi, D.F. Socie, A critical plane approach to multiaxial fatigue damage including out-of-phase loading, Fatigue Fract. Eng. Mater. Struct. 11 (1988) 149–165. doi:10.1111/j.1460-2695.1988.tb01169.x.

[49] K. Tanaka, T. Mura, A dislocation model for fatigue crack initiation, ASME J. Appl. Mech. 48 (1981) 97–103.

[50] K. Tanaka, T. Mura, A theory of fatigue crack initiation at inclusions, Metall. Trans. A. 13 (1982) 117–123. doi:10.1007/BF02642422.

[51] G. Venkataraman, Y.W. Chung, T. Mura, Application of minimum energy formalism in a multiple slip band model for fatigue-II. Crack nucleation and derivation of a generalised Coffin-Manson law, Acta Metall. Mater. 39 (1991) 2631–2638. doi:10.1016/0956-7151(91)90079-G.

[52] G. Venkataraman, Y.W. Chung, T. Mura, Application of minimum energy formalism in a multiple slip band model for fatigue - I. Calculation of slip band spacings, Acta Metall. Mater. 39 (1991) 2621–2629. doi:10.1016/0956-7151(91)90078-F.

[53] K.S. Chan, A microstructure-based fatigue-crack-initiation model, Metall. Mater. Trans. A. 34A (2003) 43-? doi:10.1007/s11661-003-0207-9.

[54] M.D. Sangid, H.J. Maier, H. Sehitoglu, A physically based fatigue model for prediction of crack initiation from persistent slip bands in polycrystals, Acta Mater. 59 (2011) 328–341. doi:10.1016/j.actamat.2010.09.036.

[55] M.D. Sangid, H.J. Maier, H. Sehitoglu, The role of grain boundaries on fatigue crack initiation - An energy approach, Int. J. Plast. 27 (2011) 801–821. doi:10.1016/j.ijplas.2010.09.009.

[56] M.M. Shenoy, D.L. McDowell, Constitutive Modeling and Life Prediction in Ni-Base Superalloys, Mech. Eng. Doctor of (2006).

[57] M. Shenoy, Y. Tjiptowidjojo, D. McDowell, Microstructure-sensitive modeling of polycrystalline IN 100, Int. J. Plast. 24 (2008) 1694–1730. doi:10.1016/j.ijplas.2008.01.001.

[58] M. Shenoy, J. Zhang, D.L. McDowell, Estimating fatigue sensitivity to polycrystalline Ni-base superalloy microstructures using a computational approach, Fatigue Fract. Eng. Mater. Struct. 30 (2007) 889–904. doi:10.1111/j.1460-2695.2007.01159.x.

[59] C. Przybyla, R. Prasannavenkatesan, N. Salajegheh, D.L. McDowell, Microstructure-sensitive modeling of high cycle fatigue, Int. J. Fatigue. 32 (2010) 512–525. doi:10.1016/j.ijfatigue.2009.03.021.

[60] C.P. Przybyla, D.L. McDowell, Simulated microstructure-sensitive extreme value probabilities for high cycle fatigue of duplex Ti-6Al-4V, Int. J. Plast. 27 (2011) 1871–1895. doi:10.1016/j.ijplas.2011.01.006.

[61] G.M. Castelluccio, D.L. McDowell, Microstructure and mesh sensitivities of mesoscale surrogate driving force measures for transgranular fatigue cracks in polycrystals, Mater. Sci. Eng. A. 639 (2015) 626–639. doi:10.1016/j.msea.2015.05.048.

[62] J.D. Hochhalter, D.J. Littlewood, R.J. Christ, M.G. Veilleux, J.E. Bozek, A.R. Ingraffea, A.M. Maniatty, A geometric approach to modeling microstructurally small fatigue crack formation: II. Physically based modeling of microstructure-dependent slip localization and actuation of the crack nucleation mechanism in AA 7075-T651, Model. Simul. Mater. Sci. Eng. 18 (2010). doi:10.1088/0965-0393/18/4/045004.

[63] A. Rovinelli, Y. Guilhem, H. Proudhon, R.A. Lebensohn, W. Ludwig, M.D. Sangid, Assessing reliability of fatigue indicator parameters for small crack growth via a probabilistic framework, Model. Simul. Mater. Sci. Eng. 25 (2017). doi:10.1088/1361-651X/aa6c45.

[64] A. Nicolas, N.E.C. Co, J.T. Burns, M.D. Sangid, Predicting fatigue crack initiation from coupled microstructure and corrosion morphology effects, Eng. Fract. Mech. 220 (2019) 106661. doi:10.1016/j.engfracmech.2019.106661.

[65] B. Chen, J. Jiang, F.P.E. Dunne, Is stored energy density the primary meso-scale mechanistic driver for fatigue crack nucleation?, Int. J. Plast. 101 (2018) 213–229. doi:10.1016/j.ijplas.2017.11.005.

[66] V. Prithivirajan, M.D. Sangid, The role of defects and critical pore size analysis in the fatigue response of additively manufactured IN718 via crystal plasticity, Mater. Des. 150 (2018) 139–153. doi:10.1016/j.matdes.2018.04.022.

[67] R. Bandyopadhyay, M.D. Sangid, Crystal plasticity assessment of inclusion- and matrix-driven competing failure modes in a nickel-base superalloy, Acta Mater. 177 (2019) 20–34. doi:10.1016/j.actamat.2019.07.024.

[68] V.V.C. Wan, D.W. MacLachlan, F.P.E. Dunne, A stored energy criterion for fatigue crack nucleation in polycrystals, Int. J. Fatigue. 68 (2014) 90–102. doi:10.1016/j.ijfatigue.2014.06.001.

[69] A. Cruzado, S. Lucarini, J. LLorca, J. Segurado, Microstructure-based fatigue life model of metallic alloys with bilinear Coffin-Manson behavior, Int. J. Fatigue. 107 (2018) 40–48. doi:10.1016/j.ijfatigue.2017.10.014.

[70] K. Kirane, S. Ghosh, M. Groeber, A. Bhattacharjee, Grain Level Dwell Fatigue Crack Nucleation Model for Ti Alloys Using Crystal Plasticity Finite Element Analysis, J. Eng. Mater. Technol. 131 (2009) 021003. doi:10.1115/1.3078309.

[71] M. Anahid, M.K. Samal, S. Ghosh, Dwell fatigue crack nucleation model based on crystal plasticity finite element simulations of polycrystalline titanium alloys, J. Mech. Phys. Solids. 59 (2011) 2157–2176. doi:10.1016/j.jmps.2011.05.003.

[72] S.R. Yeratapally, M.G. Glavicic, C. Argyrakis, M.D. Sangid, Bayesian uncertainty quantification and propagation for validation of a microstructure sensitive model for prediction of fatigue crack initiation, Reliab. Eng. Syst. Saf. 164 (2017) 110–123. doi:10.1016/j.ress.2017.03.006.

[73] A. Bagri, G. Weber, J. Stinville, W. Lenthe, T. Pollock, C. Woodward, Microstructure and Property-Based Statistically Equivalent Representative Volume Elements for Polycrystalline Ni-Based Superalloys Containing Annealing Twins, Metall. Mater. Trans. A. 49 (2018) 5727–5744. doi:10.1007/s11661-018-4858-y.

[74] X. Tu, A. Shahba, J. Shen, S. Ghosh, C. Engineering, Microstructure and property based statistically equivalent RVEs for polycrystalline-polyphase aluminum alloys, Int. J. Plast. 115 (2019) 268–292. doi:10.1016/j.ijplas.2018.12.002.

[75] T. Kanit, S. Forest, Determination of the size of the representative volume element for random composites : statistical and numerical approach, 40 (2003) 3647–3679. doi:10.1016/S0020-7683(03)00143-4.

[76] Committee on Integrated Computational Materials Engineering, Integrated computational materials engineering: A transformational discipline for improved competitiveness and national security, 2008. doi:10.17226/12199.

[77] D.U. Furrer, D.M. Dimiduk, J.D. Cotton, C.H. Ward, Making the Case for a Model-Based Definition of Engineering Materials, Integr. Mater. Manuf. Innov. 6 (2017) 249–263. doi:10.1007/s40192-017-0102-7.

[78] S.R. Stock, Recent advances in X-ray microtomography applied to materials, Int. Mater. Rev. 53 (2008) 129–181. doi:10.1179/174328008X277803.

[79] S.R. Stock, X-ray microtomography of materials, Int. Mater. Rev. 44 (1999) 141–164. doi:10.1179/095066099101528261.

[80] H. Poulsen, Three-dimensional X-ray diffraction microscopy: mapping polycrystals and their dynamics, Springer, 2004.

[81] R.M. Suter, D. Hennessy, C. Xiao, U. Lienert, Forward modeling method for microstructure reconstruction using x-ray diffraction microscopy: Single-crystal verification, Rev. Sci. Instrum. 77 (2006) 123905. doi:10.1063/1.2400017.

[82] S.F. Li, R.M. Suter, Adaptive reconstruction method for three-dimensional orientation imaging, J. Appl. Crystallogr. 46 (2013) 512–524. doi:10.1107/S0021889813005268.

[83] J. V Bernier, N.R. Barton, U. Lienert, M.P. Miller, Far-field high-energy diffraction microscopy: a tool for intergranular orientation and strain analysis, J. Strain Anal. Eng. Des. 46 (2011) 527–547. doi:10.1177/0309324711405761.

[84] L. Margulies, T. Lorentzen, H.F. Poulsen, T. Leffers, Strain tensor development in a single grain in the bulk of a polycrystal under loading, Acta Mater. 50 (2002) 1771–1779. doi:10.1016/S1359-6454(02)00028-9.

[85] H.F. Poulsen, S.F. Nielsen, E.M. Lauridsen, S. Schmidt, R.M. Suter, U. Lienert, L. Margulies, T. Lorentzen, D. Juul Jensen, Three-dimensional maps of grain boundaries and the stress state of individual grains in polycrystals and powders, J. Appl. Crystallogr. 34 (2001) 751–756. doi:10.1107/S0021889801014273.

[86] M.D. Sangid, T.A. Book, D. Naragani, J. Rotella, P. Ravi, A. Finch, P. Kenesei, J.-S. Park, H. Sharma, J. Almer, X. Xiao, Role of heat treatment and build orientation in the microstructure sensitive deformation characteristics of IN718 produced via additive manufacturing, Addit. Manuf. 22 (2018) 479–496.

[87] J. Miao, T.M. Pollock, J. Wayne Jones, Crystallographic fatigue crack initiation in nickel-based superalloy René 88DT at elevated temperature, Acta Mater. 57 (2009) 5964–5974. doi:10.1016/j.actamat.2009.08.022.

[88] C. Blochwitz, W. Tirschler, Twin boundaries as crack nucleation sites, Cryst. Res. Technol. 40 (2005) 32–41. doi:10.1002/crat.200410305.

[89] A. Heinz, P. Neumann, Crack initiation during high cycle fatigue of an austenitic steel, Acta Metall. Mater. 38 (1990) 1933–1940. doi:10.1016/0956-7151(90)90305-Z.

[90] P. Peralta, L. Llanes, J. Bassani, C. Laird, Deformation from twin-boundary stresses and the role of texture: Application to fatigue, Philos. Mag. A Phys. Condens. Matter, Struct. Defects Mech. Prop. 70 (1994) 219–232. doi:10.1080/01418619408242547.

[91] C. Blochwitz, W. Tirschler, Influence of texture on twin boundary cracks in fatigued austenitic stainless steel, Mater. Sci. Eng. A. 339 (2003) 318–327. doi:10.1016/S0921-5093(02)00126-0.

[92] G.M. Castelluccio, D.L. Mcdowell, Effect of annealing twins on crack initiation under high cycle fatigue conditions, (n.d.). doi:10.1007/s10853-012-7021-y.

[93] A. Cerrone, C. Stein, R. Pokharel, C. Hefferan, J. Lind, H. Tucker, R. Suter, A. Rollett, A. Ingraffea, Implementation and verification of a microstructure-based capability for modeling microcrack nucleation in LSHR at room temperature, Model. Simul. Mater. Sci. Eng. 23 (2015) 035006. doi:10.1088/0965-0393/23/3/035006.

[94] T.J. Turner, P.A. Shade, J. V. Bernier, S.F. Li, J.C. Schuren, P. Kenesei, R.M. Suter, J. Almer, Crystal Plasticity Model Validation Using Combined High-Energy Diffraction Microscopy Data for a Ti-7Al Specimen, Metall. Mater. Trans. A Phys. Metall. Mater. Sci. 48 (2017) 627–647. doi:10.1007/s11661-016-3868-x.

[95] K. Kapoor, M.D. Sangid, Initializing type-2 residual stresses in crystal plasticity finite element simulations utilizing high-energy diffraction microscopy data, Mater. Sci. Eng. A. 729 (2018) 53–63. doi:10.1016/j.msea.2018.05.031.

[96] V. Tari, R.A. Lebensohn, R. Pokharel, T.J. Turner, P.A. Shade, J. V. Bernier, A.D. Rollett, Validation of micro-mechanical FFT-based simulations using High Energy Diffraction Microscopy on Ti-7Al, Acta Mater. 154 (2018) 273–283. doi:10.1016/j.actamat.2018.05.036.

[97] R. Bandyopadhyay, A.W. Mello, K. Kapoor, M.P. Reinhold, T.F. Broderick, M.D. Sangid, On the crack initiation and heterogeneous deformation of Ti-6Al-4V during high cycle fatigue at high R ratios, J. Mech. Phys. Solids. 129 (2019) 61–82. doi:10.1016/j.jmps.2019.04.017.

[98] A. Nicolas, A.W. Mello, Y. Sun, D.R. Johnson, M.D. Sangid, Reconstruction methods and analysis of subsurface uncertainty for anisotropic microstructures, Mater. Sci. Eng. A. 760 (2019) 76–87. doi:10.1016/j.msea.2019.05.089.

[99] https://www.eos.info/systems_solutions/metal/systems_equipment/eosint_m280, (2010).

[100] B.A. Dowd, G.H. Campbell, R.B. Marr, V. Nagarkar, S. Tipnis, L. Axe, D.P. Siddons, Developments in synchrotron X-ray computed microtomography at the National Synchrotron Light Source, in: Proc. SPIE, 1999: p. Bellingham, WA, Society of Photo-Optical Instrumen. doi:10.1117/12.363725.

[101] M.L. Rivers, tomoRecon: High-speed tomography reconstruction on workstations using multi-threading, in: Proc. SPIE, 2012. doi:10.1117/12.930022.

[102] D. Gürsoy, F. De Carlo, X. Xiao, C. Jacobsen, TomoPy: A framework for the analysis of synchrotron tomographic data, J. Synchrotron Radiat. 21 (2014) 1188–1193. doi:10.1107/S1600577514013939.

[103] N. Otsu, A Threshold Selection Method from Gray-Level Histograms, IEEE Trans. Syst. Man. Cybern. 9 (1979) 62–66. doi:10.1109/TSMC.1979.4310076.

[104] C.T. Rueden, J. Schindelin, M.C. Hiner, B.E. DeZonia, A.E. Walter, E.T. Arena, K.W. Eliceiri, ImageJ2: ImageJ for the next generation of scientific image data, BMC Bioinformatics. 18 (2017) 1–26. doi:10.1186/s12859-017-1934-z.

[105] C.A. Schneider, W.S. Rasband, K.W. Eliceiri, NIH Image to ImageJ: 25 years of image analysis, Nat. Methods. 9 (2012) 671–675. doi:10.1038/nmeth.2089.

[106] Konrad Z, User's Guide – Avizo, (2017).

[107] M.D. Sangid, P. Ravi, V. Prithivirajan, N.A. Miller, J. Park, ICME Approach to Determining the Critical Pore Size of IN718 Produced by Selective Laser Melting, JOM. (2019). doi:10.1007/s11837-019-03910-0.

[108] P.A. Shade, B. Blank, J.C. Schuren, T.J. Turner, P. Kenesei, K. Goetze, R.M. Suter, J. V. Bernier, S.F. Li, J. Lind, U. Lienert, J. Almer, A rotational and axial motion system load frame insert for in situ high energy x-ray studies, Rev. Sci. Instrum. 86 (2015) 1–9. doi:10.1063/1.4927855.

[109] P.A. Shade, D.B. Menasche, J. V Bernier, P. Kenesei, J.-S. Park, R.M. Suter, J.C. Schuren, T.J. Turner, Fiducial marker application method for position alignment of in situ multimodal X-ray experiments and reconstructions, J. Appl. Cryst. 49 (2016) 700–704. doi:10.1107/S1600576716001989.

[110] H. Sharma, R.M. Huizenga, S.E. Offerman, A fast methodology to determine the characteristics of thousands of grains using three-dimensional X-ray diffraction. I. Overlapping diffraction peaks and parameters of the experimental setup, J. Appl. Crystallogr. 45 (2012) 693–704. doi:10.1107/S0021889812025563.

[111] H. Sharma, R.M. Huizenga, S.E. Offerman, A fast methodology to determine the characteristics of thousands of grains using three-dimensional X-ray diffraction. II. Volume, centre-of-mass position, crystallographic orientation and strain state of grains, J. Appl. Crystallogr. 45 (2012) 705–718. doi:10.1107/S0021889812025599.

[112] A. Khounsary, P. Kenesei, J. Collins, G. Navrotski, J. Nudell, High Energy X-ray Micro-tomography for the characterization of thermally fatigued GlidCop specimen, J. Phys. Conf. Ser. 425 (2013) 212015. doi:10.1088/1742-6596/425/21/212015.

[113] J. Ahrens, B. Geveci, C. Law, ParaView: An End-User Tool for Large Data Visualization, (2005).

[114] R. Bandyopadhyay, V. Prithivirajan, M.D. Sangid, Uncertainty Quantification in the Mechanical Response of Crystal Plasticity Simulations, Jom. 71 (2019) 2612–2624. doi:10.1007/s11837-019-03551-3.

[115] M.A. Groeber, M.A. Jackson, DREAM . 3D : A Digital Representation Environment for the Analysis of Microstructure in 3D, Integr. Mater. Manuf. Innov. (2014) 1–17.

[116] http://dream3d.bluequartz.net/binaries/Help/DREAM3D/, (2013).

[117] M. Groeber, Development of an Automated Characterization- Representation Framework for the Modeling of Polycrystalline Materials in 3D, Ohio State University, 2007.

[118] M.D. Sangid, H. Sehitoglu, H.J. Maier, T. Niendorf, Grain boundary characterization and energetics of superalloys, Mater. Sci. Eng. A. 527 (2010) 7115–7125. doi:10.1016/j.msea.2010.07.062.

[119] L.H. Chan, Synthetic Three-Dimensional Voxel-Based Microstructures that Contain Annealing Twins, Carnegie Mellon University, 2010.

[120] G.Taylor, Plastic strain in metals, J. Inst. Met. 62 (1938).

[121] J. Bishop, R. Hill, A theory of the plastic distortion of a polycrystalline aggregate under combined stresses, Philos. Mag. 42 (1951). doi:10.1080/14786445108561065.

[122] H.J. Bunge, Some Applications of the Taylor Theory of Polycrystal Plasticity, Krist. Und Tech. 5 (1970) 145–175.

[123] C. Geuzaine, J.-F. Remacle, Gmsh: a three-dimensional finite element mesh generator with built-in pre-and post-processing facilities, Int. J. Numer. Methods Eng. 79(11). 0 (2009) 1309–1331. doi:10.1002/nme.2579.

[124] R.J. Asaro, Crystal Plasticity, J. Appl. Mech. 50 (1983) 921. doi:10.1115/1.3167205.

[125] L. Anand, M. Kothari, A computational procedure for rate-independent crystal plasticity, J. Mech. Phys. Solids. 44 (1996) 525–558. doi:10.1016/0022-5096(96)00001-4.

[126] E.H. Lee, Elastic-Plastic Deformation at Finite Strains, J. Appl. Mech. 36 (1969) 1. doi:10.1115/1.3564580.

[127] J.W. Hutchinson, Creep and plasticity of hexagonal polycrystals as related to single crystal slip, Met. Trans A. 8 (1977) 1465–1469. doi:10.1007/BF02642860.

[128] C.O. Frederick, P.J. Armstrong, A mathematical representation of the multiaxial Bauschinger effect, Mater. High Temp. 24 (2007) 1–26. doi:10.1179/096034007x207589.

[129] M.F. Horstemeyer, D.L. McDowell, R.D. McGinty, Design of experiments for constitutive model selection: application to polycrystal elastoviscoplasticity, Model. Simul. Mater. Sci. Eng. 7 (1999) 253–273.

[130] U.F. Kocks, The relation between polycrystal deformation and single-crystal deformation, Metall. Mater. Trans. 1 (1970) 1121–1143. doi:10.1007/BF02900224.

[131] C. Ye, J. Chen, M. Xu, X. Wei, H. Lu, Multi-scale simulation of nanoindentation on cast Inconel 718 and NbC precipitate for mechanical properties prediction, Mater. Sci. Eng. A. 662 (2016) 385–394. doi:10.1016/j.msea.2016.03.081.

[132] E. Salvati, T. Sui, A.M. Korsunsky, Uncertainty quantification of residual stress evaluation by the FIB–DIC ring-core method due to elastic anisotropy effects, Int. J. Solids Struct. 87 (2016) 61–69. doi:10.1016/j.ijsolstr.2016.02.031.

[133] G. Martin, N. Ochoa, K. Sai, E. Herve-Luanco, G. Cailletaud, A multiscale model for the elastoviscoplastic behavior of Directionally Solidified alloys: Application to FE structural computations, Int. J. Solids Struct. 51 (2014) 1175–1187. doi:10.1016/j.ijsolstr.2013.12.013.

[134] P. Haldipur, F.J. Margetan, R.B. Thompson, Estimation of Single-Crystal Elastic Constants from Ultrasonic Measurements on Polycrystalline Specimens, 1061 (2006).

[135] V.N. Parthasarathy, C.M. Graichen, A.F. Hathaway, A comparison of tetrahedron quality measures, Finite Elem. Anal. Des. 15 (1994) 255–261. doi:10.1016/0168-874X(94)90033-7.

[136] Z. Zhang, M.A. Cuddihy, F.P.E. Dunne, On rate-dependent polycrystal deformation : the temperature sensitivity of cold dwell fatigue, in: Proc. R. Soc. A Math. Phys. Eng. Sci., 2015.

[137] A. Manonukul, F.P.E. Dunne, High- and low-cycle fatigue crack initiation using polycrystal plasticity, Proc. R. Soc. A Math. Phys. Eng. Sci. 460 (2004) 1881–1903. doi:10.1098/rspa.2003.1258.

[138] C.A. Sweeney, W. Vorster, S.B. Leen, E. Sakurada, P.E. McHugh, F.P.E. Dunne, The role of elastic anisotropy, length scale and crystallographic slip in fatigue crack nucleation, J. Mech. Phys. Solids. 61 (2013) 1224–1240. doi:10.1016/j.jmps.2013.01.001.

[139] S.D. Antolovich, R.W. Armstrong, Plastic strain localization in metals: Origins and consequences, Prog. Mater. Sci. 59 (2014) 1–160. doi:10.1016/j.pmatsci.2013.06.001.

[140] A. Acharya, J.L. Bassani, Lattice incompatibility and a gradient theory of crystal plasticity, J. Mech. Phys. Solids. 48 (2000) 1565–1595. doi:10.1016/S0022-5096(99)00075-7.

[141] D. Naragani, M.D. Sangid, P.A. Shade, J.C. Schuren, H. Sharma, J.S. Park, P. Kenesei, J. V. Bernier, T.J. Turner, I. Parr, Investigation of fatigue crack initiation from a non-metallic inclusion via high energy x-ray diffraction microscopy, Acta Mater. 137 (2017) 71–84. doi:10.1016/j.actamat.2017.07.027.

[142] K. Kirane, S. Ghosh, A cold dwell fatigue crack nucleation criterion for polycrystalline Ti-6242 using grain-level crystal plasticity FE Model, Int. J. Fatigue. 30 (2008) 2127–2139. doi:10.1016/j.ijfatigue.2008.05.026.

[143] M.J. Caton, S.K. Jha, A.H. Rosenberger, J.M. Larsen, Divergence of Mechanisms and the Effect on the Fatigue Life Variability of Rene' 88 DT, Superalloys. (2004) 305–312.

[144] L. Huynh, J. Rotella, M.D. Sangid, Fatigue behavior of IN718 microtrusses produced via additive manufacturing, Mater. Des. 105 (2016) 278–289. doi:10.1016/j.matdes.2016.05.032.

[145] C.A. Kantzos, R.W. Cunningham, V. Tari, A.D. Rollett, Characterization of metal additive manufacturing surfaces using synchrotron X-ray CT and micromechanical modeling, Comput. Mech. (2017). doi:10.1007/s00466-017-1531-z.

[146] V. Prithivirajan, M.D. Sangid, Examining metrics for fatigue life predictions of additively manufactured IN718 via crystal plasticity modeling including the role of simulation volume and microstructural constraints, Mater. Sci. Eng. A. (2020).

[147] W.Z. Zhuang, G.R. Halford, Investigation of residual stress relaxation under cyclic load, Int. J. Fatigue. 23 (2001) 31–37. doi:10.1016/s0142-1123(01)00132-3.

[148] R. Bandyopadhyay, V. Prithivirajan, A.D. Peralta, M.D. Sangid, Microstructure sensitive critical plastic strain energy density criterion for fatigue life prediction across various loading regimes, Proc. R. Soc. A Math. Phys. Eng. Sci. (2020) 20190766. doi:http://dx.doi.org/10.1098/rspa.2019.0766.

[149] R.P. Skelton, Energy criterion for high temperature low cycle fatigue failure, Mater. Sci. Technol. 7 (2014) 427–440. doi:10.1179/mst.1991.7.5.427.

[150] A.M. Korsunsky, D. Dini, F.P.E. Dunne, M.J. Walsh, Comparative assessment of dissipated energy and other fatigue criteria, Int. J. Fatigue. 29 (2007) 1990–1995. doi:10.1016/j.ijfatigue.2007.01.007.

[151] K. Dang-Van, Macro-Micro Approach in High-Cycle Multiaxial Fatigue, Adv. Multiaxial Fatigue. (1993) 120–130. doi:10.1520/stp24799s.

[152] K. Chatterjee, A. Venkataraman, T. Garbaciak, J. Rotella, M.D. Sangid, A.J. Beaudoin, P. Kenesei, J.S. Park, A.L. Pilchak, Study of grain-level deformation and residual stresses in Ti-7Al under combined bending and tension using high energy diffraction microscopy (HEDM), Int. J. Solids Struct. 94–95 (2016) 35–49. doi:10.1016/j.ijsolstr.2016.05.010.

[153] Findley, W. N., A Theory for the Effect of Mean Stress on Fatigue of Metals Under Combined Torsion and Axial Load or Bending, J. Eng. Ind. (1959) 301–306.

[154] H. Mughrabi, R. Wang, K. Differt, U. Essmann, Fatigue Crack Initiation by Cyclic Slip Irreversibilities in High-Cycle Fatigue, Astm Stp 811. (1983) 5–45.

[155] C. Déprés, C.F. Robertson, M.C. Fivel, Crack initiation in fatigue: Experiments and three-dimensional dislocation simulations, Mater. Sci. Eng. A. 387–389 (2004) 288–291. doi:10.1016/j.msea.2003.12.084.

[156] J.P. Hirth, The Influence of Grain Boundaries, Metall. Trans. 3 (1972) 3047–3067. doi:10.1007/bf02661312.

[157] P. Neumann, A. Tönnessen, Crack Initiation at Grain Boundaries in F.C.C. Materials, in: Strength Met. Alloy. (ICSMA 8), Pergamon Press plc, 1989: pp. 743–748. doi:10.1016/b978-0-08-034804-9.50116-9.

[158] C.A. Brice, Proceedings of the 1st World Congress on Integrated Computational Materials Engineering, in: ICME, 2011: pp. 241–245.

[159] V. Prithivirajan, P. Ravi, D. Naragani, M.D. Sangid, Direct comparisons of microstructure-sensitive fatigue crack initiation via crystal plasticity simulations and in situ high energy X-ray experiments, Mater. Des. (2020).

[160] A. Cruzado, S. Lucarini, J. Llorca, J. Segurado, Crystal plasticity simulation of the e ff ect of grain size on the fatigue behavior of polycrystalline Inconel 718, Int. J. Fatigue. 113 (2018) 236–245. doi:10.1016/j.ijfatigue.2018.04.018.

[161] T. Zhang, J. Jiang, B. Britton, B. Shollock, F. Dunne, Crack nucleation using combined crystal plasticity modelling, high-resolution digital image correlation and high-resolution electron backscatter diffraction in a superalloy containing non-metallic inclusions under fatigue, Proc. R. Soc. A Math. Phys. Eng. Sci. 472 (2016). doi:10.1098/rspa.2015.0792.

[162] M. Obstalecki, S.L. Wong, P.R. Dawson, M.P. Miller, Quantitative analysis of crystal scale deformation heterogeneity during cyclic plasticity using high-energy X-ray diffraction and finite-element simulation, Acta Mater. 75 (2014) 259–272. doi:10.1016/j.actamat.2014.04.059.

[163] J. Oddershede, J.P. Wright, A. Beaudoin, G. Winther, Deformation-induced orientation spread in individual bulk grains of an interstitial-free steel, Acta Mater. 85 (2015) 301–313. doi:10.1016/j.actamat.2014.11.038.

[164] D.P. Naragani, P.A. Shade, P. Kenesei, H. Sharma, M.D. Sangid, X-ray characterization of the micromechanical response ahead of a propagating small fatigue crack in a Ni-based superalloy, Acta Mater. 179 (2019) 342–359. doi:10.1016/j.actamat.2019.08.005.

[165] I. Serrano-Munoz, J.Y. Buffiere, R. Mokso, C. Verdu, Y. Nadot, Location, location &size: Defects close to surfaces dominate fatigue crack initiation, Sci. Rep. 7 (2017) 1–9. doi:10.1038/srep45239.

[166] J.W. Hutchinson, Plasticity at the micron scale, Int. J. Solids Struct. 37 (2000) 225–238. doi:10.1016/S0020-7683(99)00090-6.

PUBLICATIONS

1. **V. Prithivirajan**, MD Sangid. The role of defects and critical pore size analysis in the fatigue response of additively manufactured IN718 via crystal plasticity. Materials & Design (2018).

2. **V Prithivirajan***[7], R Bandyopadhyay*, MD Sangid. Uncertainty quantification in the mechanical response of crystal plasticity simulations. The Journal of the Minerals, Metals & Materials Society (2019).

3. **V Prithivirajan**, MD Sangid. Examining metrics for fatigue life predictions of additively manufactured IN718 via crystal plasticity modeling including the role of simulation volume and microstructural constraints. Material Science and Engineering: A (2020).

4. R Bandyopadhyay, **V Prithivirajan**, A Peralta-Duran, MD Sangid. Microstructure sensitive critical plastic strain energy density criterion for fatigue life prediction across various loading regimes. Proceedings of the Royal Society A (2020).

5. MD Sangid, P Ravi, **V Prithivirajan**, NA Miller, JS Park, P Kenesei. An ICME Approach to Determining the Critical Pore Size of IN718 Produced by Selective Laser Melting. The Journal of the Minerals, Metals & Materials Society (2020).

6. **V Prithivirajan**, P.Ravi, D Naragani, MD Sangid. Direct comparison of microstructure sensitive fatigue crack initiation via crystal plasticity simulations and in situ high-energy X-ray experiments. Materials & Design (2020).

[7] * denotes equal contributions